INTERPRETATION OF NEAR-SOURCE GROUND MOTION AND IMPLICATIONS

Thesis by

Hsui-Lin Liu

In Partial Fulfillment of the Requirements

for the Degree of

Doctor of Philosophy

California Institute of Technology

Pasadena, California U.S.A.

1983

(submitted May 20, 1983)

To my parents

Acknowledgements

I thank deeply those of you who have helped make this work possible. My thesis advisor, Don Helmberger provided guidance and advice on my work through these years. Hiroo Kanamori guided my earlier research work and patiently reviewed the preliminary version of this thesis. A special thanks to Tom Heaton, who encouraged me to step into this specific research field and assisted my work in many aspects. I want to thank Dave Harkrider, Steve Hartzell, Ronan Le Bras, Gladys Engen, Robert Clayton and John Louie for their assistance in many numerical calculations and computer programs. I especially acknowledge Jeff Given, Tom Heaton and Ronan Le Bras for reading parts of the manuscript. And, finally, I appreciate the opportunity of being educated at Caltech and the Seismo Lab.

This work was partly supported by Air Force Systems Command, Hanscom Air Force Base, under Contract No. F19628-83-K-0010, and National Science Foundation, Earth Harzard Migration Section, under Grant # CEE-8121719, and National Science Foundation, Earth Science Section, under Grant # PFR-7921769.

Abstract

This thesis presents some deterministic modeling and interpretation of various aspects of observed near-source ground motions.

In Chapter 1, finite source parameters determined from waveform modeling studies are presented for two California earthquakes; the 1979 Coyote Lake event and the 1966 Parkfield event. These events were recorded by strong motion arrays with similar station to fault rupture geometries. Thus it is possible to demonstrate that differences in the ground motions recorded within 30 km of the epicenter are indeed due to the differences in rupture fault length and dislocation distribution.

Details of the waveform modeling for the August 6, 1979 Coyote Lake earthquake are described in part 1-A. A finite fault striking N24°W and extending to a depth of 10 km is proposed to model the strong-ground motion data. The source model suggests that right-lateral faulting initiated at a depth of 8 km and ruptured towards the south with a velocity of 2.8 km/sec. This unilateral rupture can explain the large displacements recorded south and southwest of the epicenter. However, the waveform coherency observed across an array south and southwest of the epicenter suggests that the rupture length is less than 6 km. The maximum dislocation is about 120 cm in a small area near the hypocenter and the total moment is estimated to be 3.5×10^{24} dyne-cm. An abrupt stopping phase, which corresponds to a cessation of right-lateral motion, can explain the high peak acceleration recorded at array station 6. The stress drop in the

hypocentral area is about 140 bars; although the average stress drop over the entire rupture surface is 30 bars. This preferred finite source model can predict observed P_{nl} waveforms as well as the beginning features of teleseismic body waves.

In part 1-B, a similar waveform modeling technique is used to interpret the ground motions recorded during the June 28, 1966 Parkfield earthquake. The preferred model suggests that the earthquake involved two fault segments; one is the NE branch which extends 22 km southward from epicenter and has an average slip of 45 cm, another is the SW branch which ruptured less than 10 km and has an average slip of about 22 cm. The total moment indicated by this model is 1.25×10^{25} dyne-cm. The anomalous large amplitude ground displacement seen at station Cholame No. 2 is modeled as a local amplification effect rather than a source effect due to significant dislocation near this station.

Direct waveform comparisons between recordings of the Parkfield event and the Coyote Lake event also support the conclusion that the rupture length of the Coyote Lake earthquake is much shorter than that of the Parkfield event. The waveform modeling also emphasizes the importance of using array data to constrain source parameters. The solution derived from a single station's recording, which in many cases is the only available information, may often produce misleading results.

In Chapter 2, high-frequency ground motions (ground velocity and acceleration) recorded at less than 30 km epicentral distances are studied for two aftershocks of the 1979 Imperial Valley, California earthquake. In the past, little has been done to understand these high frequency waves through a deterministic modeling approach. The waveform modeling technique and the source

mechanisms of these two aftershocks are described in sections 2-A and 2-B.

An important feature of the ground motions recorded during the October 15, 1979 Imperial Valley earthquake sequence is the strong high frequency waves observed on the vertical components. This feature is also seen in recordings of the aftershock of October 16, 23:16, 1979, which is described in section 2-A. This polarization feature is easily explained by the basin velocity structure which bends rays towards the vertical at the free surface. Short S-P times are observed at the three closest stations (epicentral distances of 3 km to 5 km) suggesting that this aftershock occurred at a very shallow depth of about 2 km. A fault plane orientation (strike=N20° E, dip=30° SE, and rake=-80°) obtained from a first P-motion study, generates synthetic waveforms of the strong ground velocities which are similar to those observed at three closest stations. The source time duration is determined to be 1.0 second and the moment is 1.6×10^{23} dyne-cm. Synthetics for a number of line source models are compared with the observations. These comparisons lead to two basic mechanisms that are necessary to explain the frequency content of the observed P- and S- waves. One is that the source process is characterized by irregular rupture. It is postulated that the heterogeneous stiffness in the layered medium is the basic cause of the irregular rupture. Heterogeneous rupture generates both high-frequency P- and S-waves. In order to explain the contrast in observed frequency content it is also necessary that there is a mechanism for attenuating S-waves much stronger than P-waves.

The aftershock that occurred about 3 minutes after the mainshock, at 23:19 October 15, 1979 is presented in section 2-B. This aftershock was located on the Imperial fault near Highway 8 and close to the zone of high frequency energy

release of the main event. The impulsive seismograms for 16 array stations, ranging from 8 km to 26 km in epicentral distance, are well suited for source parameter inversion studies to obtain an optimal solution for ground velocity and acceleration. The earthquake source is approximated by a model consisting of several point dislocation sources separated in space and time and having different dislocation orientations and moments. These source parameters were deduced by trial and error modeling as well as by applying inversion procedures. The waveforms and amplitudes of horizontal ground velocities are well modeled by two predominantly strike-slip point sources; the first source (strike= N41°W, dip=42°NE and rake=174°) has a moment of 0.7×10^{24} dyne-cm, the second source (strike=N36° W, dip=82°SW and rake=181°) lies about 1 km to the north of the first and has a seismic moment of about twice that of the first source. It is suggested that the higher-frequency ground motions , such as accelerations, can be derived from very irregular source processes, whereas the longer-period ground motions , such as ground displacements, can be well modeled by simpler planar source.

A Futterman attenuation operator with a t_β^* of about 0.08 to 0.1 and a t_α^* of about 0.001 in the sedimentary region produces longer period S waves and the proper amplitude ratio between P and S waves.

In Chapter 3, the ground motion data from the 1971 San Fernando earthquake recorded at epicentral distances of less than 100 km are presented. Three long profiles (> 50 km) and three short profiles (< 2 km) of ground velocity and acceleration, displayed as a function of epicentral distance are analyzed.

Although there is considerable variation in waveforms and peak amplitudes observed along the long profiles, there are also many examples of coherent phases seen at adjacent stations. Ground velocity profiles show striking differences in amplitude and duration between stations located on hard rock sites and stations located within the sedimentary basins. The San Fernando basin, in which the source is located, seems to respond quite differently from the Los Angeles basin which is about 30 km from the earthquake source area. Ground acceleration profiles show that there is little change in the duration of high-frequency shaking along the long profiles.

The three short profiles, which are all located within the Los Angeles basin, demonstrate that ground velocity waveforms are nearly identical along these profiles. Although greater variation of waveforms and amplitudes are seen for ground acceleration along these short profiles, strong phase coherence is still observed.

The 2D acoustical finite difference method is used to compute the effects on SH-waves of irregular velocity structures believed to exist along Profile I and Profile II. Profile I extends 65 km southward from the epicenter across the San Fernando and Los Angeles basins to a station on the Palos Verdes Peninsula. Profile II extends 95 km S 40° E along the front of the San Gabriel mountains and across the San Gabriel and Los Angeles basins. These numerical models consist of low-velocity sedimentary basins (β=2.1 km/sec) of irregular shape which are imbedded in high-velocity basement rock (β=3.5 km/sec). Heaton's (1982) finite source model derived from modeling the five nearest stations for the San Fernando event, is also incorporated in the interpretation. The resulting simulation suggests that the smaller S! phases in both Profile I and Profile II are direct

S waves from the deep source region (13 km). The shallow source region (at 1 km) dominates high amplitude later arrived phases observed along Profile I and are due to the complicated basin path along this profile. The shallower source region, however, contributes little to the ground motions along Profile II due to the lack of thick sediments near the source region along this azimuth.

Table of Contents

Introduction

In this thesis, earthquake ground motions recorded at small epicentral distances (< 100 km) are studied in order to better understand the earthquake source and the effects of wave propagation in the near-source region. Ideally, we expect the ground motions recorded within a couple of wavelengths from the source on a perfect bedrock site to represent mainly the source motion. However, such conditions are rarely encountered and the ground motions are altered during propagation through complex earth structure. Furthermore, the source complexity can easily be confused with complexity due to the complex response of earth structure. Thus the fundamental problem we face in this type of study is how to sort out the various effects which are generated from different origins. These difficulties can roughly be divided into three catagories, source complexity, path effect and wave interference, although in most of the problems we have studied it is impossible to avoid the ambiguity.

First, the source complexity; for a realistic rupture process, it is reasonable to accept a certain amount of roughness on the fault zone, which will allow two kinds of rupturing to accompany the earthquake process, namely, the coherent and incoherent sources. The coherent part of the source represents the over-all motion of the faulting, and we expect that the longer period phases, such as those seen in ground displacement records, characterize this coherent rupture. Teleseismic data are often used to study this type of source motion. On the other hand, the excitation of high frequency waves such as those

observed in ground acceleration records is sensitive to small rupture asperities, which are responsible for the incoherent part of the source.

The effect of source finiteness is another important consideration in the interpretation of near-source seismograms. For small faults, fault finiteness effects are not easily identified in regional and teleseismic data. However, it can significantly affect waveforms and amplitudes in the near-source region. A proper distribution of the near-source recording sites is very important for obtaining a reliable determination of fault size and dislocation distribution.

One approach to resolve source complexities is to construct a finite fault based on certain model parameters and then compare the resulting synthetics with the observed data. Examples include: 1966 Parkfield earthquake (Trifunac and Udwadia, 1974; Bouchon and Aki, 1979; Archuleta and Day, 1980); 1971 San Fernando earthquake (Trifunac, 1974; Boore and Zoback, 1974; Heaton and Helmberger, 1979); 1979 Imperial Valley earthquake (Hartzell and Helmberger, 1982). In order to reduce complications produced by earth structure it is desirable that the data are recorded at distances of less than about 5 times the source depths. Due to the rapid decay of amplitudes with distance in the near-source region, ground motion data recorded at distances small when compared to fault dimension can provide information only for the near-by segment of the faulting. Thus, for studying long ruptures, we need to use array data to resolve the dislocation distribution accompanying the whole faulting process.

Second, the path effects; in the near-source region, earth structure is of fundamental importance for waveform development, such as multiple arrivals, amplification, scattering and attenuation. Thus, in near-source waveform modeling studies, a detailed knowledge of earth structure is very important. It

is difficult to compare source characteristics of different events recorded at different station-source geometries unless the impulse response of the medium is well understood. The ground motions recorded from aftershocks can provide important constraints in the development of realistic impulse responses used for modeling high-frequency waves from mainshocks.

Third, the wave interference; due to the small epicentral distances inherent in near-source problems, different types of waves produced from various origins can arrive at stations almost simultaneously, thereby making it difficult to reliably identify individual arrivals. In many instances, surface waves can dominate observed arrivals at epicentral distances of as little as 30 km.

It is clear that the array data of strong motions can constrain the many free parameters in near-source distances as opposed to far-field data. This feature is emphasized in this thesis. A brief introduction of each chapter will be described as follows.

The first chapter describes the finite source modeling technique by analyzing the near-source ground motions from two California earthquakes; the 1979 Coyote Lake earthquake (in section 1-A) and the 1966 Parkfield earthquake (in section 1-B). Although the seismic moment of the Coyote Lake event (3.5×10^{24} dyne-cm) is about one-third of the moment of the Parkfield earthquake (1.2×10^{25} dyne-cm), the Coyote Lake earthquake has actually been assigned a larger local magnitude (M_L=5.9) than has the Parkfield earthquake (M_L=5.6). It is suggested that the 1979 Coyote Lake earthquake had a rupture length of about 6 km, whereas the 1966 Parkfield earthquake ruptured a fault length of more than 30 km. These earthquakes had similar strike-slip mechanism and were recorded by strong motion arrays with similar source-station geometries.

This allows us to resolve the differences in the source characteristics of these two events. Also a comparison of the teleseismic body waves recorded for these events is interpreted in terms of differences in the source characteristics.

The discrete wavenumber finite element method (Olson, 1982) is used to calculate point dislocation source responses of horizontally layered earth structure. Finite source is modeled by the integrated sum of the point sources over the proposed fault plane. Although the earth structures used for these two events are slightly different, the point source responses are similar enough for us to compare the recorded ground motions in a direct manner.

In the second chapter, we study the high frequency waves (ground velocity and acceleration) which were recorded by array stations for two aftershocks of the 1979 Imperial Valley earthquake. In the past, most of the approaches used to understand high frequency ground motions utilized either statistical or empirical analysis. In this work we interpret the waveforms and frequency contents deterministically based on assumed physical processes. In the first part of this chapter, 2-A, one of the 1979 Imperial Valley aftershocks (M_L = 5.0) is studied, which occurred about one day after the main event. Very distinguishable high-frequency ground motions were recorded on vertical components for this event. This type of high-frequency (> 10 Hz) enriched seismogram seems to be a common feature for many events seen in the Imperial Valley. We propose that the source velocity gradient in the Imperial Valley is responsible for this phenomenon. Very low velocity and high shear attenuation sediments near the free surface cause P- and S-waves to be almost entirely vertically and horizontally polarized, respectively. Because of the steep incidence angle, only S-waves are significantly attenuated in the shallowest sediments, thereby causing the

observed discrepancy in the observed frequency content of P- and S-waves. In the second part, 2-B, another aftershock (M_L of 5.0) is studied, which occurred about 3 minutes after the main event. Abundant high quality data are available for this event, allowing us to investigate the predictability and as well the randomness of the high frequency ground motions.

For both aftershock studies, the Green's functions are computed using the Generalized Ray method along with a high frequency approximation (Helmberger and Harkrider, 1978). The multi-layered structures (22 layers for the top 5 km) used for the Green's function calculation are slightly different for these two events. A line source model is used to simulate source complexity at high frequencies (1 to 10 Hz). An amplitude inversion method is also used to determine the optimal model parameters for the line source.

A similar approach is also used to explain some strong phases seen in the acceleration recordings of the 1979 Imperial Valley mainshock. However, the uniqueness of the interpretation is hard to verify.

In chapter 3, ground motion profiles of strong motion data recorded during the 1971 San Fernando earthquake are displayed. In many respects, the San Fernando earthquake is still the best recorded earthquake. There are both dense arrays and also stations at a wide range of distance (up to 100 km), allowing us to construct ground motion profiles along three azimuths. A remarkable correlation of the ground motions with bedrock geometry is seen. It is suggested that for epicentral distances of greater than 30 km, propagation path plays a very important role in wave development. A 2D acoustical finite difference method (Brown and Clayton, 1983) is used to simulate SH wave propagation along irregular structures. Incorporating the source model

determined by Heaton (1982), we attempt to identify arrivals derived from different parts of the finite fault. The phase delays and the amplitude fluctuations along the propagation path are also examined.

Chapter 1 Finite Source Modeling of the Ground Displacements

1-A The Near-Source Ground Motion of the August 6, 1979 Coyote Lake California Earthquake

Introduction

The strong ground motions recorded at the Gilroy array and San-Martin Coyote-Creek station from the August 6, 1979 Coyote Lake, California earthquake (M_L =5.9) provide a good opportunity to investigate the faulting process along the Calaveras fault zone. From a seismological point of view, the near-in data reflect the most detailed information available about the faulting process, especially the portion of the fault which radiates the high frequency energy. However, interpreting these details of the source process necessitates constructing source models with a large number of free parameters (e.g., rupture velocity, rupture direction, dislocation size and distribution). Data from an array of near-source instruments are essential to reliably constrain these unknowns.

A detailed analysis of the strong ground motion data will be presented in this paper. In particular, we will demonstrate how to interpret the data in terms of fault size, rupture speed, rupture direction and fault dislocation heterogeneity. We will then use our near-source model to interpret regional and

teleseismic seismograms.

Source Location and Mechanism

The epicenter of the Coyote Lake earthquake was located about 13 km northeast of Gilroy by the University of California, Berkeley (Uhrhammer, 1980). This location is about 3 km to the northeast of the location obtained by the U.S. Geological Survey as shown in Figure 1-A-1 (Lee et al., 1979). The Gilroy stations (GA-1, GA-2, GA-3, GA-4, and GA-6) and San Martin-Coyote Creek (SMCC) range from 2 km to 16 km from the epicenter (Brady et al., 1979).

The first P-motion distribution indicates a nearly pure strike-slip mechanism with strike (N24° W) parallel to the Calaveras fault (Lee et al., 1979). The teleseismic and regional first P motions suggest a plane dipping 80° to the northeast (see Figure 1-A-2). No clear surface faulting was found near the epicentral region. Right-lateral surface breakage of about 0.5 cm is reported near the junction of highway 152 and the Calaveras fault and is marked as the shaded area in Figure 1-A-1 (Herd et al., 1979).

Strong Ground Motion Data

The recorded strong ground accelerations were corrected and integrated to velocities and displacements (Brady et al., 1979). We rotate the horizontal velocities into the radial and transverse components defined relative to source BK (shown in Figure 1-A-3). The arrows in Figure 1-A-3 indicate the S arrivals and all traces start at the trigger time. The major signal is less than 2 seconds in duration at all stations. In general the waveforms are very coherent across the Gilroy array although broader waveforms are observed on the tangential

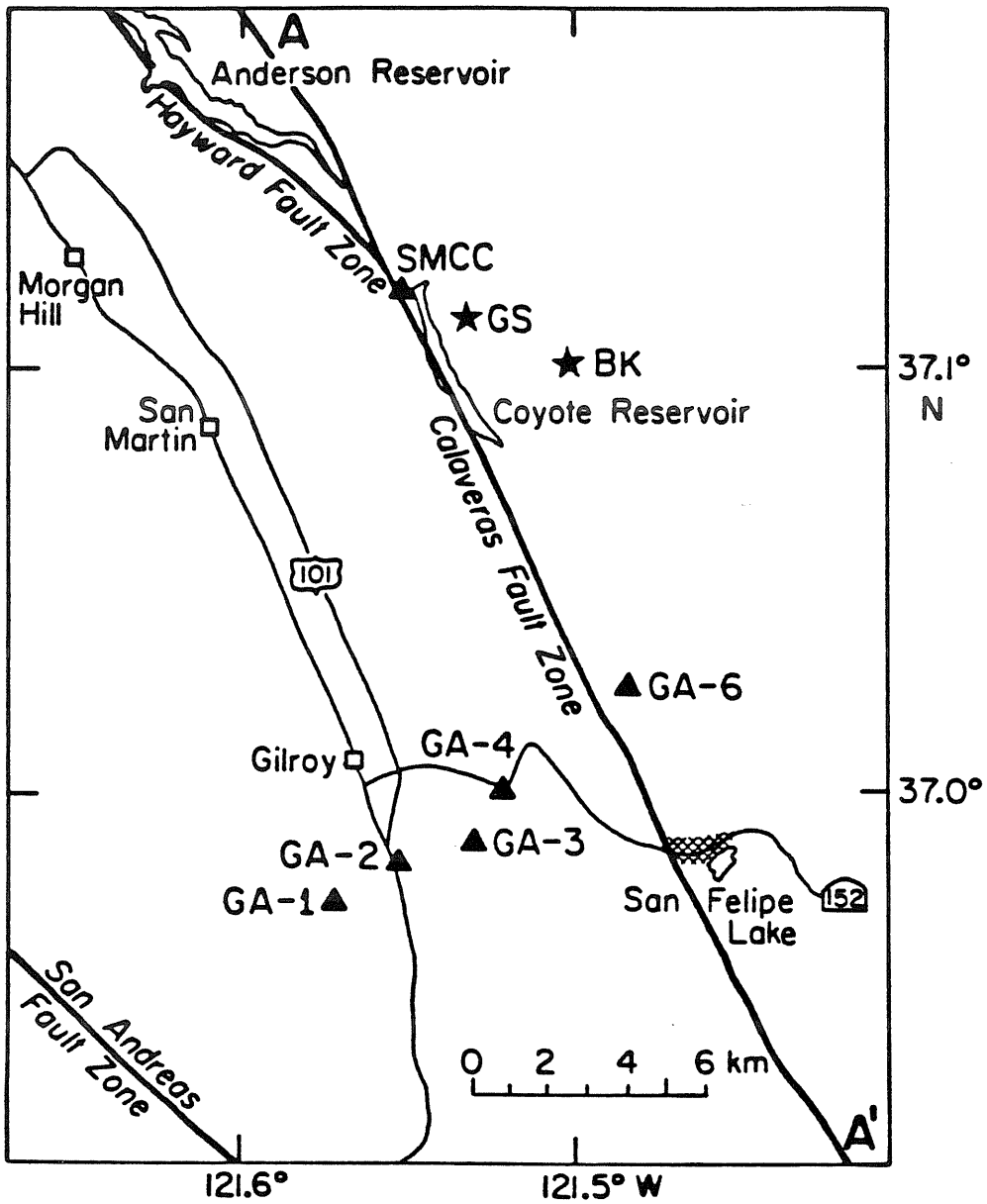

Figure 1-A-1 Epicenter of the August 6, 1979 Coyote Lake, California Earthquake. GS is the epicenter located by U.S.G.S. and BK is the U.C. Berkeley location. The solid triangles are the strong-ground motion sites which include San-Martin Coyote-Creek (SMCC) and the Gilroy array (GA-1, GA-2, GA-3, GA-4, and GA-6). The shaded area near the junction of highway 152 and the Calaveras fault zone is the location where a 0.5 cm right-lateral surface breakage is reported.

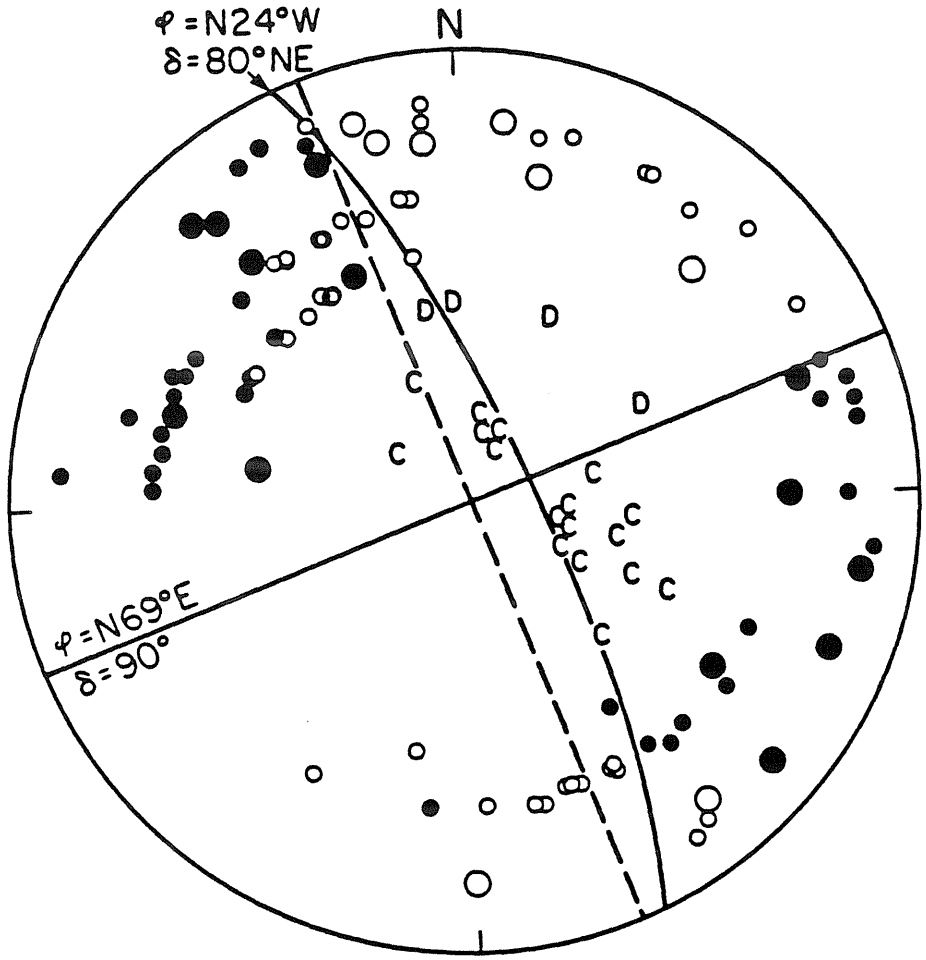

Figure 1-A-2 The lower hemisphere equal-area projection of the first P-motions. The solid dots and circles are the local compressional and dilatational projections taken from Lee et al (1979). C and Ds are, respectively, compressional and dilatational first P-motions from regional and teleseismic stations. The dashed line is the fault plane determined by Lee et al (1979) and the solid line is the one determined in this study, which has a 80 degrees dip to the northeast.

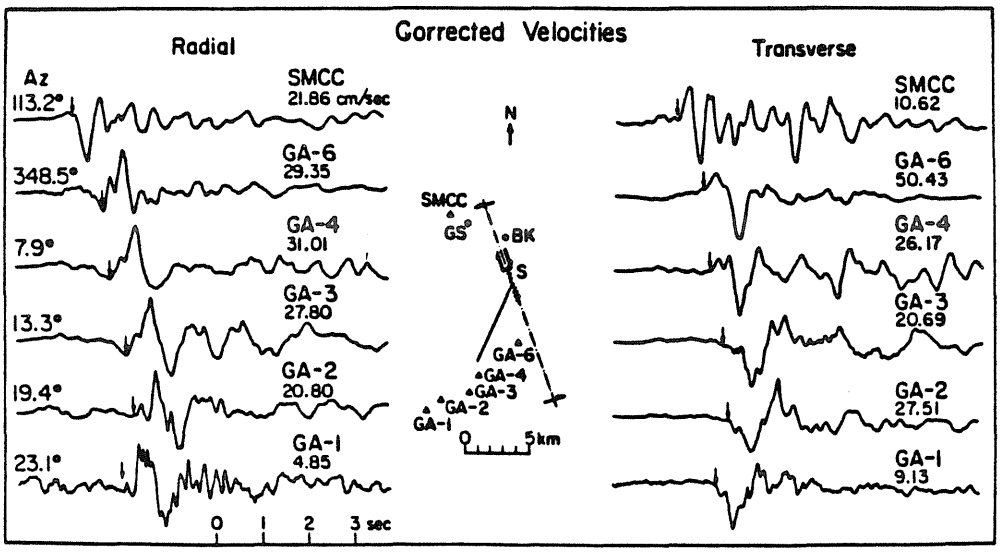

Figure 1-A-3 The horizontal velocities from San Martin-Coyote Creek and Gilroy Array. The data are rotated relative to the BK epicenter as transverse and radial components, as indicated by their back azimuths. The absolute amplitudes are indicated as those numbers with units of cm/sec. The arrows indicate the S-arrivals.

components southwest of the epicenter. Table 1-A-1 lists the station information and their peak amplitudes.

Although the station SMCC which lies northwest of the epicenter has the shortest epicentral distance, its amplitudes are smaller than most of the southern stations, particularly station GA-6. One possible explanation for the difference in amplitude is the rupture direction along the fault. Since most of the aftershock activity was located south of San-Felipe, lateral rupture along the fault toward the station GA-6 was postulated to explain the high amplitude seismograms (Archuleta, 1979). The directivity effect will be analyzed later together with other array displacements. In addition GA-6 lies close to an SH radiation maximum, and the N230°E component is naturally rotated in the tangential direction. It seems that the radiation pattern also contributes to the high amplitude observed there.

Figure 1-A-4 shows the corrected acceleration (the maximum observed horizontal acceleration for this event) and the corresponding velocity and displacement recorded at station GA-6 on component N230° E. The displacement, with a peak value of about 10 cm, is consistent with the right lateral strike-slip faulting. However, the high acceleration (arriving near 2.5 seconds) and the corresponding peak velocity indicate the decelerated motion at the end of the faulting process. An abrupt stopping of the rupture seems to be the most likely explanation for this high acceleration at station GA-6.

It can be seen in Figure 1-A-3 that the amplitudes vary slowly across the Gilroy array except for the most distant station GA-1. Station GA-1 has a very low amplitude signal compared to GA-2, which is only about 2 km away. The radiation pattern and rupture direction can not explain a factor of 3 amplitude

Table 1-A-1 Strong-ground Motion Stations and Data

Station	Coordi.	S-P time (sec)	Comp.	Acc. (cm/sec^2)	Vel. (cm/sec)	Dis. (cm)
SMCC	37.118N	1.3	250°	245	20.5	2.4
	121.550W		UP	101	7.2	0.7
			160°	138	11.5	1.1
GA-6	37.026N	1.5	320°	315	25.1	3.6
	121.484W		UP	147	16.5	3.1
			230°	409	43.8	9.3
GA-4	37.000N	2.2	360°	246	32.2	5.2
	121.521W		UP	409	15.4	2.5
			270°	228	25.2	3.0
GA-3	36.991N	2.6	140°	246	29.4	5.7
	121.536W		UP	136	7.0	1.2
			50°	252	16.9	3.7
GA-2	36.982N	2.7	140°	249	31.9	5.3
	121.556W		UP	162	6.6	1.0
			50°	186	10.2	2.2
GA-1	36.973N	2.5	320°	111	10.3	1.7
	121.572W		UP	58	2.6	.5
			230°	84	4.0	.7

* The data are taken from Brady and others (1979).

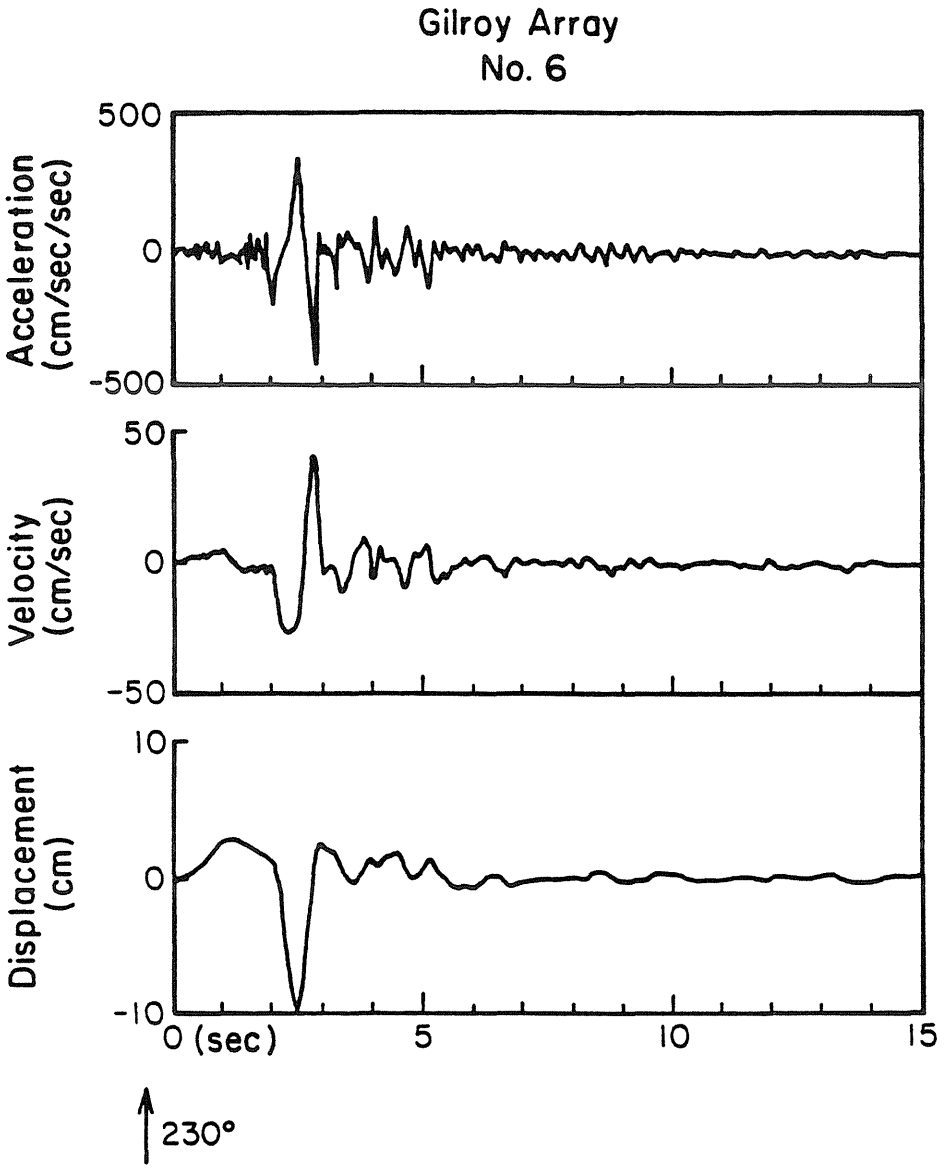

Figure 1-A-4 The corrected acceleration, integrated velocity and displacement at Gilroy station no. 6. The positive motion is along N230° E.

difference. Joyner and others (1981) interpreted this as an alluvium amplification effect on station GA-2. Nevertheless, the waveforms are quite similar at GA-2 and GA-1 for both horizontal components.

To model the strong ground motions we locate the fault consistent with the available data, i.e., fault-plane geometry and observed radiation pattern. The focal mechanism from the first P-motions suggests a fault plane with similar strike to the Calaveras fault (N24°E) and with 80° dip to the east. The initial motions of the transverse and radial components of the displacements are identified as the radiation from the hypocenter. The first arrivals seen on the transverse components reverse polarity between station GA-3 and GA-4, indicating that a nodal line corresponding to SH waves from the initiation of rupture lies between these two stations (as indicated by the solid line in Figure 1-A-3). The azimuth of the nodal line is fixed to agree with the orientation of the fault plane and the hypocenter of our source model is constrained to lie on that line. The first radial S-motions of stations GA-4 and GA-6 indicate that both stations lie to the west of a line defined by the fault strike. We therefore propose to model the near-source ground motions by a 10 km long fault striking N24°W and dipping 80° to the northeast. The surface projection of the finite fault is indicated as the dashed line along N24°W in Figure 1-A-3, which is about 2 km east of the surface trace of the Calaveras fault. We suggest that the rupture started at the intersection of the SH nodal line and fault strike direction indicated by the point S in Figure 1-A-3. We further suggest that most of the rupture occurred in a localized area just south of the hypocenter producing the short and coherent horizontal signals observed at different azimuths at the Gilroy array.

We also plot the vertical velocities in Figure 1-A-5. The amplitude is about one-third of the horizontal motion. The downward solid arrows in Figure 1-A-5 indicate our expected S arrivals determined from the horizontal components. However, in the vertical traces these coherent phases can be recognized only in stations SMCC and GA-6. It appears that some earlier arrivals in station GA-4 and GA-3 (about .8 sec earlier, indicated as upward dashed arrows) are more likely the S waves. GA-4 and GA-3 are near the node of SH waves or the maximum of P waves, and P to SV converted energy may explain the earlier arrival times. Angstman and others (1979) interpret these as an S-P converted phase due to the low velocity in the alluvium near the receiver.

Strong Ground Motion Modeling

A finite dislocation source along a 10×8 km^2 fault is used to simulate the horizontal ground displacements. The velocity structure (listed in Table 1-A-2) used to locate the aftershocks near the Gilroy array area by Lee et al. (1979) is adapted to calculate the theoretical seismograms. The full point source responses up to 2 Hz are calculated by the discrete wavenumber, finite element technique (Olson, 1978; Hartzell and Helmberger, 1981). Figure 1-A-6 shows the SH displacements from a strike-slip fault at various distances and depths. For the sources deeper than 4 km, which is very likely the case in this earthquake , the responses reflect mainly the source character.

Our finite source model is simply the sum of the responses due to point sources along the fault with proper time lags determined by the arrival of rupture front (Heaton, 1982). We use 1×1 km^2 as the basic grid size in computing the step responses. In order to have finer grids efficiently, we linearly

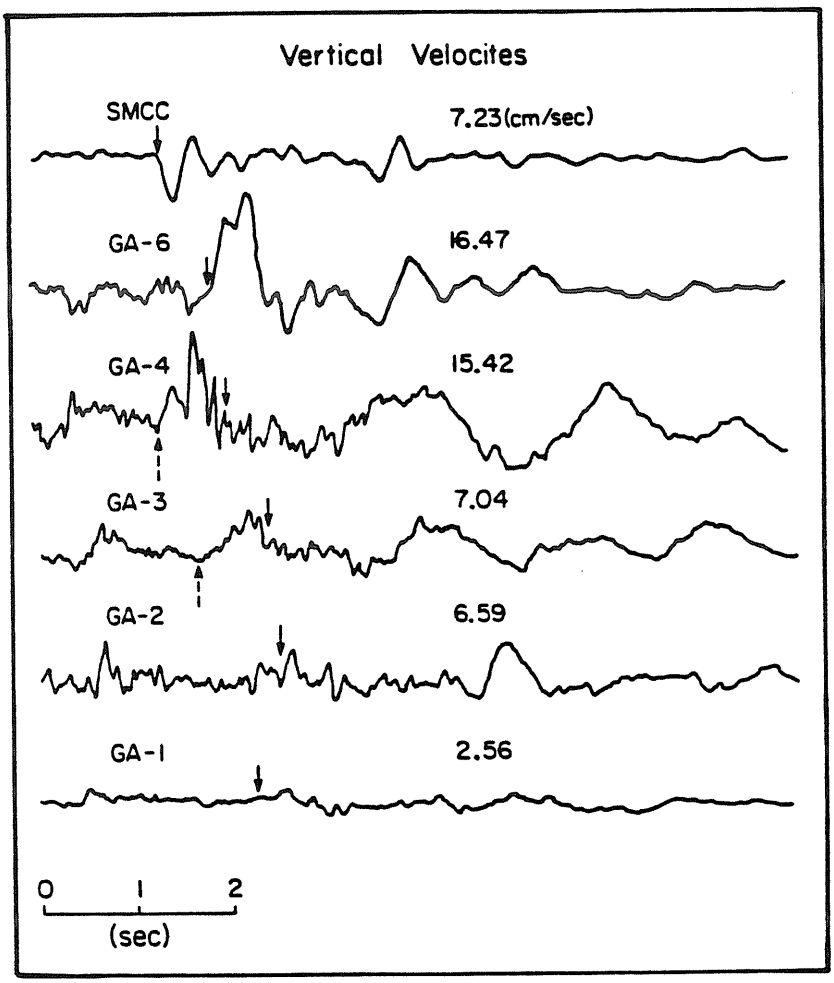

Figure 1-A-5 Vertical components of the integrated velocity from San Martin-Coyote Creek and Gilroy array stations. The solid arrows indicate the expected S arrivals determined from horizontal components. The dashed arrows marked in GA-4 and GA-3 indicate the possible converted phases which arrived earlier than the S waves.

Table 1-A-2 The Velocity Structure

Thickness (km)	P-vel (km/sec)	S-vel (km/sec)	Density (g/cm^3)
0.5	3.0	1.5	2.4
2.5	5.0	2.8	2.7
9.0	5.7	3.3	2.78
--	6.9	3.9	3.0

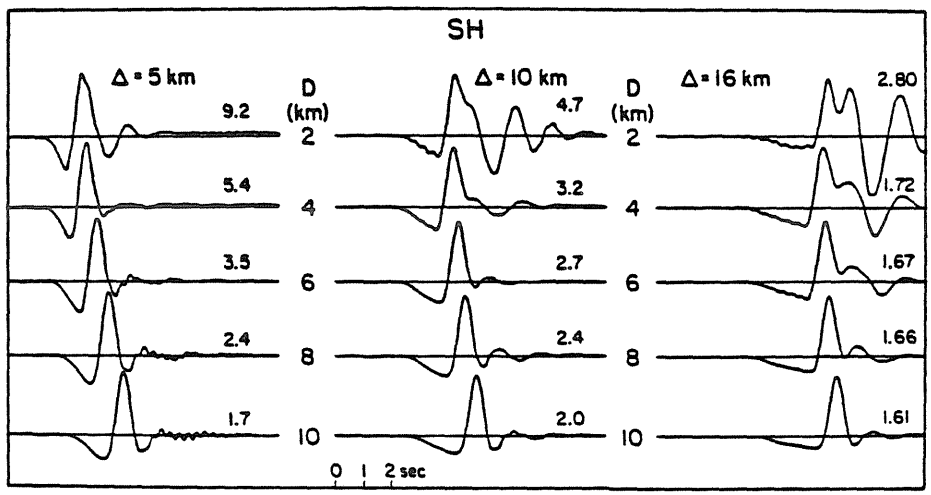

Figure 1-A-6 The synthetic SH displacements for a pure strike-slip source at various distances (5 km, 10 km, and 16 km) and depths (from 2 km to 10 km). The Green's functions are generated by discrete wavenumber finite-element technique and represent the full wave field for the structure listed on Table 1-A-2. A one-second triangular time function (0.5, 0.5) is convolved with the Green's function to obtain the displacement.

interpolate the Green's functions for a $.5 \times .5 km^2$ grid from the adjacent points. A .5 second symmetric triangular time function is assumed to represent the time derivative of the dislocation time history of each point on the finite fault. The dislocation along the fault, or the final slip, and the fault area can be varied easily by adjusting the moment of each grid point source. Once the faulting initiates, it propagates at a constant speed and forms a circular rupture front, terminating when it reaches the edge of the finite fault boundary.

Our preferred dislocation model N1 derived by trial and error modelling is illustrated in Figure 1-A-7. We essentially constrain the fault size by the signal durations, especially from the more distant stations, such as GA-1, GA-2, GA-3 and GA-4. The rupture velocity is then adjusted by the relative amplitudes among these stations, particularly the contrast between the northern station SMCC and the southern station GA-6. The hypocenter is located at a depth of 8 km. The rupture started at that point and propagated with a velocity of about 2.8 km/sec. A 0.3 km/sec variation of the rupture velocity can still generate acceptable amplitudes without significant change of the fault size. This model suggests that the major faulting responsible for the near-source ground displacements accounted for 60% of the total moment and took place in a small area of about $2km \times 3$km just south of the hypocenter. The rupture propagated mostly toward station GA-6, which explains part of high amplitude waveforms recorded in GA-6.

Figure 1-A-8 illustrates the comparison of the observed horizontal ground displacements vs. the synthetics for this model. An Ormsby filter (high pass .05Hz-.25Hz) has been applied to both observed and synthetic displacements shown in Figure 1-A-8. In general, the waveforms and amplitudes agree quite

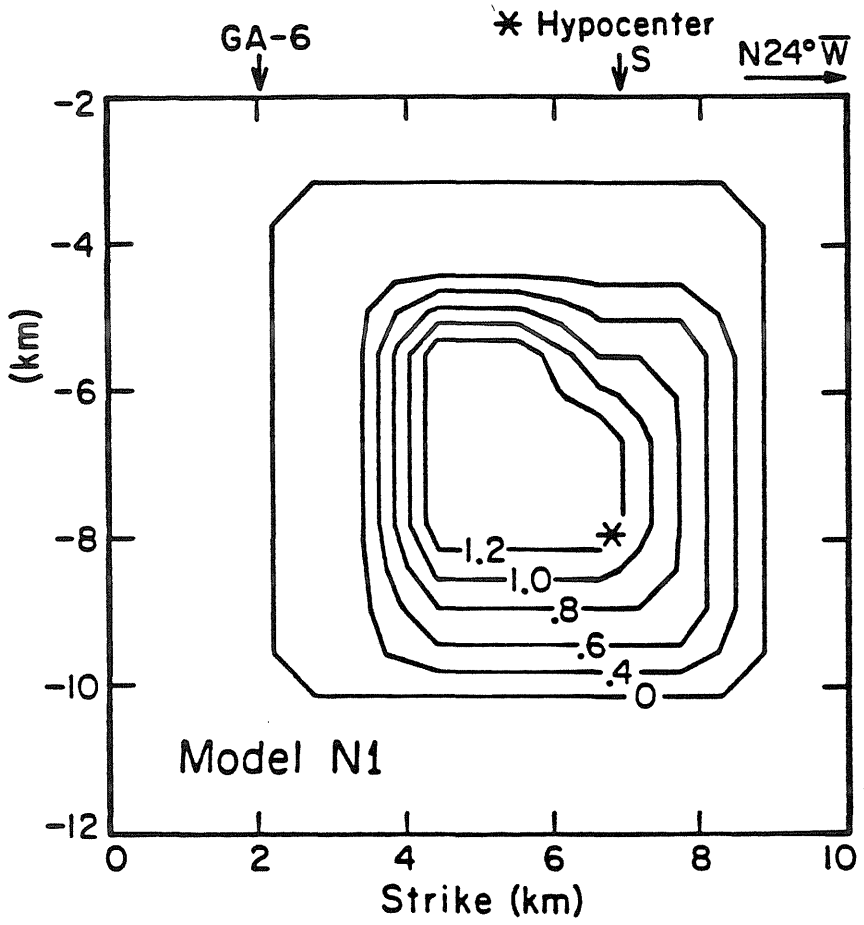

Figure 1-A-7 The dislocation distribution along the fault in our preferred model. The units are meters. S is the epicenter indicated in Figure 1-A-3.

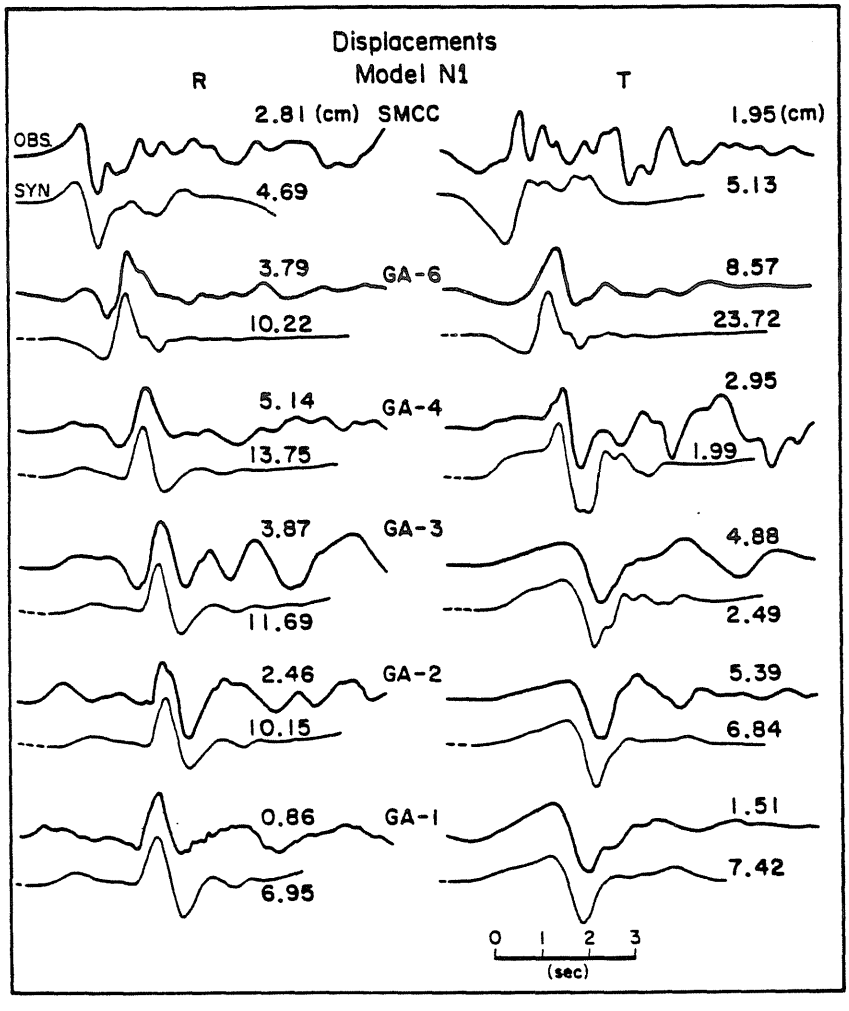

Figure 1-A-8 The observed radial and transverse displacements compared with synthetics for the dislocation model N1. The dashed trace in the beginning of the synthetic seismogram is the discrepancy in the travel time. The number associated with each station indicate the displacement in cm. The synthetic seismograms are calculated for a moment of 10^{25} dyne-cm.

well. The transverse components of GA-3 and GA-4 are close to a node and are sensitive to small variations. Our model can not predict the observed transverse amplitudes of these two stations. A detailed study of the ground motions recorded near nodal stations will be discussed in Chapter 2-B. If we exclude the transverse components of GA-3 and GA-4, the average seismic moment for the horizontal components is about 3.5×10^{24} dyne-cm. A maximum slip of about 1.2 m is obtained near the hypocenter. The total rupture length along the strike direction is about 6 km and the fault area is about 40 km^2. The stress drop near the hypocentral region ($2\times3km^2$) is 140 bars, but if we average over the entire source area it would be about 30 bars. From our non-uniform dislocation model, we can consistently predict almost zero slip on the free surface. Table 1-A-3 summarizes the source parameters for our preferred finite source model.

In order to demonstrate how the fault dislocation affects the array records, we show a uniform dislocation model, U1. This model has the same fault length as model N1, but the final dislocation of 17 cm is uniformly distributed. The hypocenter is located at the same place as in model N1. Figure 1-A-9 shows the synthetics for model U1. Due to larger rupture area, the waveforms are much broader for the stations further away from the fault, such as stations GA-4, GA-3, GA-2 and GA-1. The waveforms at station GA-6 are fit reasonably well, since they are not particularly sensitive to the size of the fault. Most of the observed signal durations from the array data suggest that the rupture duration was shorter than that implied by model U1. Thus the high amplitude records in GA-6 are not necessarily caused by a long fault. A slower rupture might accompany the source process at the end, but in terms of the beginning 7-seconds of motion, we prefer the concentrated dislocation source model N1 to explain what we have

Table 1-A-3 Source Parameters

Local magnitude	5.9
Seismic moment	3.5×10^{24} dyne-cm
Focal mechanism	strike=N24° W dip=80° slip=176°
Fault size*	40 km^2
Rupture speed	2.8 km/sec
Hypocenter depth	8 km
Maximum dislocation	120 cm
Average stress drop	30 bars

*The fault size here regards the area with slip greater than zero

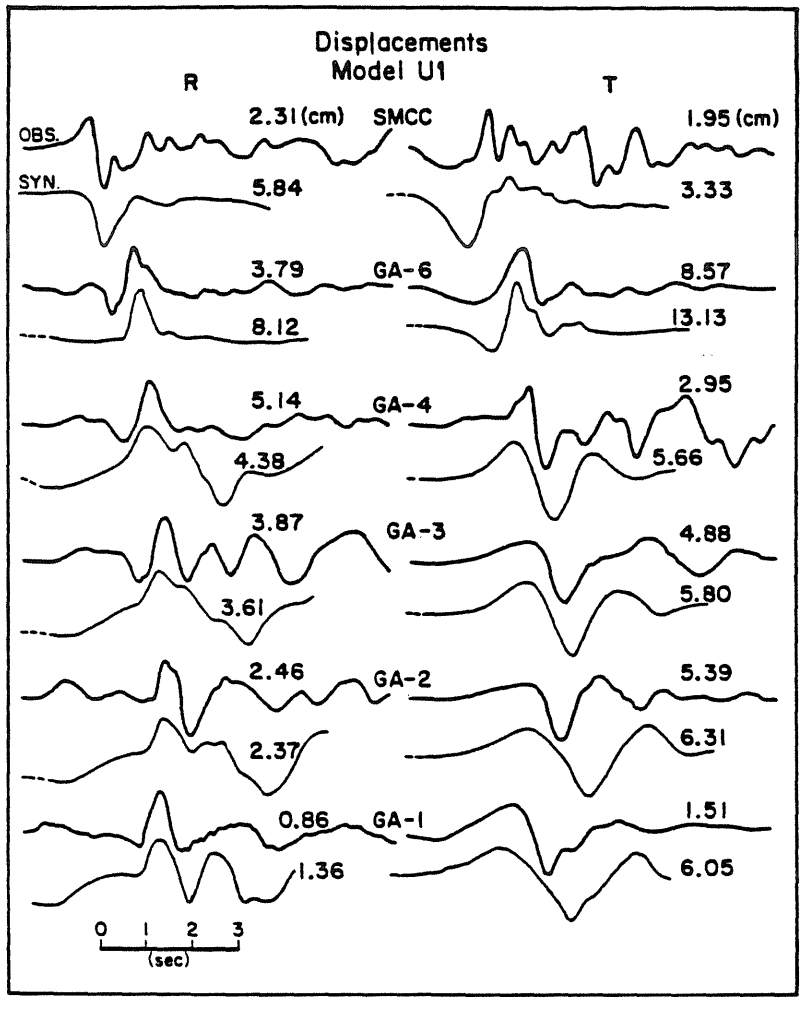

Figure 1-A-9 The observed horizontal displacements and synthetics from model U1. The displacements are indicated in cm. The synthetic seismograms are calculated for a moment of 10^{25} dyne-cm.

observed.

Bouchon (1982) derived a uniform dislocation fault model for the Coyote Lake earthquake from the waveform modeling in transverse components at stations GA-6, SMCC and the broadband seismogram recorded at Berkeley (about 107 km from the epicenter). Bouchon's source model has a fault length of 14 km and extends from the depth of 1 km to 10 km. The final slip of 15 cm to 20 cm was suggested. The rupture velocity was determined to be 2.6 km/sec. We argue that Bouchon's fault model is similar to U1 model shown in Figure 1-A-9 but with even larger fault area, which would produce much broader waveforms for stations not located on the fault. Bouchon used a high-frequency stopping phase identified at Berkeley broadband seismogram to determine the fault size. We also argue that at the distance of about 100 km this high-frequency phase could also be the Moho reflected wave. The Green's function at this distance is very sensitive to the detailed velocity structure. Unless we know the crustal model very well, it is difficult to identify the source phase in Berkeley records. Instead, we will demonstrate the small source character suggested in the far-field by modeling the teleseismic data in the following section.

Regional and Teleseismic Data

In order to test our finite source model, we synthesize the waveforms recorded at both regional distances (1° to 12°) and teleseismic distances (30° to 90°) from model N1.

The long-period body waves recorded at regional distances can be represented by the combinations of P_n and P_l phases, or P_{nl} waves, which have propagated through a single crustal layer over a half-space (Helmberger and

Engen, 1980; Wallace et al., 1981). Due to the long-period character of the P_{nl} waves, they can not be used to resolve the source time function. However, P_{nl} waves can provide good constraints on the fault orientation and the seismic moment. For simplicity, a trapezoidal time function with 3 seconds duration is assumed to represent the far-field source time history (see Figure 1-A-10). The observed and the synthetic P_{nl} waves for the Coyote Lake earthquake are shown in Figure 1-A-10. The station information is listed in Table 1-A-4. We found good agreement in waveshapes and amplitudes. The seismic moment used to calculate the amplitude is 3.5×10^{24} dyne-cm, which is the moment we obtained from the model N1. No attenuation is considered in this synthetic calculation. The comparable amplitudes of the observations vs. synthetics indicate that no significant attenuation accompanies the propagation of P_{nl} waves.

The teleseismic body waves (30° to 90°) are generally accepted as the more reliable data for describing the overall motion during the earthquake process. An important question we would like to answer is whether the finite source model can predict the teleseismic seismograms. For the Coyote Lake event, due to the nearly pure strike-slip mechanism and relatively small moment, few teleseismic P waves were observed. Here we simply generate the teleseismic long-period P (vertical component) and SH waves for our finite source model N1. The stations used are listed on Table 1-A-5. The structure we considered is a half-space (α = 6.0 km/sec, β = 3.5 km/sec, and ρ = 2.78 g/cm^3) and thus the seismograms are assumed to consist of P, pP and sP for vertical P waves and S, sS for SH waves (Langston and Helmberger, 1975). The far-field source time function is calculated from the finite source model N1 for each station (Heaton, 1982). Figure 1-A-11 illustrates the observed and synthetic vertical P and SH

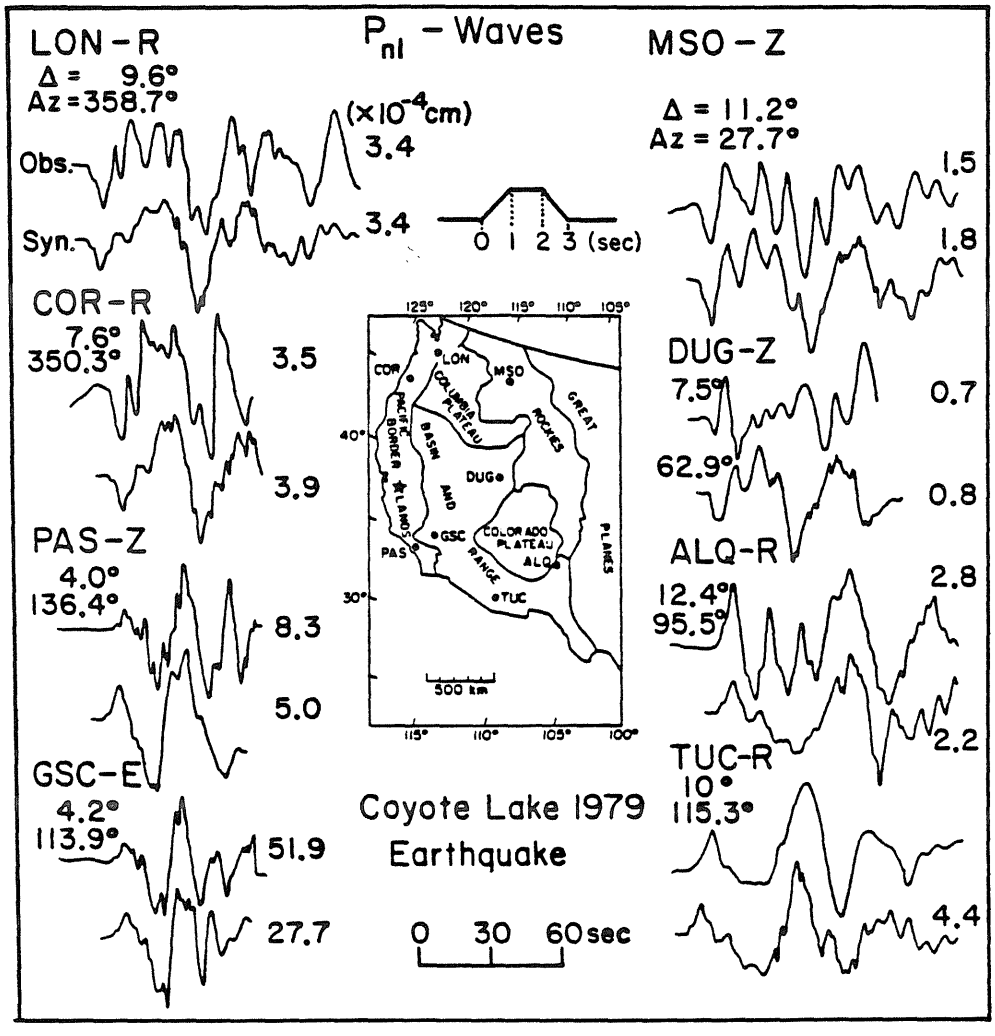

Figure 1-A-10 The observed P_{nl} waves vs. synthetics for model N1. The number associated with each station is the absolute ground displacement. The synthetics are calculated for a moment of 3.5×10^{24} dyne-cm. No amplification factor is available for amplitude correction at station TUC.

Table 1-A-4 Stations for P_{nl} waves

Station Name	Epicentral Distance	Azimuth	Component(*)
ALQ	12.4	95.5	R
COR	7.6	350.3	R
DUG	7.5	62.9	Z
GSC	4.2	113.9	E
LON	9.6	358.7	R
MSO	11.2	27.7	Z
PAS	4.0	136.4	Z
TUC	10.0	115.3	R

* Z: The vertical component.
E: The east-west component.
R: The radial component.

waveforms. This comparison shows that our finite source model can predict the beginning 10 seconds of motion well, but it can not predict the later arrivals. The seismic moment is about 3.6×10^{24} dyne-cm. The average far-field source time function for model N1 is about 2 seconds.

Nabelek (1982) has inverted these teleseismic data for source parameters and found that the waveforms can be matched better by three separate events. His preferred solution is described in Figure 1-A-12, which includes the main shock (the first event) and two aftershocks, 6 and 12 seconds later. Our finite source model is very close to Nabelek's first event in terms of source time duration and seismic moment. The fault orientation of Nabelek has about the same dip angle and slip as ours, but the strike is rotated 12° further to the west. In Nabelek's solution, the first event, or the mainshock, has a moment about 3 times larger than the other two events. The second and third events, which have very different fault geometry from the first earthquake, can not be recognized in the near source ground motion records. According to the far-field source parameters determined by Nabelek, the second event is probably too small to be seen in the near-field, but the third event is expected to produce about one-third of the near-source ground motions as the main event. The possible explanation for this discrepancy is either the third source is outside the strong-ground motion array and rupturing away from it or the source process is too smooth to produce significant near-source ground motions.

Few teleseismic stations recorded good-quality short period vertical seismograms. The stations in South America show rather high short-period amplitude when compared with stations in other azimuths. Figure 1-A-13 shows the seismograms from 4 of these stations, which yield azimuthal range of about

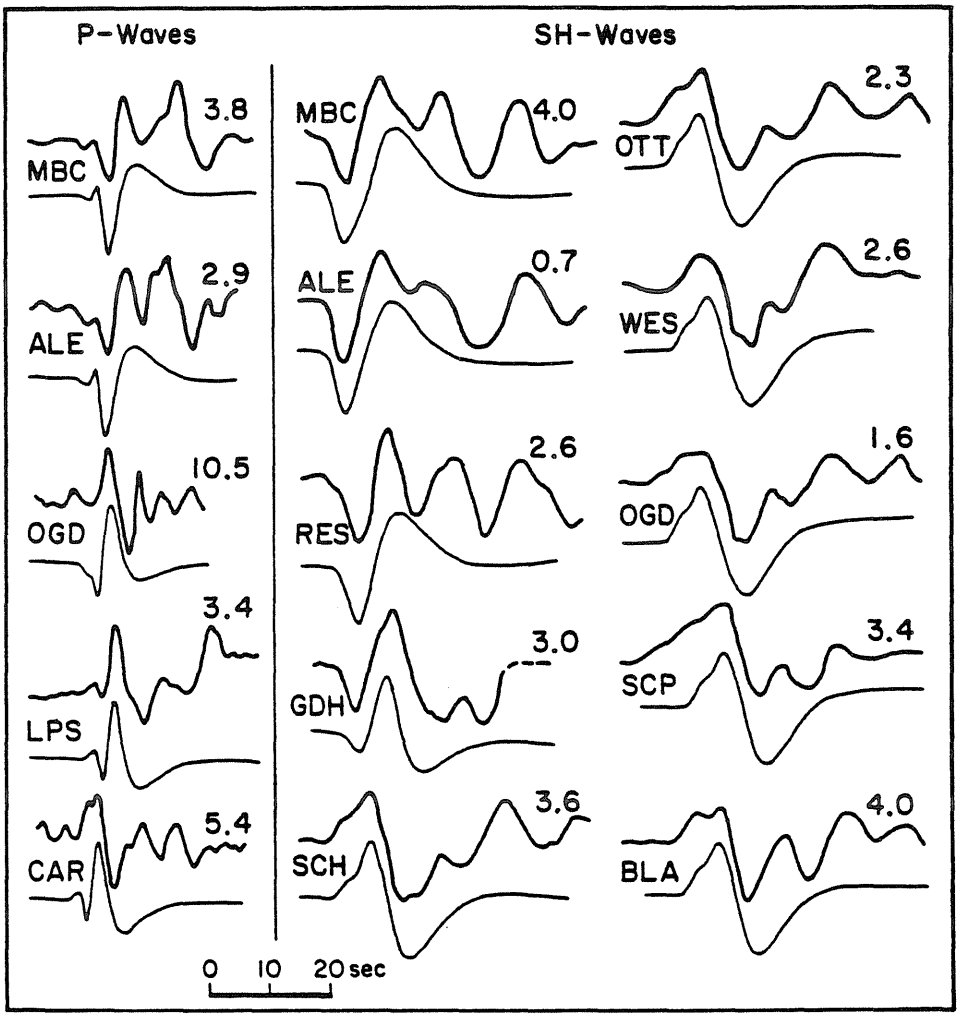

Figure 1-A-11 The teleseismically observed vertical P and SH waves vs. synthetics for the finite source model N1. The numbers indicate the seismic moment in units 10^{24} dyne-cm for each station.

Table 1-A-5 Teleseismic Stations Used in This Study

Station Name	Epicentral Distance	Azimuth	Component(*)
ALE	49.5	8.5	P-LZ, SH
BLA	32.6	77.1	SH
BOG	54.0	114.8	P-SZ
CAR	55.6	103.8	P-LZ,P-SZ
GDH	48.1	26.3	SH
LPS	36.7	119.7	P-LZ,P-SZ
MBC	39.2	.8	P-LZ,SH
OGD	36.3	68.9	P-LZ,SH
OTT	35.0	61.6	SH
RES	39.7	10.7	SH
SCH	40.8	46.3	SH
SCP	33.9	70.	SH
SJG	51.8	95.6	P-SZ
WES	38.5	66.1	SH

* P-LZ: Long-period vertical P component
P-SZ: Short-period vertical P component
SH: SH waves

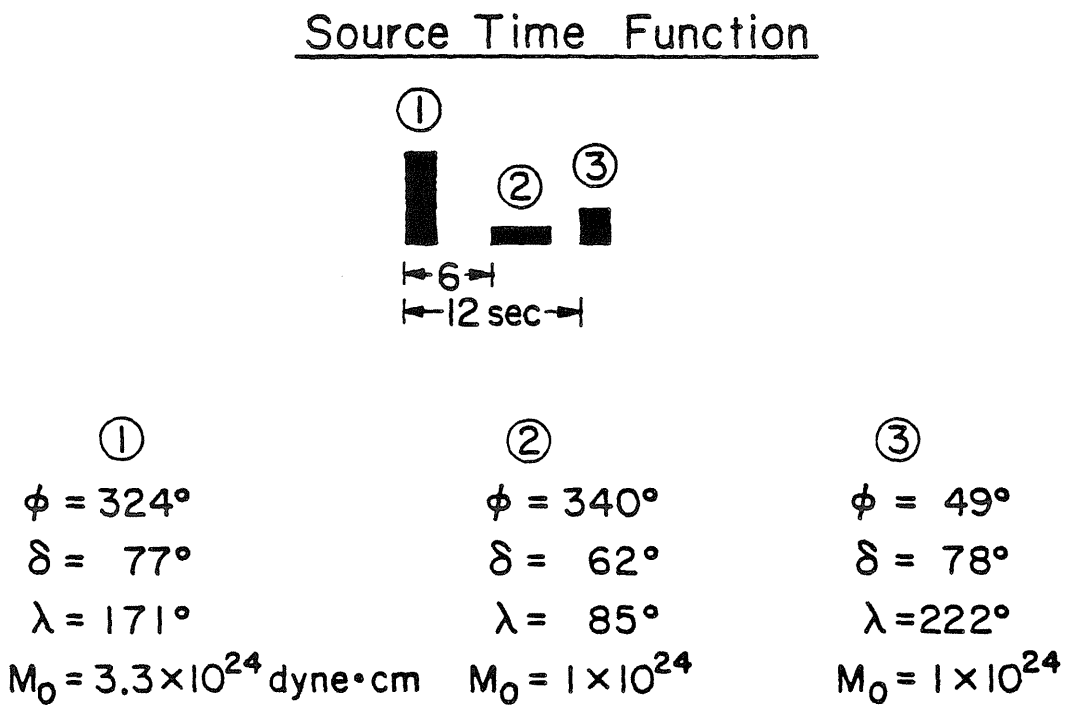

Figure 1-A-12 The multiple sources determined by Nabelek (1982).

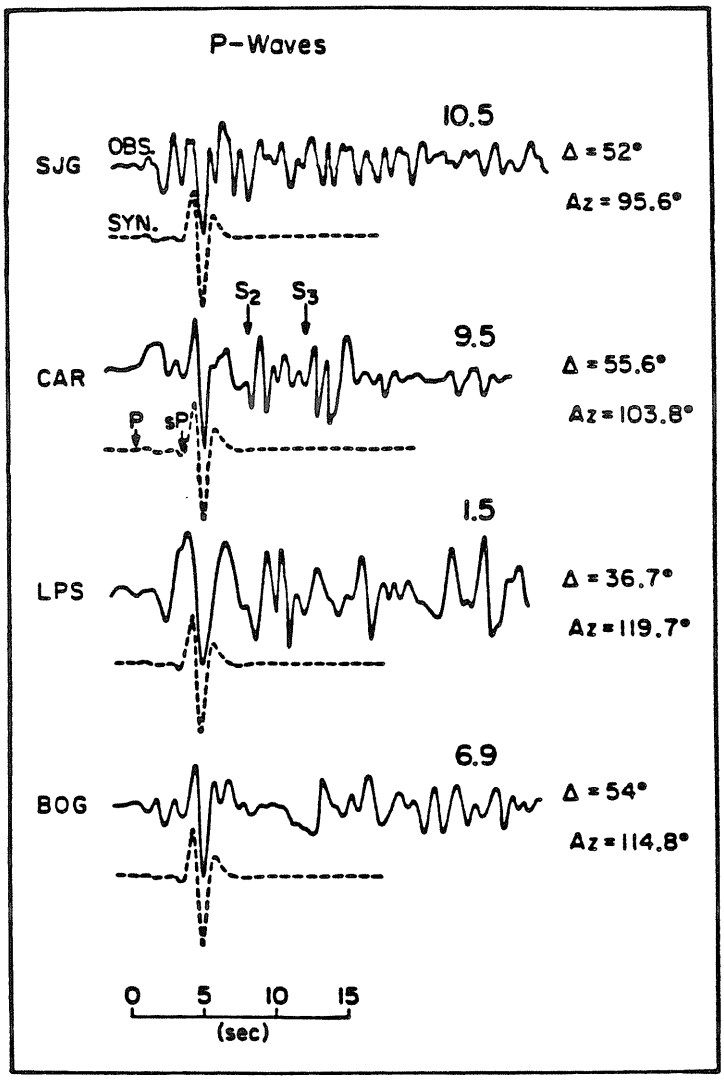

Figure 1-A-13 The teleseismic short-period vertical P waves and synthetics for the finite source model, N1. S_2 and S_3 at station CAR indicate the possible phases corresponding to the second and third events in Nabelek's solution. The numbers are the seismic moments in units 10^{24} dyne-cm.

20°. The impulsive arrivals seen about 3 secs after the direct P waves are very coherent and can be predicted by our finite source model as the sP phase. The seismic moment determined from the amplitude ratio is indicated for each station, and is higher than the averaged moment from the long-period waves. Station LPS may have some instrument calibration problem, since the response is not near 1 second. The later waves appearing in the seismograms (indicated as S_2 and S_3 at CAR in Figure 1-A-13) may be the second and third events according to Nabelek's solution, since the delay time is about 6 and 12 seconds, respectively . One of the more difficult problems in working with the short-period teleseismic data is the uncertainty introduced by the effects of velocity structure. In this study we simply use a half-space structure at both source and receiver; at the stations like Caracas (CAR), for which the structure appears rather transparent (Burdick and Langston, 1977), this approximation may be adequate. In spite of complexities, the teleseismic short-period data contain information which may provide close correlation with the near-source ground motions, particularly in the phases associated with high stress drop events.

Discussion

The source model we determined from the strong-ground motion data can predict reasonably well the P_{nl} waves in regional distances and the beginning features of the teleseismic seismograms. However, some questions are raised concerning a unified source model which can explain both near-field and far-field data simultaneously.

First, the basic difference between our preferred model N1 and Nabelek's mainshock solution is the 12° strike direction. The question is how well we can

resolve this difference from either near-field or far-field observations. We have generated P_{nl} waves from Nabelek's source orientation (strike = 324°, dip = 77° and slip = 171°); the major difference from model N1 appears at the nodal station DUG. However, neither our preferred model, N1, or Nabelek's solution could predict a satisfactory waveform at this station. A similar situation arises at the teleseismic nodal stations. Since the waveforms are barely above the noise level at these stations, we can not argue the resolution based upon them. For the strong ground motion data, the problem is different. The finite source model N1 is constructed with a fixed fault geometry (strike = 336°, dip = 80° and slip = 176°). As we mentioned earlier, some qualitative judgements about the waveform coherency and the radiation pattern are considered in the trial and error modelling process. If we simply use the same dislocation configuration of model N1 but adopt the fault orientation of Nabelek (1982), the amplitude of the radial component of the southeast station GA-6 increases, which is not consistent with the observations. On the other hand, the predicted amplitude ratio of transverse vs. radial for station GA-4 and GA-3 increases, which fits the data better. The signal duration and the waveshape can be reproduced on most of the stations reasonably well, except for the transverse component of station GA-4, which is near the SH node. Therefore we conclude that the most significant feature in our preferred finite source model N1 is the large final slip concentrated to the south of the hypocenter. The uncertainty of the fault geometry is not well resolved within the acceptable variation in the amplitudes.

Second, we raise a question of how distinguishable the far-field waveform can be for a uniformly distributed dislocation model. A close comparison of the source factors we have considered and their effects on the far-field waveforms

are discussed below.

Figure 1-A-14 shows the teleseismic synthetics for stations MBC, OGD, and CAR for four uniform dislocation sources, namely U1, U2, U3, and U4. The synthetics from model N1 are also displayed in the same figure for comparison. The variables in these four uniform dislocation models are the rupture velocity, the far-field rise time of the point dislocation and the hypocenter location. Based on a total moment of 3.5×10^{24} dyne-cm, the average final slip is estimated to be 17 cm for all the uniform slip models.

In model U1, the only difference from model N1 is the uniform slip. At the teleseismic distances, the long-period synthetic waveforms for U1 show no significant differences from model N1, however the amplitudes are slightly reduced. The short-period synthetics for N1 model suggest that the amplitude at CAR is about twice as large as at station MBC due to the southward rupture through a concentrated source. This may explain why only the South American stations recorded high short-period amplitudes. This amplitude contrast is no longer seen for model U1 when the source dislocation is uniformly distributed through a large fault, because the amount of one-second energy has been reduced. The observations at station CAR show that the amplitude ratio of short period to long-period is about 0.3, which is higher than the predicted of 0.16 in model N1, and 0.07 in U1. Although the synthetics are calculated using a half-space assumption and with $t_\alpha^* = 1$, the observed amplitude ratio indicates a high frequency source. We have shown earlier that the U1 model produces too broad and much longer signal durations for strong motion stations away from the fault, such as GA-4, GA-3, GA-2, and GA-1. Hence, in this case, the near source array data can provide the best constraints for identifying such a high frequency

source.

The U2 model has slower rupture velocity (2.0 km/sec). The teleseismic long-period synthetics have slight amplitude change but the waveforms are about the same as model U1. The short period synthetic seismograms have about 30% of the amplitude compared to U1 model and the waveforms are more complicated, due to the response to the longer rupture duration. In this case, the amplitude ratio of short-period vs. long-period at station CAR is about 0.02, which is about one order magnitude smaller than the observation.

In model U3, we consider slower rise time, triangular function of 1-second. The synthetic seismograms are quite similar to model U2, this simply implies that such difference in the source parameters is not resolvable teleseismically.

A symmetric rupture is shown in model U4, which has the hypocenter located in the center of the fault. Again, the long-period change is not very significant. The short period waveform at CAR has the feature of the concentrated source, but the amplitude is only about 10% of that in model N1.

These comparisons suggest that the teleseismic long-period data can hardly distinguish the difference between a uniform or non-uniform dislocation model for the presented fault size, but the short period data reveal quite significant amplitude differences. The short-period waveforms also show individual difference for some cases. However, in a real earth, these variations can easily be caused by other uncertain parameters, including the source/receiver structures.

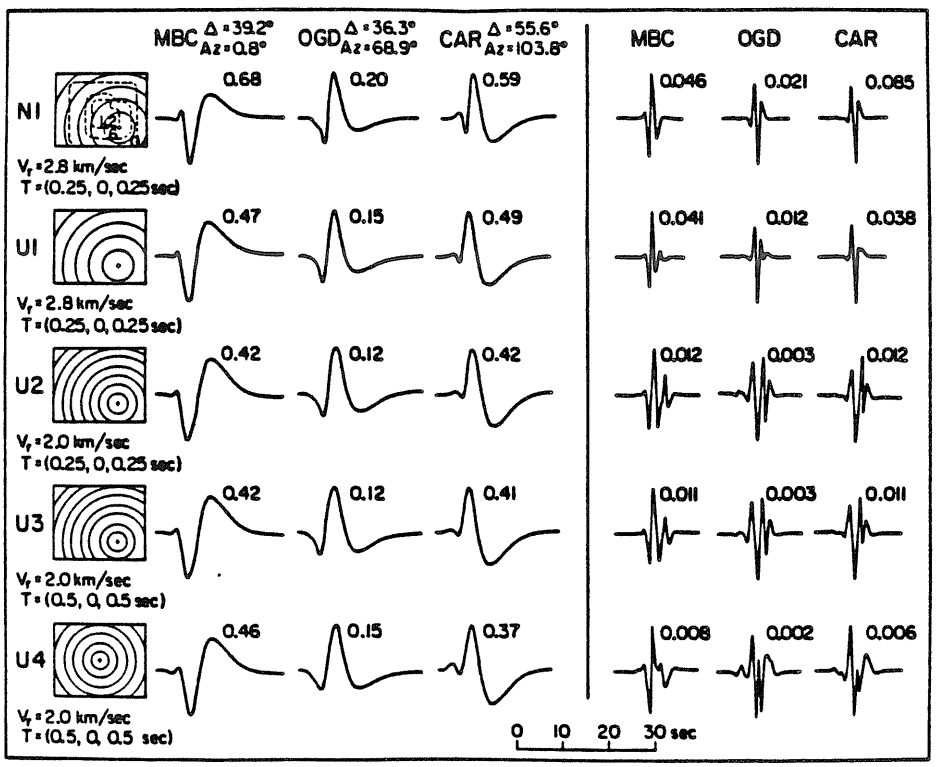

Figure 1-A-14 Synthetic comparison at the teleseismic stations for the uniform slip models, namely U1, U2, U3, and U4. Our preferred model N1 (see also Figure 1-A-7) is also illustrated. All the uniform slip models have a final dislocation of 17 cm along the fault surface. The circular rupture fronts are also illustrated. The numbers are the amplitudes in micrometers calculated for the seismic moment of 5.0×10^{24} dyne-cm.

Conclusion

We have learned from this study that the near-source array data can provide good constraints on source parameters. The strong ground motion array data from the 1979 Coyote Lake, California earthquake suggest that the source initiated at a depth of 8 km and with about 120 cm dislocation near the hypocentral area. The rupture is basically toward the south but vanishes after a rupture length of 6 km. The stress drop in the hypocentral area is about 140 bars, but averages about 30 bars over the entire rupture surface. The concentrated dislocation results in the high frequency enriched seismograms. Nabelek's (1982) inversion solution for the teleseismic data indicates that the Coyote Lake earthquake is a multiple event comprised of three separate earthquakes, in which the first event or the mainshock is characterized by high stress drop and short source time-duration. Our preferred finite source model reflects only this strong but short rupturing of the mainshock. No clear indication of the second and the third events can be found in the near-source ground motions.

1-B Near-Source Ground Motions of the 1966 Parkfield, California Earthquake

Introduction

The near-source ground motions of the 28 June 1966 Parkfield earthquake have been well documented but not well understood (Aki, 1979). The motive for reanalyzing this event arose because its local magnitude (M_L=5.6) and source-station geometry is similar to the 1979 Coyote Lake, California earthquake. Since local magnitude is a significant parameter for engineering problems, it is important to understand the similarities and differences of the source parameters for these two earthquakes.

In Table 1-B-1, we list source information from previous studies for these two earthquakes (Aki, 1968; Eaton et al., 1970; Lee et al., 1979; and Chapter 1-A, this thesis). Although the 1966 Parkfield earthquake has about the same local magnitude as the 1979 Coyote Lake event, its source process involved a much larger faulting area as suggested by its larger seismic moment and longer surface breakage. However, a final dislocation distribution has not been obtained which can explain the recorded near-source ground displacements (Lindh and Boore, 1981; Archuleta and Day, 1980).

In this study, we will first discuss the two contradictory models proposed respectively by Trifunac and Udwadia (1974) and Bouchon and Aki (1979) and compare the predicted synthetics to the observations. An alternative interpretation which considers the local site amplification effect will then be described to explain the observed data.

Table 1-B-1 Source Parameters

	Coyote Lake E.Q. (Calaveras fault)	Parkfield E.Q. (San Andreas fault)
Local Magnitude	5.9	5.6
Seismic Moment	3.5×10^{24} (dyne-cm)	1.4×10^{25} (dyne-cm)
Source Depth	8 km	6 km to surface
Mechanism	strike-slip right-lateral	strike-slip right-lateral
Aftershock Extending Length	16km	40 km
Surface Breakage	discontinuous	37 km
Static Offset	0.5 cm	4.5 cm (after 10 hours) 20 cm (1 month later)
Rupture Direction	toward south	toward south

The Ground Motions; A Review

Ground motions for the Parkfield earthquake were recorded by Cholame array (No. 2, No. 5, No. 8 and No. 12) and Temblor No. 2 station, which are located about 30 km south of the epicenter as shown in Figure 1-B-1. Both the surface rupture and the aftershock distribution indicate that the strike direction bends near the south of Gold Hill forming an enchelon pattern of faulting about 5 km north of the array stations. Thus the main faulting can be considered as having occurred on mainly two segments, a NE branch (about 22 km long, AA' in Figure 1-B-1) and a SW branch (about 8 km long, BB' in Figure 1-B-1), offset by about 1.5 km south of Gold Hill (see Figure 1-B-1). Therefore the ground motions will exhibit both source and structure complexities caused by rupture over about 30 km long fault. We will ignore northward rupturing which contributed little to these recordings. As shown in Figure 1-B-2, the horizontal ground velocities for the Parkfield earthquake are much more complicated than those seen in the Coyote Lake earthquake. The data shown in Figure 1-B-2 are rotated to be transverse and radial relative to the epicenter. Station Cholame No. 2 recorded only one horizontal component, which is nearly perpendicular to the strike of the fault trace and thus representing mainly transverse motion relative to the epicenter.

The basic question is whether the ground motions are mainly due to the dislocation near the epicentral region, along the NE fault branch, or due to the dislocation close to the station sites , along the SW fault branch.

Aki (1968) and Bouchon and Aki (1979) favor the model in which the dislocation is important only in the segment near the station Cholame No.2 (CH2). Their argument is based on a modeling study of the anomalous ground

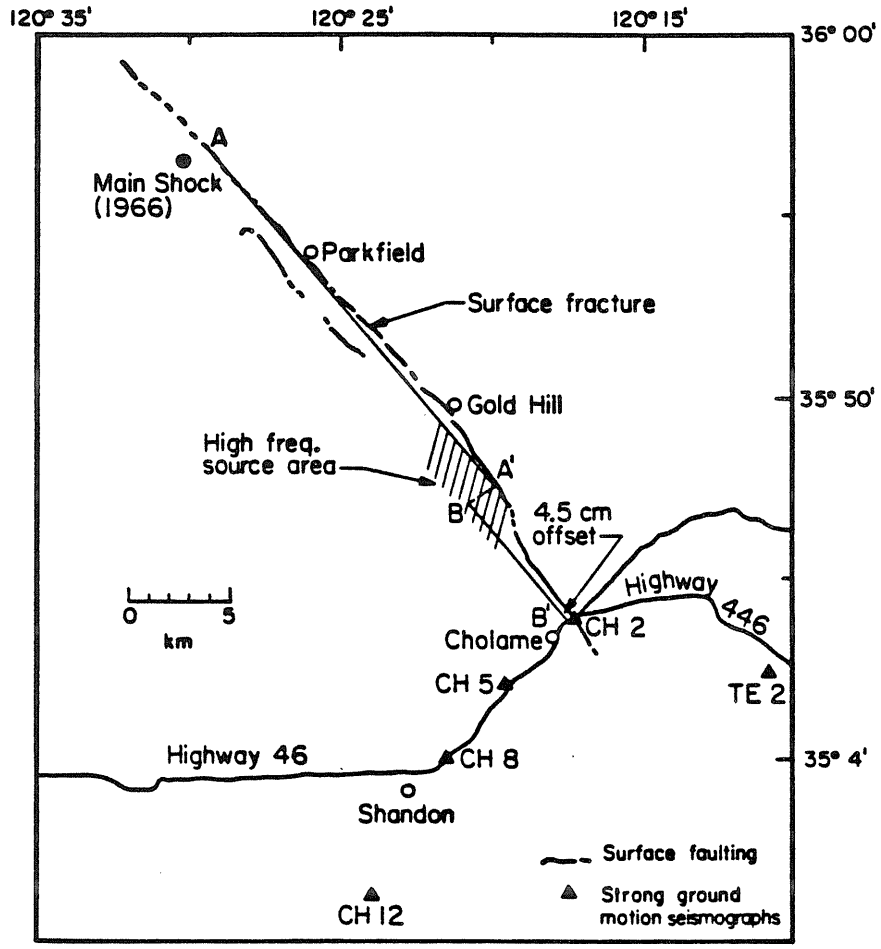

Figure 1-B-1 Map showing the mainshock location of the 1966 Parkfield earthquake and the recording sites, including CH2, CH5, CH8 and CH12 (Cholame array) and TE2 (Temblor No.2).

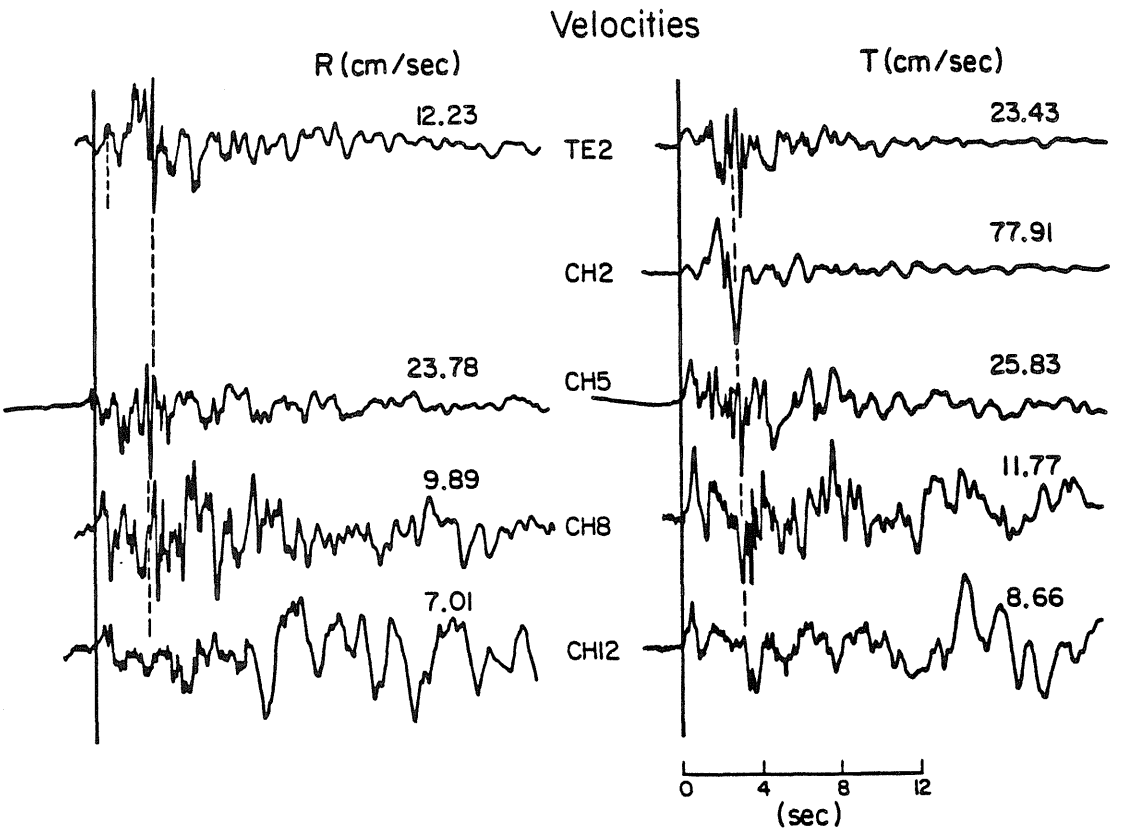

Figure 1-B-2 The radial and transverse ground velocities from the 1966 Parkfield earthquake.

displacement (245°-component) recorded at station Cholame No. 2. As shown in Figure 1-B-3, the amplitude of the ground displacement at CH2 is 3 times larger than either CH5 or TE2. Furthermore, the waveform at CH2 is quite different from the other recordings. Apparently only body waves were recorded at CH2. A large dislocation very near the station CH2 on the SW branch is required to suppress the surface waves. Also, the maximum surface offset of 4.5 cm, measured 10 hours after the mainshock was near station CH2 (see Figure 1-B-1). This further suggests that the main dislocation is near CH2. However, the relation between the static offset observed at the surface and the dislocation at depth is not well understood.

On the other hand, Trifunac and Udwadia (1974) invert for the dislocation distribution using all the recorded data and assuming a homogeneous half-space velocity structure. They conclude that major dislocation was near the hypocentral region and extended about 20 km southwardly, which is mainly along the NE branch. This solution is also supported by Lindh and Boores' timing argument (1979). Lindh and Boore estimate the direct S arrivals by aligning the high frequency phases (indicated by dashed lines in Figure 1-B-2) seen in accelerations and velocities. They conclude that the phases corresponding to the peak acceleration or velocity at all stations arrived from the area near Gold Hill, about 10 km north of station CH2. They also suggest that this high frequency motion corresponded to the stopping of the faulting process, hence most of the dislocation occurred north of Gold Hill. However, a model in which most of the dislocation is concentrated on the NE branch will produce strong surface waves and much broader and smaller seismogram for station CH2, which contradicts the observation.

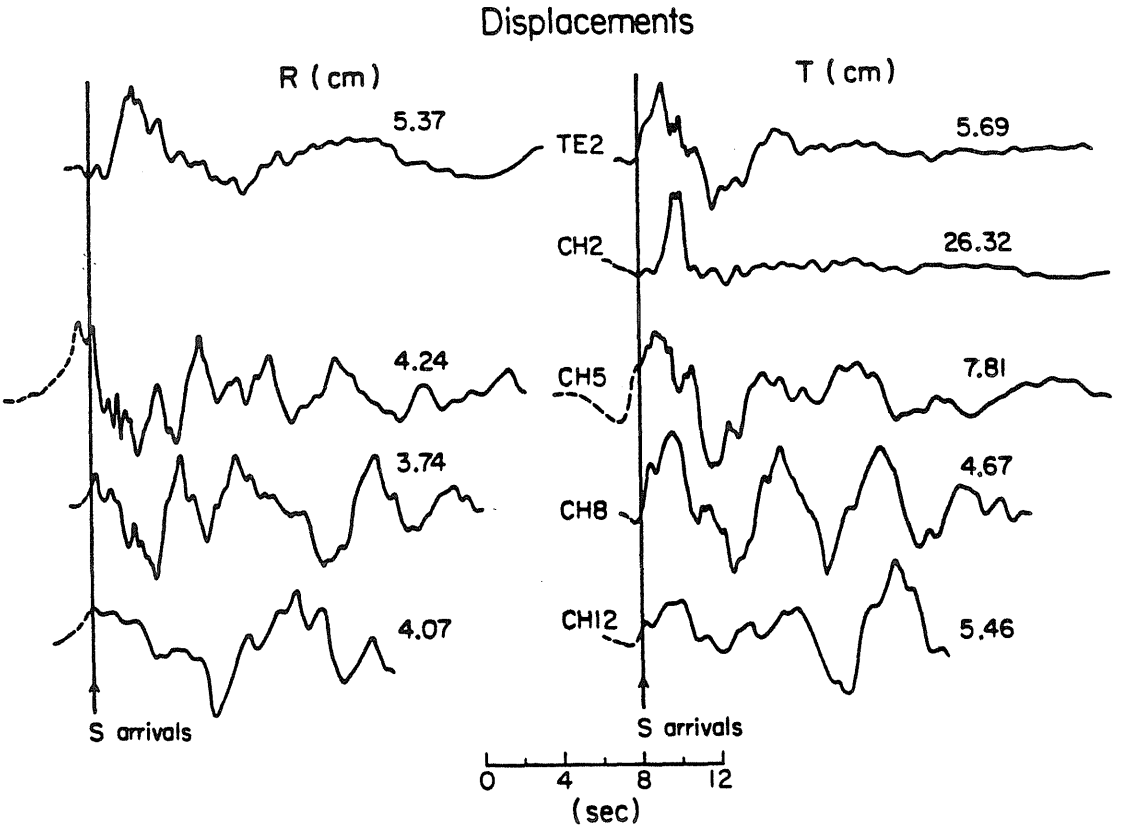

Figure 1-B-3 The radial and transverse ground displacements from the 1966 Parkfield earthquake. The traces are aligned by the apparent S phases determined from the coherent arrivals seen in the transverse velocities.

Apparently, it has been very difficult to derive a consistent solution by only adjusting the dislocation distribution and rupture velocity along the fault. We will instead consider local amplification factor at station CH2 as an explanation for its anomalous waveform as suggested by Lindh et al's amplitude test study (1982). They installed a local seismograph array at these strong ground motion recording sites and found that station CH2 recorded higher amplitudes (about 1.5 times) than the neighboring stations, CH5 and CH8. They suggest that the high amplitude waveform at station CH2 may have resulted from such local amplification and perhaps some complicated interference effects.

We will show comparisons of the observed and synthetic waveforms from models proposed respectively by Bouchon and Aki (1979) and Trifunac and Udwadia (1974) based on a layered structure calculation. We will then discuss a solution which considers the local amplification effect for station CH2.

Waveform Modeling

The velocity structure modified from Eaton (1966), as illustrated in Figure 1-B-4, is used to generate Green's functions. The structure responses are calculated for frequencies up to 1 Hz using discrete wavenumber finite element method (Olson, 1982). A 1-second triangular time function is used to represent the time derivative of the dislocation history of each point on the finite fault. The fault geometry is illustrated in Figure 1-B-5, in which both NE and SW branches are projected on the same vertical plane. The surface traces of these two vertical faults are about 1.5 km apart as indicated in Figure 1-B-1. Synthetic ground displacement is the sum of the responses to point sources distributed along the finite fault with proper time lags due to circular rupture delay.

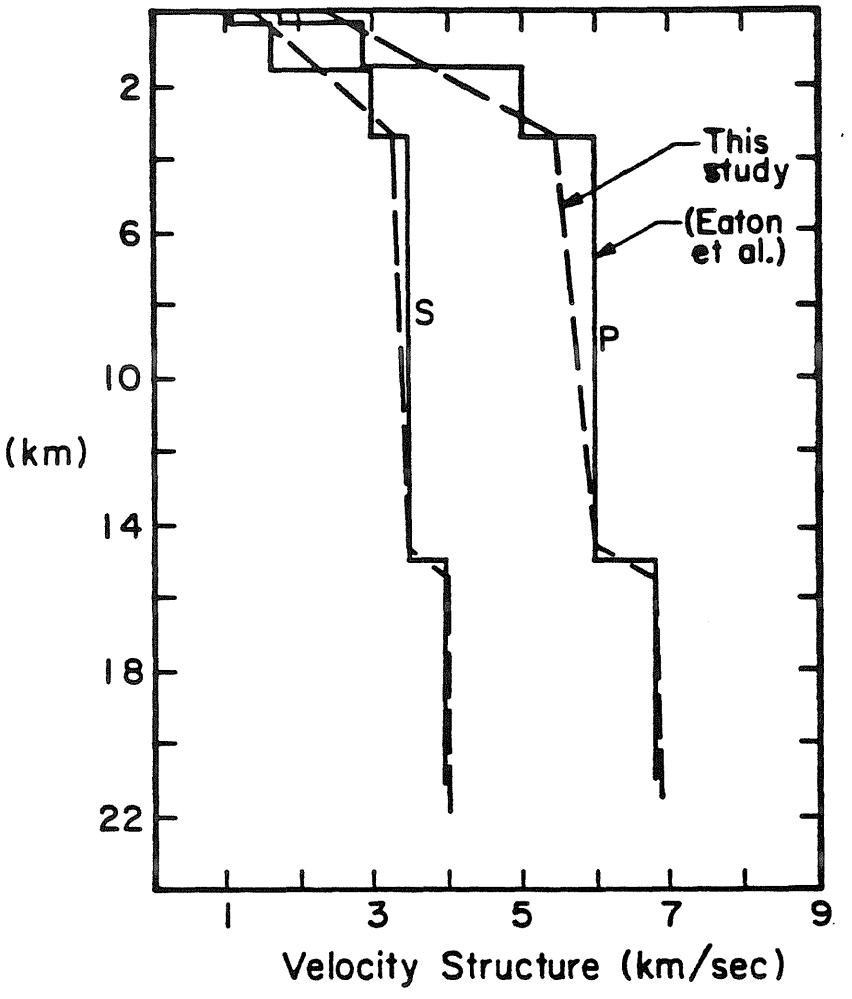

Figure 1-B-4 The gradient structure used to calculate the Green's functions.

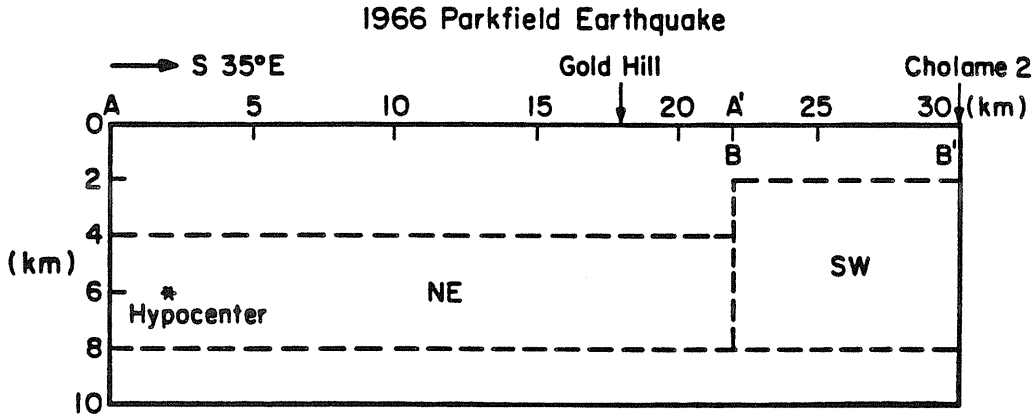

Figure 1-B-5 The vertical projections of both NE fault branch and SW fault branch (see Figure 1-B-1 for AA' and BB').

A constant rupture velocity of 2.5 km/sec is used in the calculation.

Figure 1-B-6 displays the data and synthetics computed for a finite fault assuming a uniform dislocation distribution confined to the NE branch. The total moment is 1.0×10^{25} dyne-cm. This model is essentially that of Trifunac and Udwadia (1974), with the effects of a layered velocity structure included. The transverse synthetic seismogram for station Cholame No. 2 exhibits a much broader waveform and stronger surface waves than the observed displacement. Furthermore, the calculated amplitude at station CH2 is much smaller than the observed amplitude. Since we use layered velocity structure, surface waves are much larger at station CH2 than shown in Trifunic and Udwadia (1974). This is also the basic argument that Aki (1979) and Bouchon and Aki (1979) suggest that a large amount of dislocation should have occurred near station CH2, generating high amplitude body waves. For most other components, the synthetics match the data reasonably well.

Figure 1-B-7 illustrates the synthetics computed for a uniform dislocation on the SW fault branch. The total moment is also 1.0×10^{25} dyne-cm. Consistent with Bouchon and Aki (1979) , the model predicts better waveform for the transverse component at station CH2, in which the surface waves are suppressed and the signal duration is shortened. However, for other components, this model does not predict the observed waveforms. First, the amplitude of body waves are much too large at station CH5. Second, contrary to the observations, the computed transverse waveforms for station TE2 show no resemblance to the waveforms at station CH5. Third, synthetics for the radial components at stations CH5 and CH8 are quite different from the observations.

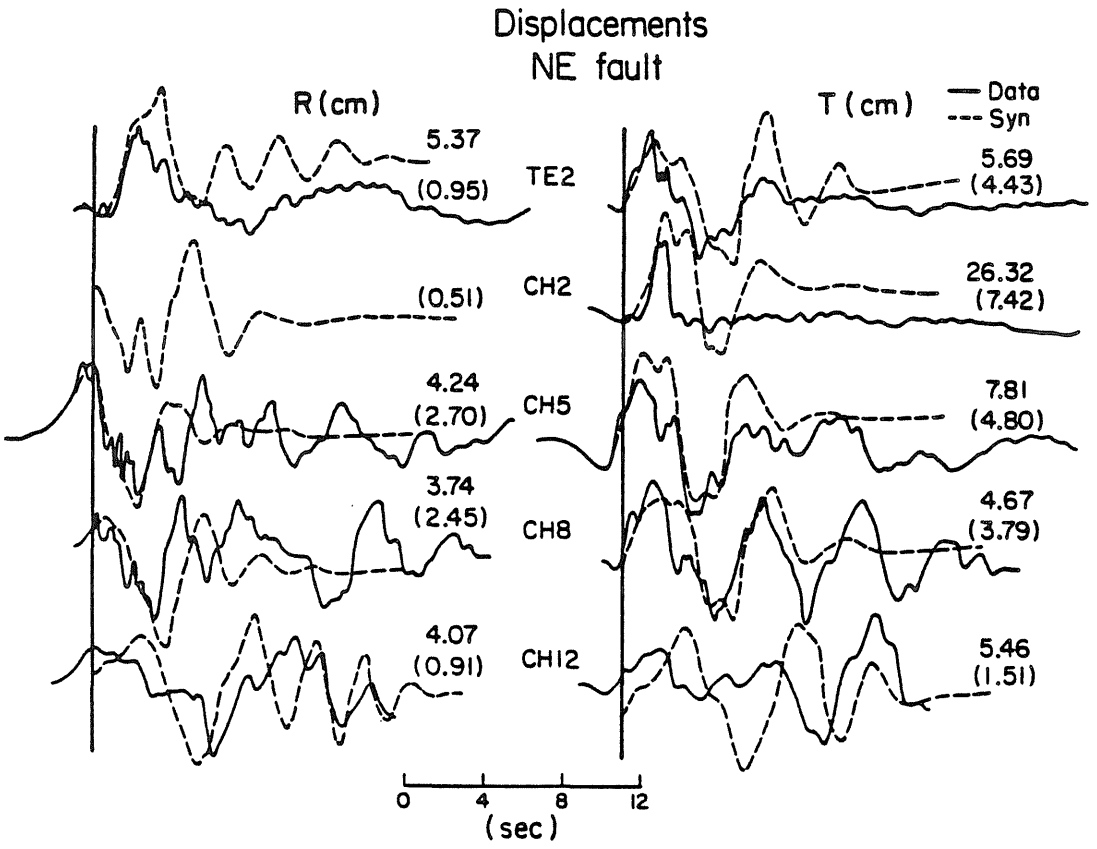

Figure 1-B-6 The comparison of the data (solid traces) vs. synthetics (dashed traces). The synthetics are generated from the NE fault segment for the moment of 1.0×10^{25} dyne-cm.

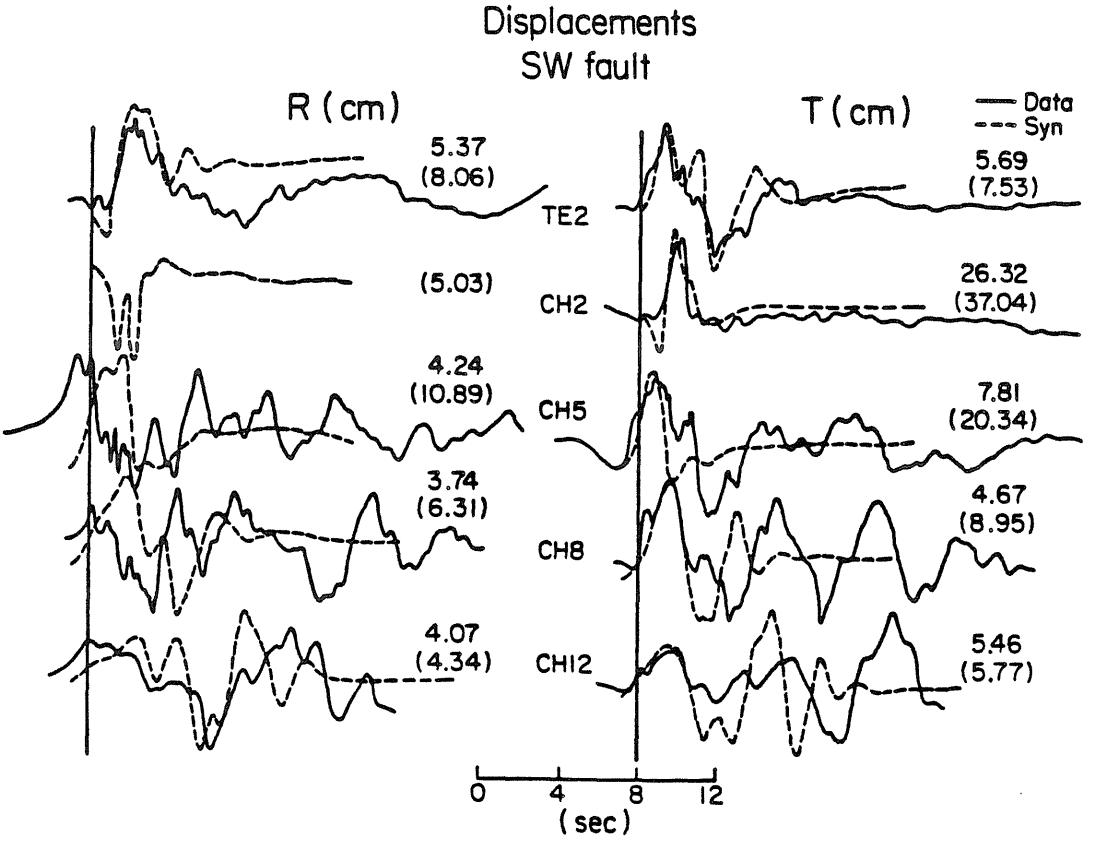

Figure 1-B-7 The comparison of the data (solid traces) vs. synthetics (dashed traces). The synthetics are generated from the SW fault segment for the moment of 1.0×10^{25} dyne-cm.

Thus, confining the source dislocation to the SW fault branch provided a better solution only for the transverse component at station CH2. Most of the other components favor the solution in which dislocations occurred along the NE branch. In order to find a solution that allows all the data besides CH2 to be dominated by the dislocation on the NE fault branch, yet maintains the waveform at CH2, we have tried different combinations of displacements on both NE and SW fault branches for all these stations. Figure 1-B-8 shows the waveforms produed at CH2 for different moment combinations from these two fault branches. Four seismic moment ratios of SW fault branch to NE fault branch, 0.125, 0.25, 0.5, and 1.0, are compared. At station CH2, a moment ratio of 0.5 can produce a reasonable waveform and amplitude on the transverse component. However, for other station components, 0.25 is the best ratio. Hence, if we allow a factor of 2 local site amplification at station CH2 from the SW fault branch, we can obtain a reasonable dislocation model, which the resulting synthetics can match the data well in all the stations. The data vs. synthetics from this model are shown in Figure 1-B-9. In this solution, the total moment is 1.25×10^{25} dyne-cm. The average slip is about 45 cm in the NE fault branch and about 21 cm in the SW branch.

Discussion

From the waveform modeling of the 1966 Parkfield earthquake, we concluded that the Parkfield earthquake is an event involving dislocations along two fault segments, although the resolution of details is rather poor due to the station distribution. It is significant to compare directly the waveforms recorded in the Parkfield earthquake with those recorded in the 1979 Coyote Lake

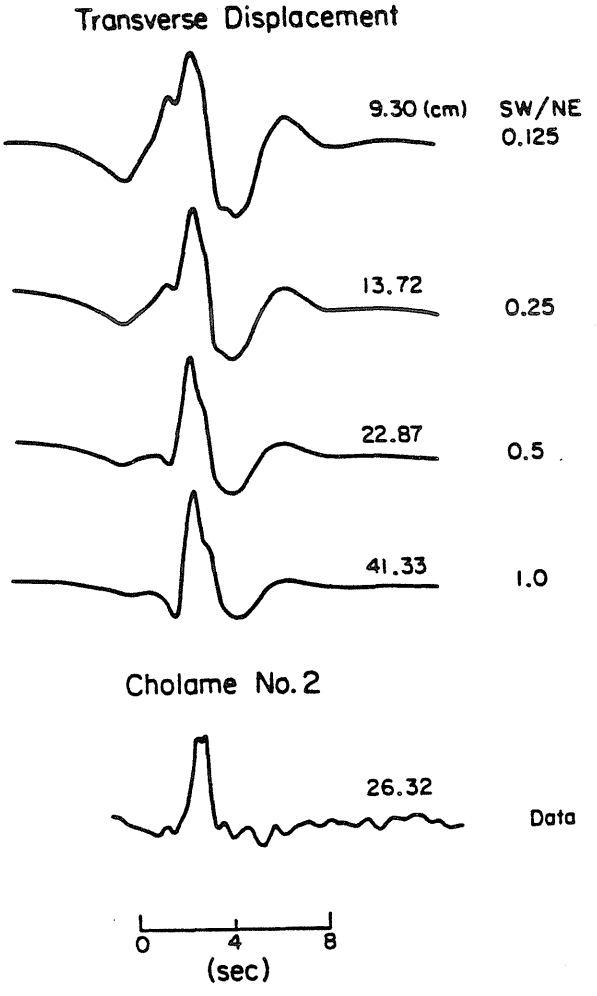

Figure 1-B-8 The comparison of various contributions from both SW and NE fault segments. The ratios of seismic moment of SW branch to the NE branch are indicated in the right column.

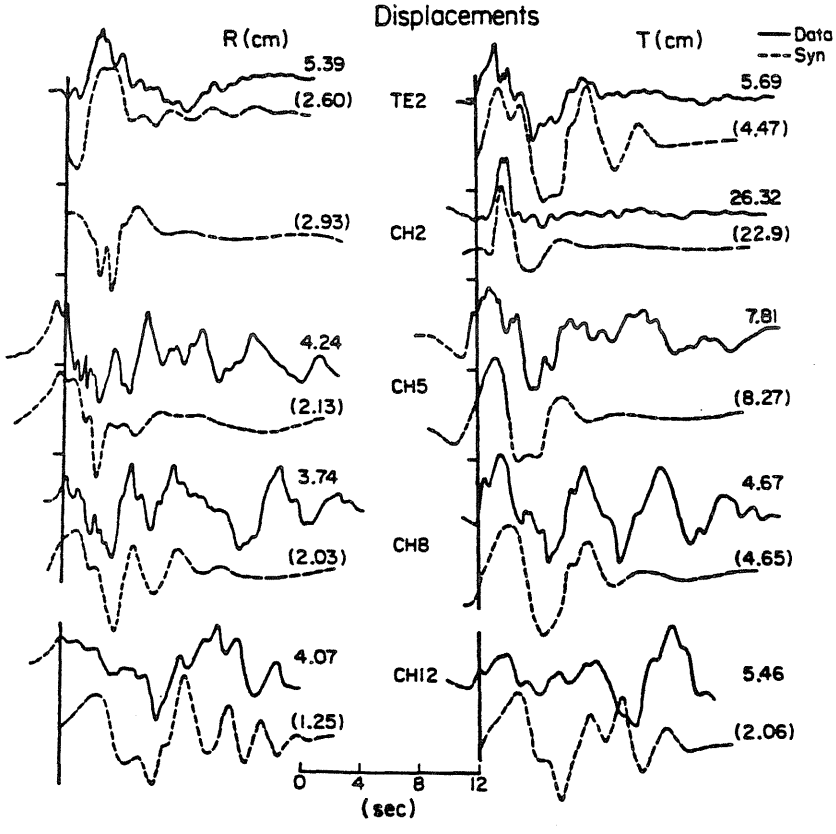

Figure 1-B-9 Comparisons of data (displacements) vs. synthetics from our preferred solution. The solution contains the dislocation from both NE and SW fault segments with a total moment of 1.25×10^{25} dyne-cm. The average slip in the NE segment is 45 cm and about 21 cm in the SW segment. A local site amplification factor of 2 needs to be added for station CH2 in the SW fault segment.

earthquake, in which the major dislocation is distributed over about a 6 km long fault. Although the source-station geometries are similar for both events, resolution of the source parameters for a smaller fault such as the 1979 Coyote Lake event is much better.

In Figures 1-B-10(a) and 1-B-10(b), we show the ground motions recorded very near the fault and about 5 km away from the fault to demonstrate the waveform differences observed between long faulting (Parkfield earthquake) and short faulting (Coyote Lake earthquake). As shown in 1-B-10(a), the 245°-component observed at station Cholame No.2, about 80 m from the fault is similar to the 230° component of station Gilroy No. 6, which is located less than 1 km from the Calaveras fault. These two components represent mainly transverse ground motions from predominantly right-lateral strike-slip faultings. We recognize that a station located on the fault cannot resolve fault size because of the rupture directivity effects. For stations about 5 km from the fault, shown in Figure 1-B-10(b), the waveform difference seen between stations Cholame No.5 and Gilroy No.4 is quite significant due to different faulting size. This comparison also verifies that the energy release during the 1979 Coyote Lake earthquake was of an asperity type, whereas the 1966 Parkfield event is a combination of long faulting and a small asperity rupture which producing the peak accelerations and associated peak velocities. It is also suggested that the small asperity in the Parkfield earthquake contributes little to the main feature of the displacements observed at most stations due to its high frequency nature.

The lack of good recordings at teleseismic distances makes it difficult to compare the difference for these two events in the far-field. However, the short-period seismograms from stations CAR and SJG shown in Figure 1-B-11

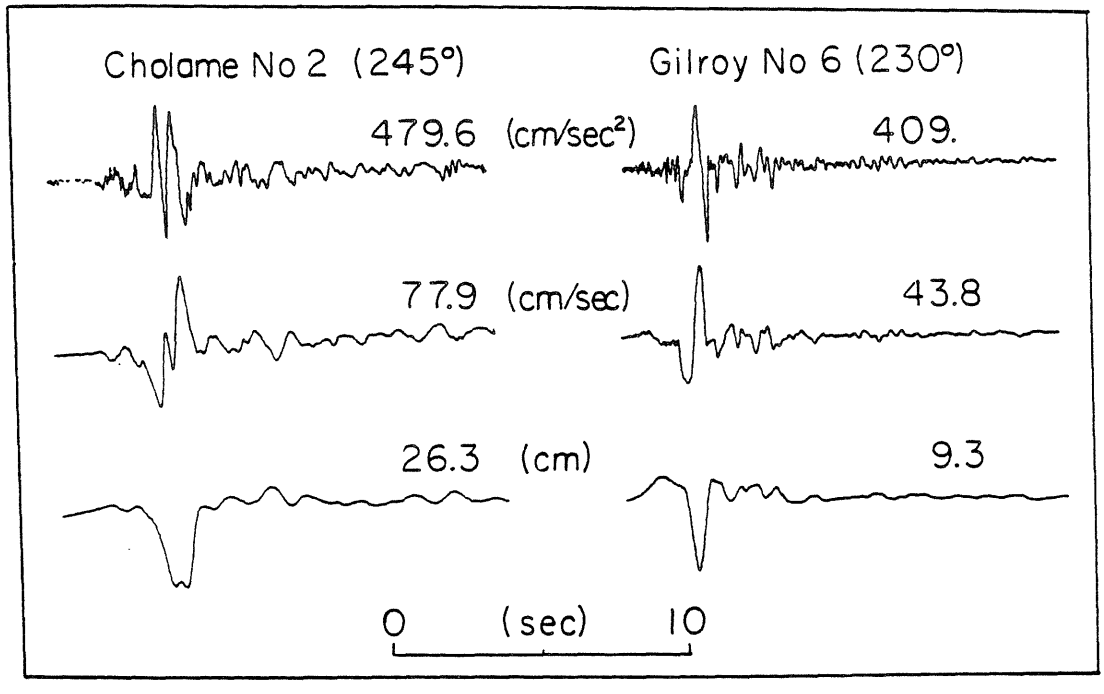

Figure 1-B-10(a) The comparison of the ground motions recorded near the fault from the 1966 Parkfield earthquake (Cholame No.2, 245°) and the 1979 Coyote Lake earthquake (Gilroy No. 6, 230°).

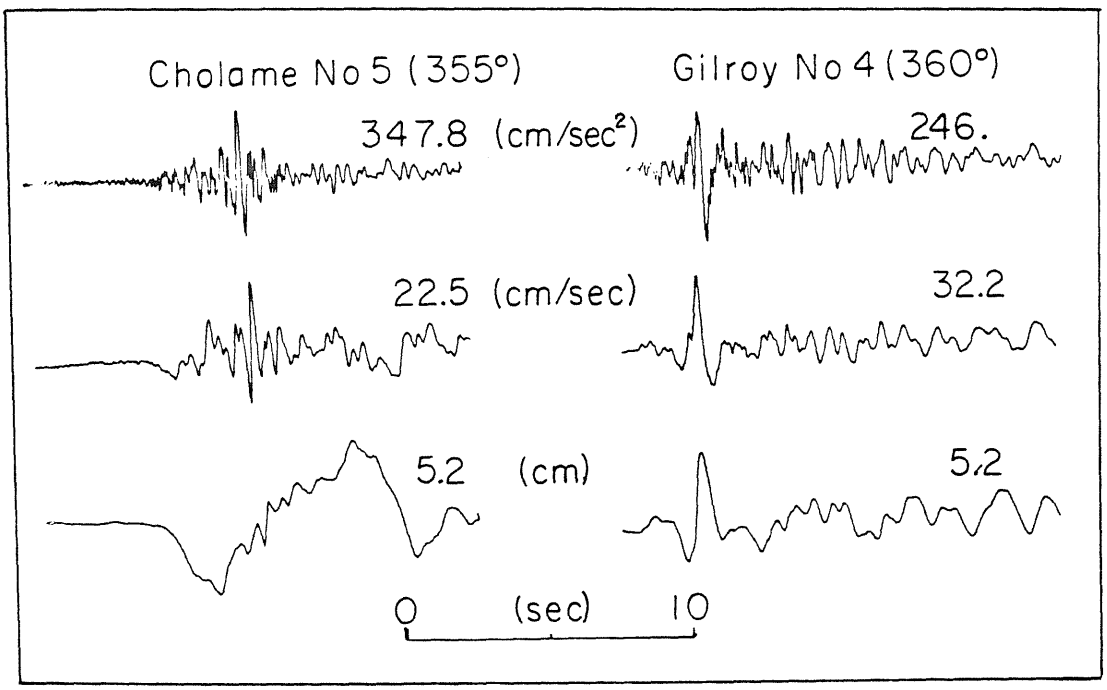

Figure 1-B-10(b) The comparison of the ground motions recorded about 5 km away from the fault from the 1966 Parkfield earthquake (Cholame No.5, 355°) and the 1979 Coyote Lake earthquake (Gilroy No. 4, 360°).

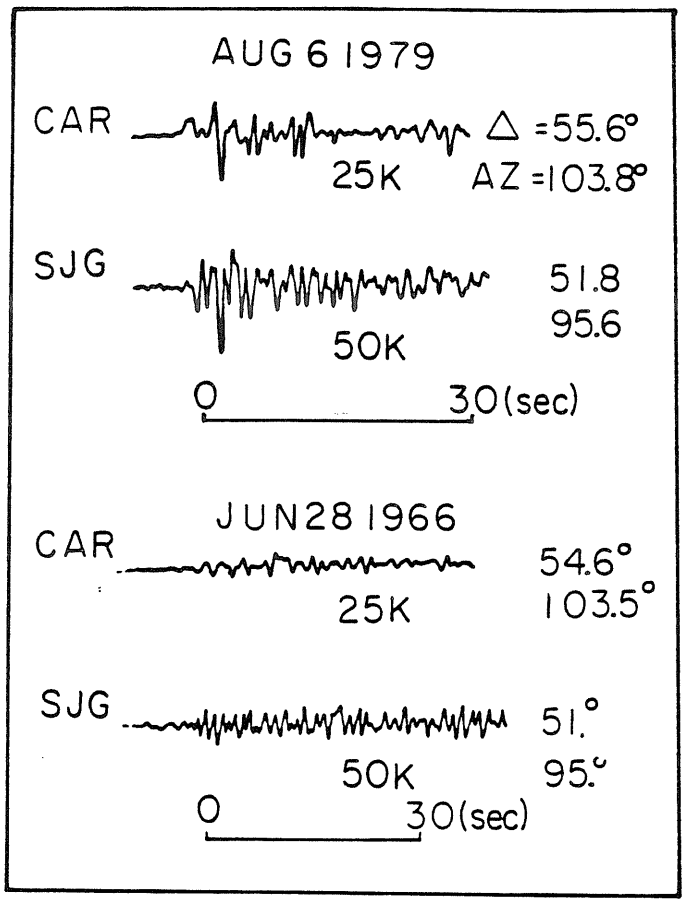

Figure 1-B-11 The comparison of short-period P waves for the 1966 Parkfield earthquake and the 1979 Coyote Lake earthquake recorded at CAR and SJG. The instrument magnification (25K for station CAR and 50K for station SJG) is also indicated.

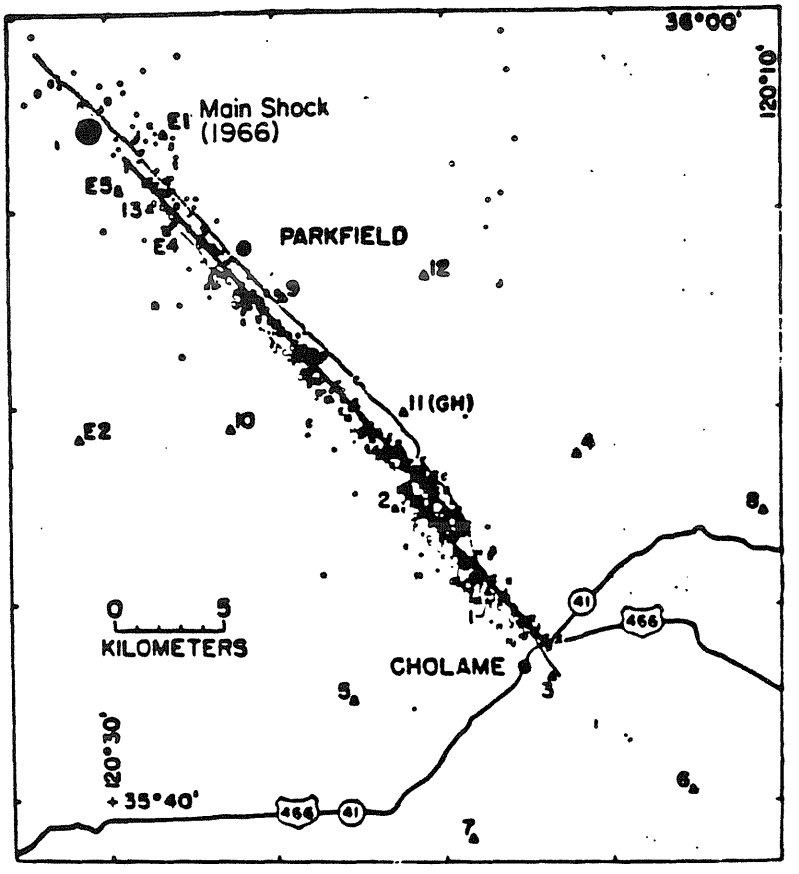

Figure 1-B-12(a) The aftershock seismicity for the 1966 Parkfield earthquake (after Eaton et al, 1970).

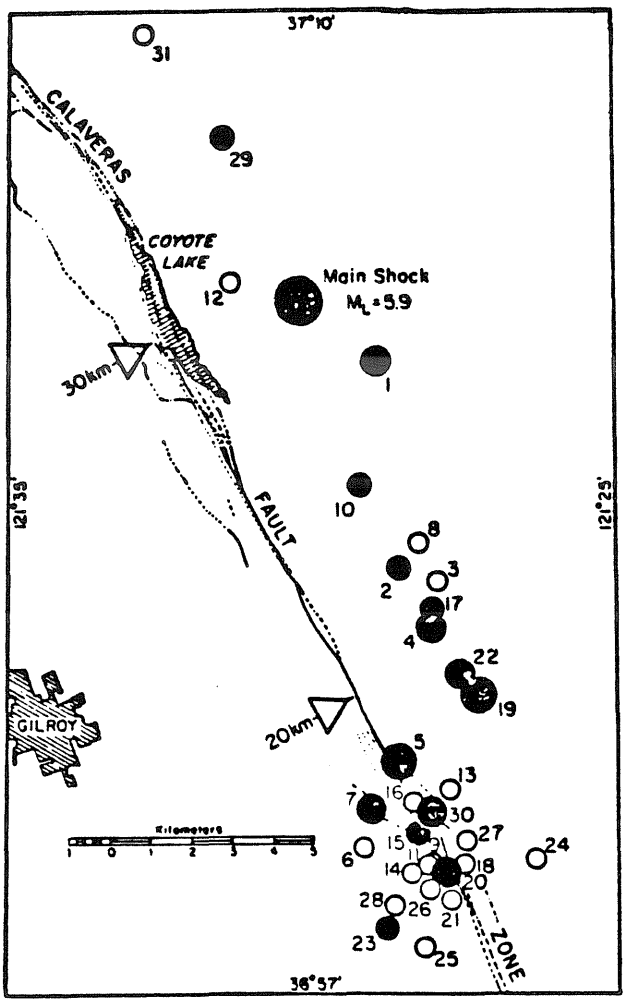

Figure 1-B-12(b) The aftershock seismicity for the 1979 Coyote Lake earthquake (after Uhrhammer, 1980).

suggest that the 1979 Coyote Lake event has a high amplitude phase corresponding to its source asperity and that the 1966 Parkfield earthquake has no such feature.

In spite of the difference in dislocation distributions , the Parkfield earthquake and the Coyote Lake earthquake have very similar aftershock seismicity patterns, as shown in Figures 1-B-12(a) and 1-B-12(b). Both events show echelon type of seismicity distribution, suggesting that there are offsets near the southern ends of the faults. Aki (1979) proposes a barrier model for the 1966 Parkfield earthquake, in which somewhat different rock property or stress field stops the rupture in an abrupt way producing high accelerations. This may also be applied to explain the high peak acceleration observed in Coyote Lake event. This waveform modeling study suggests that the 1966 Parkfield earthquake ruptured through a barrier and reduced half of its slip rate along the second fault segment. The earthquake source motion of the 1979 Coyote Lake event was terminated by perhaps a similar type of barrier, which did not break during the main event.

Conclusion

Waveform modeling of the near-source ground displacements suggests that the 1966 Parkfield earthquake involved two segments of faulting. The NE segment, extending 22 km southward from the epicenter had about 45 cm slip. The SW segment, the branch near the recording sites, had an average slip of about 22 cm. The resolution of detailed source parameters is rather poor due to the length of the fault and small areal extent of the recording array. In order to explain all of the recorded seismograms, dislocations from both segments need

to be included. Furthermore, a local site amplification factor of 2.0 needs to be added to interpret the anomalous seismogram recorded at Cholame No.2. Comparisons of waveforms between the Parkfield event and the Coyote Lake 1979 earthquake also support the conclusion that the Parkfield earthquake ruptured through a much longer segment of fault.

Chapter 2 Modeling the High Frequency Ground Motions from Aftershocks

2-A A Note on the High Frequency Vertical Strong Motions Recorded in Sedimentary Basins; The El Centro Aftershock of October 16, 23:16, 1979

Introduction

It has been noticed by seismologists and earthquake engineers that some strong ground acceleration data recorded in soft rock sites often show significant difference in the frequency content of the vertical and horizontal components. It is rather surprising that the highest accelerations recorded so far from strong-ground motion instruments are on the vertical components. One example is the accelerogram in El Centro station 6 (USGS), recorded during the October 15, 1979 Imperial Valley earthquake with a peak acceleration of 1.74 g on the vertical component and 0.45 g and 0.72 g on the horizontal components. Also the frequency content in the vertical component is much higher than that in the horizontal components (Brady and others, 1980). Another similar case is the Gazli, USSR earthquake of May 17, 1976, which generated a peak vertical acceleration of 1.3 g yet the peak horizontal acceleration at the same site was about one-half of that. The source was in western Kysylkum Desert, a region with at least 1-km thick sediments (Hartzell, 1980). These examples suggest that the above phenomenon is caused by the velocity

structure of basins. We investigate this supposition in this brief report. In order to avoid the complexity of the large earthquake source, we chose to examine acceleration data from an aftershock of the 1979 Imperial Valley earthquake (October 16, 23:16; M_L=4.9). These observations exhibit the anomalous ratio of vertical to horizontal peak accelerations but with relatively simple source process.

Data

The aftershock distribution in the source area of the October 15, Imperial Valley earthquake implies a change from strike-slip to normal fault mechanisms in the conjugate structure near Brawley (Johnson and Hutton, 1981). The epicenter of the October 16, 23:16 aftershock is located at 33.023° N and 115.49° W as determined by the Southern California Network. The focal mechanism determined from local stations indicates normal faulting with a strike of N40° E, a dip of 40° SE and a rake of -80°, see Figure 2-A-1. Too few teleseismic data are available to determine the focal mechanism independently. However the station FVM (French Village, Missouri), which is about 21° away from the source with an azimuth of N69° E, recorded very low amplitude Love waves. According to the local focal mechanism, FVM should be close to a node of the Love wave radiation pattern. For the November 4, 1976 Brawley earthquake, a similar size strike-slip event in the same region, FVM lies on a maximum of the SH radiation pattern and recorded Love waves which were about 5 times larger. From the comparison of these two observations we have good support for a normal mechanism of this earthquake from regional data.

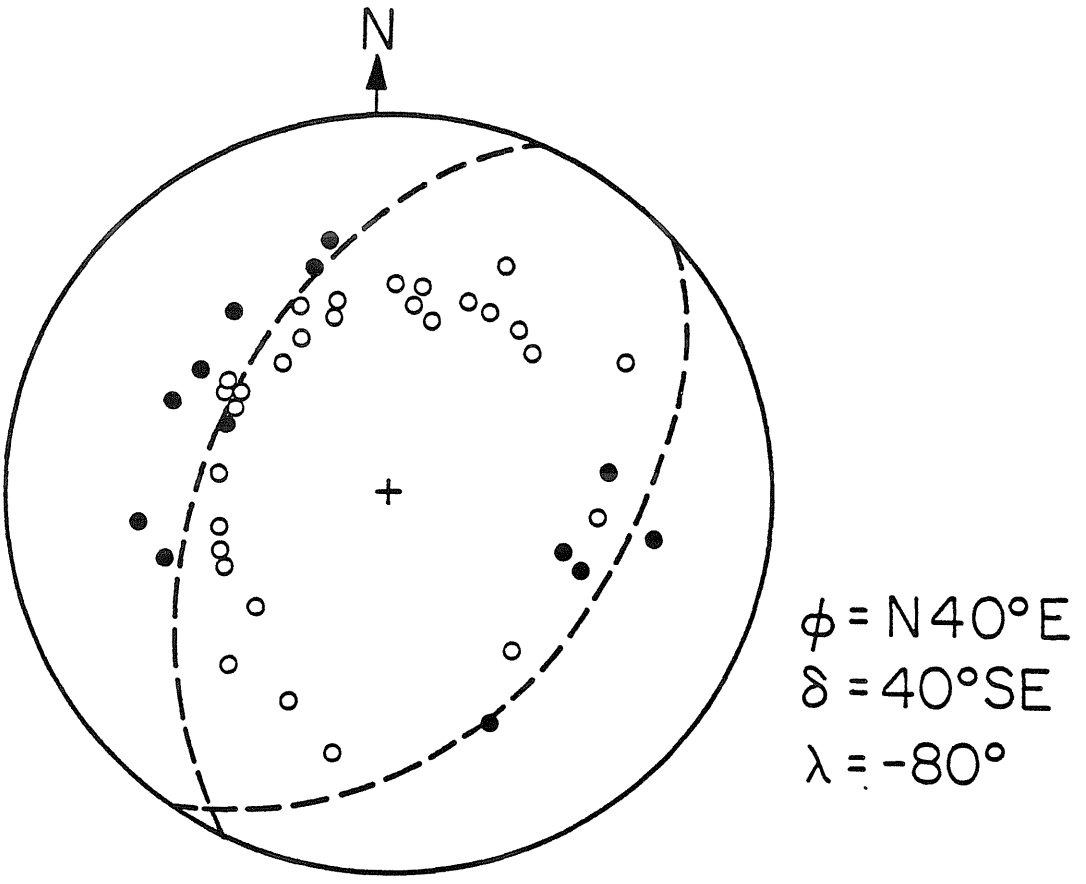

Figure 2-A-1 The first P-motion focal mechanism with strike of N 40° E, dip of 40° SE and slip angle of -80°. Only stations with clear first motion are plotted.

Strong ground motion data for this event were recorded by a temporary array. Details of this array and the accelerographs are discussed in the paper by Anderson and Heaton (1979). Figure 2-A-2 shows the station locations and the epicenter. Only the stations Del Rio Country Club (3698), Brawley Airport (3689), and San Etchegarry (3692) recorded ground motion large enough to distinguish their phase arrivals well. Table 2-A-1 lists the station locations, epicentral distances, and the peak acceleration, velocity and displacement for each component. The recorded accelerograms for the three closest stations are displayed in Figure 2-A-3. The relative station location to the epicenter and their horizontal instrument orientation are also indicated. In the beginning of the horizontal components, stations 3698 and 3689 show some long-period drifts which appear to be the near-field P-waves. For a magnitude 4.9 earthquake, these short, simple S phases (about 1.5 seconds) indicate that the recorded signals represent basically the motions of earthquake source.

For this particular aftershock, we summarize that the so-called high frequency contrast between P and S waves. (1) The dominant frequency of the P waves is around 20 Hz and about .5 to 1. Hz in S waves. As pointed out by Anderson and Heaton (1979), due to the standard data processing, the frequency and amplitude have been reduced on the vertical components. (2) The high frequency, high amplitude vertical components are predominantly P waves. The longer period horizontal components are mainly S waves. (3) The epicentral distances for these stations are about 2 km to 5 km. This paper will concentrate on how we can simulate these features by a proposed basin velocity model. The effects of this velocity structure and attenuation as well as the nature of the earthquake source are basic keys to explaining this frequency contrast feature.

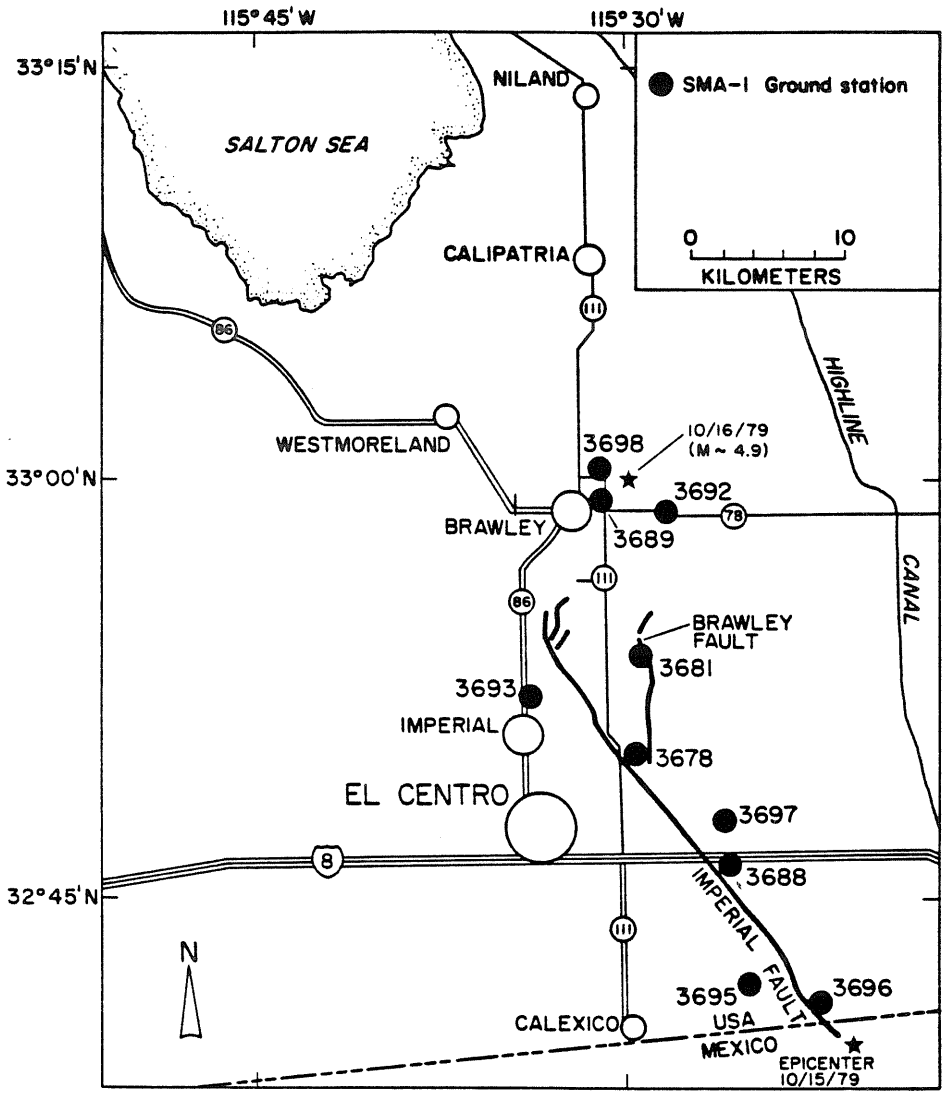

Figure 2-A-2 Map showing the temporary array stations and the epicenters. The epicenter of the aftershock at October 16, 23:16, 1979 (M_L =4.9) is located at less than 5 km to stations 3698, 3689 and 3692. The main shock epicenter is also shown in the lower right.

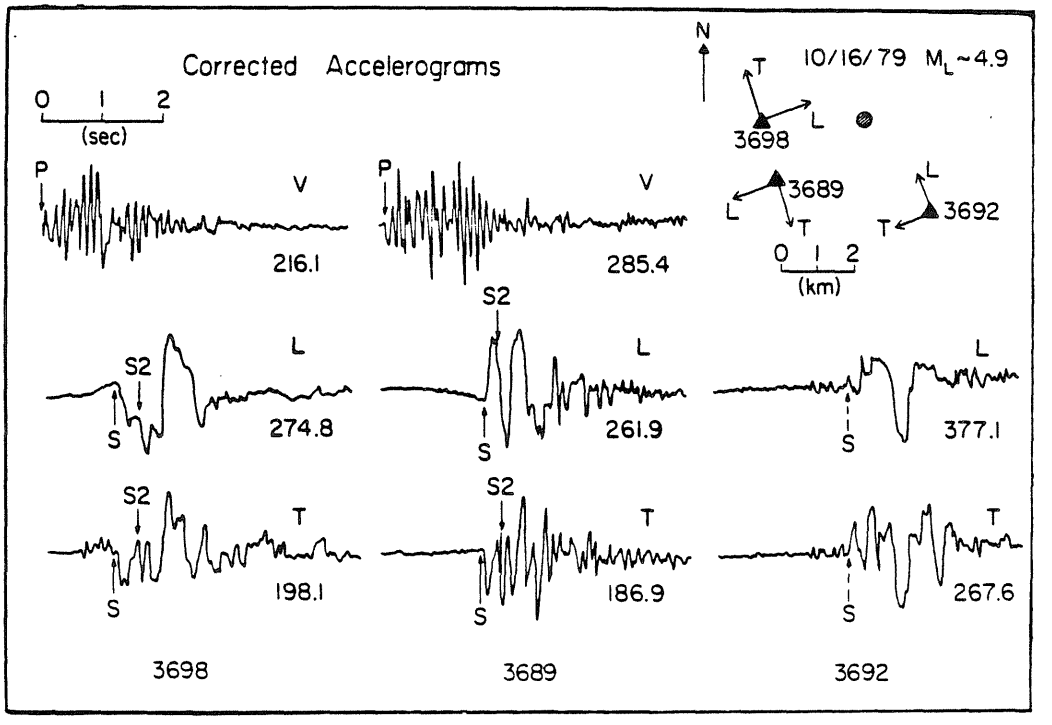

Figure 2-A-3 The corrected accelerograms at three closest stations 3698, 3689 and 3692 and the relative locations. L is the longitudinal component and T is the transverse component. V is the vertical component. The numbers are the magnitude of the accelerations in the unit of cm/sec^2.

Table 2-A-1 Station Information

Station	3698	3689	3692
Location	33.0095N 115.5207W	32.9914N 115.5167W	32.9816N 115.4743W
Distance (km)	3.0	4.2	5.1
ts-tp (sec)	1.3	1.7	2.2
Sensor(*) Orientation	L=81° T=351°	L=250° T=160°	L=338° T=248°
Peak Acc. (cm/sec^2)	L=274.8 T=198.1 V=216.1	L=261.9 T=186.9 V=285.4	L=377.1 T=267.6
Peak Vel. (cm/sec)	L=50.3 T=16.3 V=18.5	L=37.3 T=15.2 V=18.6	L=45.0 T=29.6
Peak Dis. (cm)	L=11.9 T=9.46 V=2.0	L=6.64 T=4.54 V=4.42	L=11.1 T=5.69

(*) The angle is measured from north clockwise direction. (L-Longitudinal, T-Transverse, V-Vertical)

Basin Structure and Synthetics

Earlier Imperial Valley strong motion studies involved mostly the tangential components or SH waves (e. g. Heaton and Helmberger, 1976). In these efforts, the Love wave development was produced by describing the basin structure in terms of a few layers. The synthetics for the many layered models with some travel time constraints yielded similar results and, thus, these layered models proved effective. The situation for the vertical and radial motions are more interesting as displayed in Figure 2-A-4. The radial and vertical accelerations are calculated for both a strike-slip and a dip-slip point shear dislocation situated at a depth of 2 km and recorded at a distance of 2 km. The generalized ray method is used to compute the structure response (Helmberger and Harkrider, 1978). It is easy to recognize all the phases corresponding to a single layer over a half-space velocity structure as indicated in the vertical component of the dip-slip source in Figure 2-A-4, where P_r and S_r are the reflected phases from the bottom of the basin and SP and PS are the conversion phases. When we model a multi-layered structure, a 4-layers over a half-space , these reflected and converted phases arrive at about the same time and become too small to be identified. Thus the direct ray is the essential contribution for this layered velocity structure at short epicentral ranges. In order to explain the polarization seen on vertical and horizontal components, the velocity gradient near the surface must be included. We approximate the P-velocity structure of Fuis et al. (1981) by a 21-layers over a half-space (see Figure 2-A-4). The Possion ratios are taken from the borehole data of Duke and Mal (1978) to construct the S-velocity structure. The velocities and densities for these layered structures are listed on Table 2-A-2.

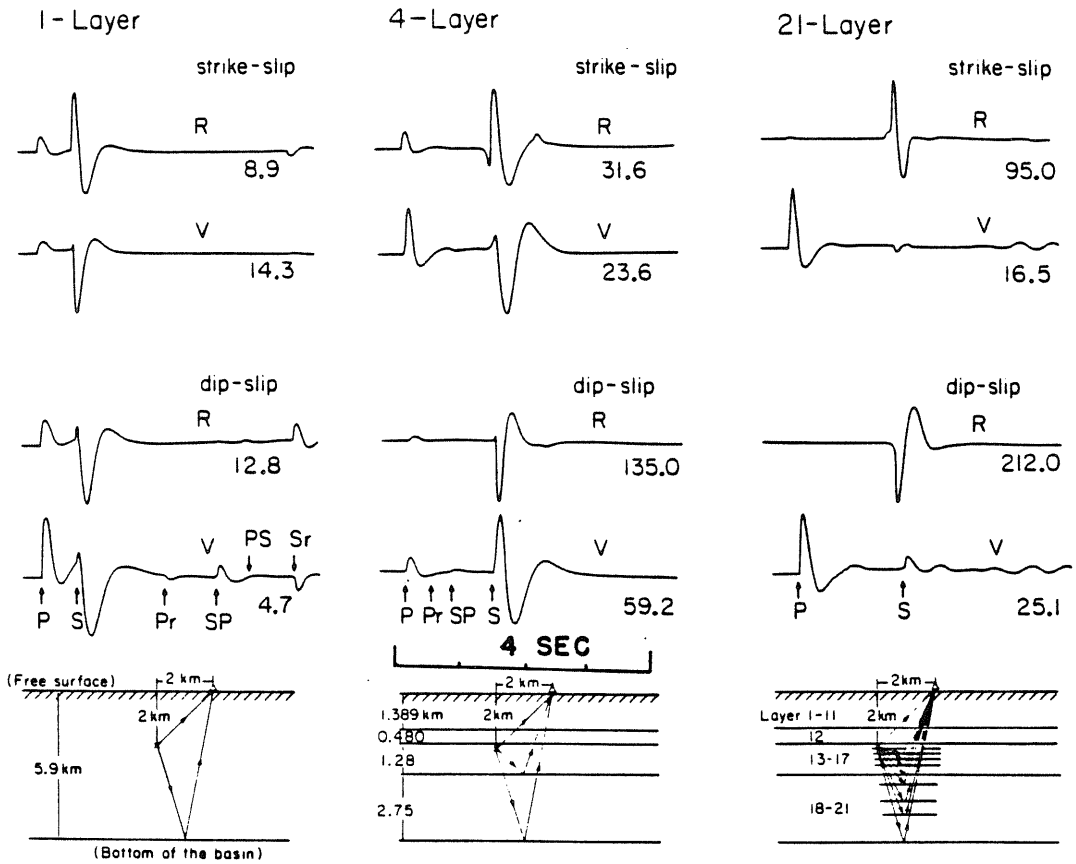

Figure 2-A-4 Synthetic accelerations for 3 different layered structures. All responses are calculated at 60° from the fault strike. Both the depth and the epicentral distances are 2 km. R is the radial component and V is the vertical component. The corresponding velocity and density functions are listed in Table 2-A-2.

Table 2-A-2 Velocity Structure

Layer No.	Thickness (km)	P-Velocity (km/sec)	S-velocity (km/sec)	Density (g/cm^3)
1-layer				
1	5.9	3.50	2.0	2.42
half-space		6.40	3.70	2.80
4-layer				
1	1.389	2.10	0.85	1.90
2	0.480	2.67	1.64	2.36
3	1.28	3.48	2.00	2.49
4	2.75	4.61	2.65	2.64
half-space		6.40	3.70	2.80
21-layer				
1	0.105	1.69	0.35	1.52
2	0.105	1.70	0.45	1.53
3	0.105	1.72	0.59	1.55
4	0.105	1.79	0.65	1.61
5	0.105	1.93	0.75	1.74
6	0.105	2.05	0.82	1.85
7	0.105	2.10	0.90	1.89
8	0.105	2.15	1.00	1.94
9	0.105	2.25	1.15	2.03
10	0.105	2.38	1.30	2.15
11	0.339	2.50	1.50	2.26
12	0.480	2.67	1.64	2.36
13	0.160	2.85	1.74	2.39
14	0.160	3.15	1.91	2.44
15	0.160	3.45	2.08	2.48
16	0.160	3.57	2.15	2.50
17	0.640	3.70	2.22	2.52
18	0.160	3.85	2.30	2.55
19	0.160	4.20	2.50	2.60
20	0.160	4.55	2.71	2.63
21	2.271	4.70	2.75	2.65
half-space	20.0	6.40	3.70	2.80

Two things are interesting to note. One is that the amplification factor in the layered media is quite remarkable as indicated by the amplitudes shown in Figure 2-A-4. All responses are based on a moment of 1.0×10^{23} dyne-cm. Another is the gradual change in the relative amplitude ratios between P and S waves. For the 21-layers over a half-space structure, the amplitude ratio of the radial to vertical component is about 5 in strike-slip source and about 10 in dip-slip case. This structure reproduces the proper phase separation between P and S waves onto vertical and horizontal components. Hence we use the 21-layers over a half-space structure to calculate response from a given source model.

Waveform Simulation

a. Point Source Model

The impulsive S waves provide a good opportunity to model the waveforms by using the point source assumption. The advantage of this approach is to obtain the over-all source parameters and depth efficiently. Combining this source mechanism and the 21-layers over a half space structure, we generate the synthetic body waves for the two horizontal components and for both acceleration and velocity. By trial and error, we find that the best point source solution has strike of N20° E, dip of 30° SE and slip angle of −80°, and a depth of 1.9 km. We adjusted these parameters on the basis of amplitude ratio between the longitudinal and transverse components at each station and the relative amplitude ratios between the three stations. The trade-off between the source parameters within certain limits is unavoidable. For the neighboring localities of .3 km from the epicenter can have more or less the same waveforms. Our preferred point source location is about 1.5 km south of the local routine location

(Johnson and Hutton, 1981). Our preferred point source location and velocity structure yield a good estimate of the S-P time at station 3692, but with .5 seconds time lag at station 3698 and .2 seconds at station 3689. In general, the point source model can predict the waveform reasonably well for stations 3698 and station 3692. In station 3689, there is a high frequency phase (marked as S2 in Figure 2-A-2) which appears at about .2 seconds after the S phase. S2 is a weaker arrival at site 3698 and can not be identified at site 3692. It is possible that a small asperity breaking close to site 3689 excites this phase, with little effect on the other two stations.

Waveform comparisons between the observed data and the point source synthetics for velocities and accelerations are shown in Figures 2-A-5 and 2-A-6, respectively. The source time function for the displacement is determined to be 1.0 second symmetric triangle. The average seismic moment estimated from velocity data in these three stations is 1.6×10^{23} dyne-cm. Table 2-A-3 summarizes the source parameters we determined in this point source model.

b. Line Source Model

The smooth velocity gradient on the structure we propose can only produce very faint multiples or scattered waves. Thus for an M_L=4.9 earthquake, the short duration signals (about 1.5 seconds), both P- and S-waves, are mainly the direct waves. The high-frequency P-wave trains suggest that the source must generate very high frequency waves and that the shear losses during propagation are responsible for the simple looking S waves. The high-frequency high-amplitude P waves are interpreted as the result of a series of small source ruptures due to a very rough dislocation process. In order to simplify the modeling

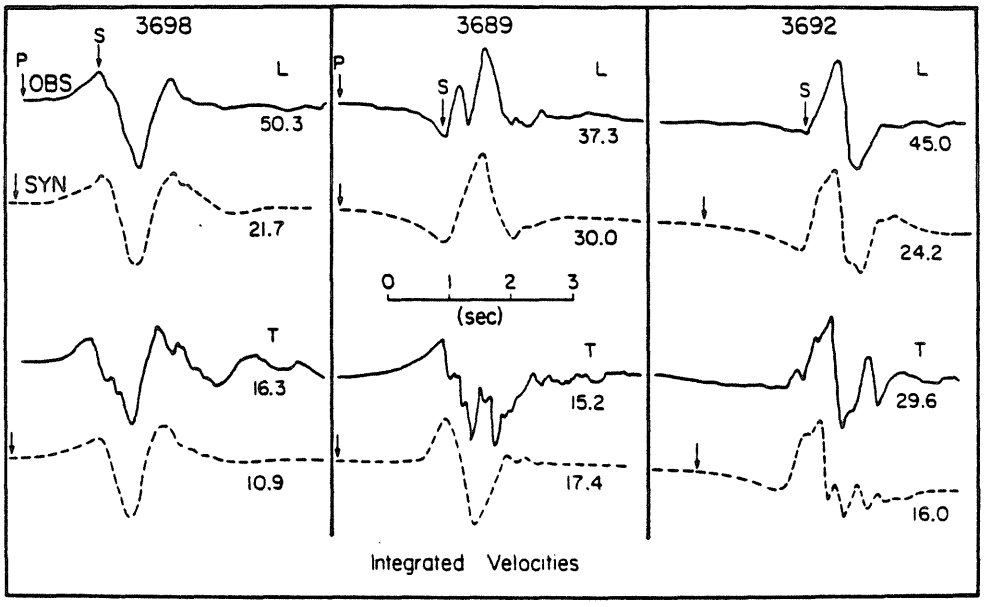

Figure 2-A-5 Comparisons between observed velocities vs. the point source synthetics at three closest stations. The solid traces are the observed data and dashed traces are the synthetics. The numbers are the velocities in cm/sec. The synthetics are calculated for a moment of 1.0×10^{28} dyne-cm. The source parameters for this point source model are listed in Table 2-A-3.

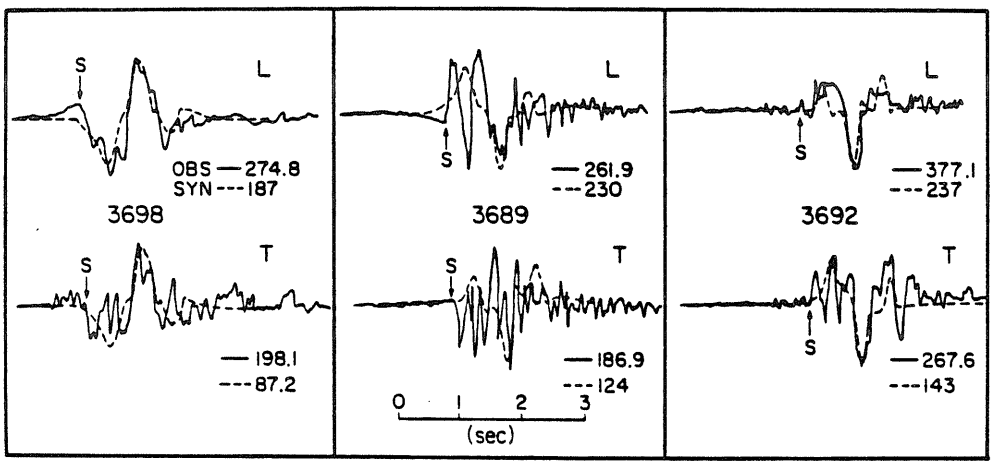

Figure 2-A-6 The synthetic accelerograms from the point source model.

Table 2-A-3 Source Parameters

Event Data	October 16, 23^h 16^m 31.62^s, 1979
Location	33.02N, 115.49W
Mechanism	Strike=N20° E Dip=30° SE Slip Angle=-80°
Depth	1.9km
Time Function	(0.5,0.5)-sec triangle
Seismic Moment	1.6×10^{23} dyne-cm

process, we simulate the P-waves by a line source model. Actually, the line source synthetics here are the superposition of point source responses along a line in the rupture direction with the proper time delays (Hartzell, 1978). Due to the lack of constraints on both rupture direction and the rupture velocity, we chose the simplest way to produce a high frequency seismogram. Judging from the frequency content in P waves, we use a line source of twenty-four point sources 2 km long and propagating down in the dip direction. The time delay is 0.05-second between the adjacent points, corresponding to a rupture velocity of about 0.9 shear velocity. A triangular source time function of (0.025-sec,0.025-sec) is convolved with the dislacement of each point source.

We chose to model station 3698 with our line source, since the accelerograms at site 3689 involved an additional small high frequency source, which is poorly constrained. Figure 2-A-7 shows the line source synthetics for three components at station 3698. The total moment used to compute these synthetics is 1.6×10^{23} dyne-cm, which is the moment determined by the point source model. Also we apply a triangular weighting function for these point sources such that the long-period nature of S-waves can be easily preserved. An extra triangular time function (0.025-sec, 0.025-sec) is convolved with the final synthetics to reduce the numerical noise due to the derivative. The amplitude of S waves on both horizontal components (as indicated in Figure 2-A-7) is about 6 times larger than that of P waves. However this is not seen in the observation, in which the vertical amplitude is comparable to the horizontals. Hence a physical mechanism which can attenuate the S waves and smooth the waveforms must be considered.

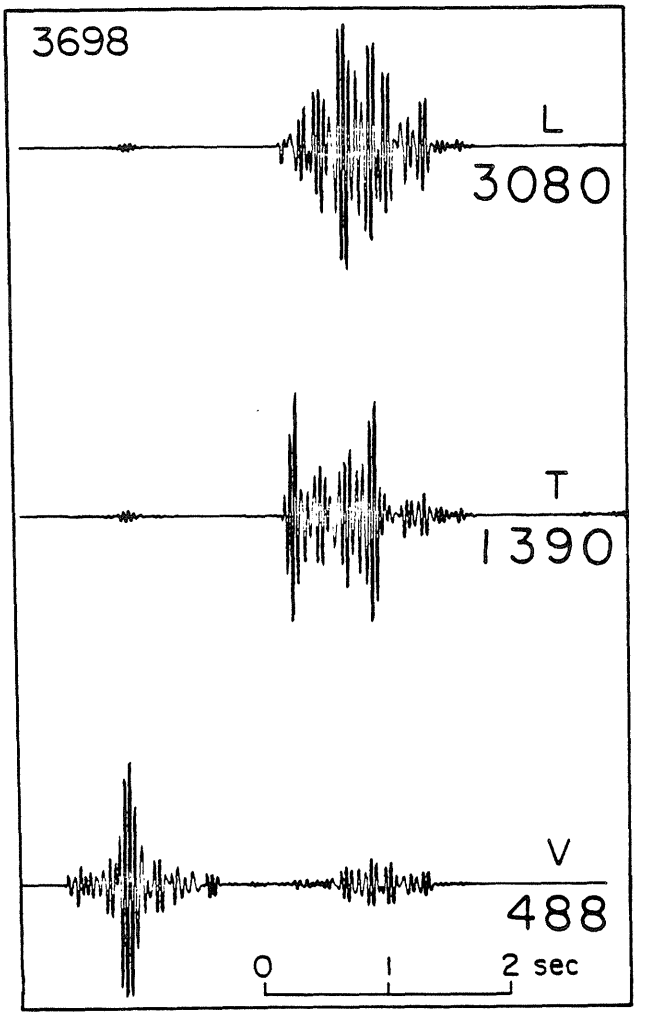

Figure 2-A-7 Line source synthetic accelerograms (in cm/sec^2) for three components at station 3698.

Attenuation

In a layered velocity structure, the wave amplitude is expected to be attenuated by both physical absorption and thin layer tunneling effects (Mellman and Helmberger, 1974). High velocity thin layers become barriers to the short wavelength signals, especially at distances further than the critical reflection ranges. For the same thin layer, the S waves will be more strongly attenuated by the tunneling effect than the P waves. Due to the lack of precise knowledge about the velocity structure, we will consider an effective Q model to account for the attenuation effects in the sediments. This basically includes absorption, tunneling and the possible scattering factors.

Helmberger et al. (1979) model the seismic pulses which have been multiply reflected between the ocean basin surface and the subbottom in the Bering Sea. They find very little evidence of attenuation at 10 Hz P waves. They suggest that a Q_α of 500 is the proper attenuation factor for about 1 km thick mature oceanic sediments in the Bering Sea. On the other hand, an analysis of seismograms from a downhole array in sediments near the San Francisco Bay area (Joyner, 1976) gives an estimation of Q_β of 10 to 15 down to a depth of about 200 meters. Other experimental data from earth dam studies also support this result with Q_β of about 10 to the depth of 72 m (Abdel-Ghaffar and Scott, 1978). We adopted the Q_α and Q_β from these previous studies and adjusted the value by our current velocity model. Table 2-A-4 lists the Q_α and Q_β for the structure in the current study. We estimate t^* assuming vertical incidence for the whole sedimentary column by using the simple relationship, $t^* = \int dt / Q_{av.}$ (along the ray path), where dt is the travel time and the $Q_{av.}$ is the average Q value at a specific layer. The predicted t^*_α is 0.0025 and t^*_β is 0.135 for our velocity structure. Thus the

Table 2-A-4 Attenuation in Sediments

Layer	Thickness (km)	Q_α	Q_β
1	0.105	211.8	6.2
2	0.105	211.8	8.8
3	0.105	211.8	15.3
4	0.105	1271.	132.2
5	0.105	1271.	163.7
6	0.105	1271.	197.5
7	0.105	1765.	341.5
8	0.105	1765.	412.3
9	0.105	1765.	512.4
10	0.105	1765.	598.2
11	0.339	1765.	737.9
12	0.480	1800.	798.6
13	0.160	1886.	832.8
14	0.160	1894.	833.7
15	0.160	1898.	834.3
16	0.160	1909.	835.3
17	0.640	1913.	837.2
18	0.160	1920.	839.8
19	0.160	1934.	842.2
20	0.160	1949.	855.0
21	2.271	1968.	865.9
22	20.0	2000.	891.3

(*) Effective $t^* = \int dt / Q_{av}$; $t^*_\alpha = 0.025, t^*_\beta = 0.135$.

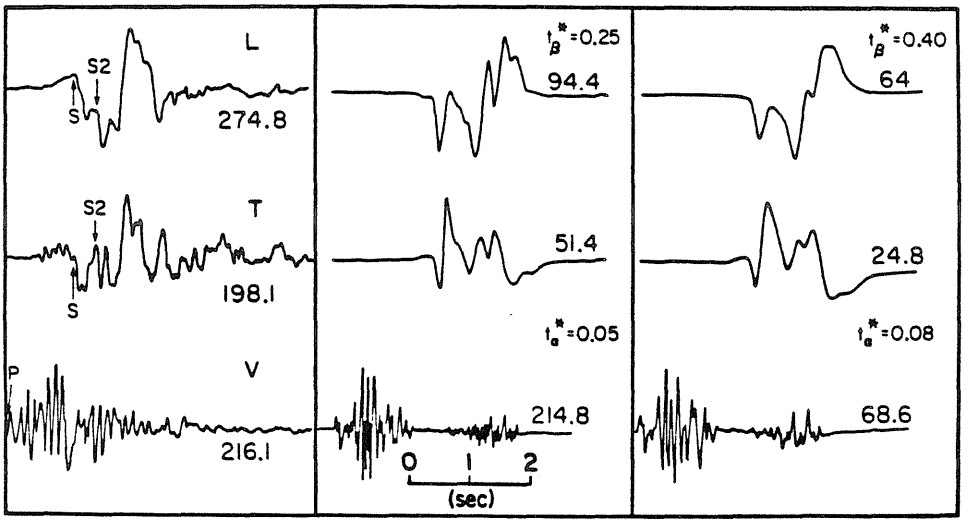

Figure 2-A-8 Comparisons of the observed accelerations vs. synthetics with different effective Q operators at station 3698. The left traces are the observed data.

synthetics for P and S waves can be corrected for attenuation by convolving the Futterman operator $F(t^*,t)$ (Carpenter, 1967).

The resulting line source synthetics including effective Q are shown in Figure 2-A-8. Different t^* values have been convolved with the synthetics in order to reduce the S-wave amplitude and smooth the waveform. We found that the effective t_α^* of .05 to .08 and t_β^* of .25 to .4 seem to be the reasonable attenuation value for P and S waves, which would model the observe amplitude ratio and frequency content.

Discussion and Conclusion

We present a self-consistent model to explain how the waves are generated and propagate at near-source distances. In order to generate the observed high-frequency P-waves, we postulate a rough rupturing source. It has been shown that an efficient way of generating high frequency waves is an abrupt change in the rupture velocity (Madariaga, 1977). It is possible that the varied physical property in the layered medium causes a non-uniform rupture. But we can not exclude the possibility of stress concentrations near the rupture front at this stage.

The vertical-horizontal frequency contrast in the strong ground motion accelerograms can be explained satisfactorily as a phenomenon associated with a layered basin structure. The velocity gradient in the layered medium causes the P and S phases to separate onto the vertical and horizontal components. Apparently, the shear wave amplification in a soft sedimentary medium can actually be cancelled by the effective shear loss along the wave path which produces a longer period S waves at near-source distances. The t_α^* of 0.05 to 0.08

and t_β^* of 0.25 to 0.4 seem to be the reasonable attenuation values of P and S waves in the sedimentary basin in this epicentral region. We expect this feature will vary to some extent in different basins or sedimentary regions depending on the velocity structure and the source depth.

2-B Modeling the Near-Source Ground Motion for the 23:19 M_L=5.0 Aftershock of the October 15, 1979 Imperial Valley Earthquake

Introduction

In recent years significant progress has been made in understanding longer period strong ground motions (displacements) produced by some of the larger California earthquakes. Assuming a distributed shear dislocation along planar surfaces embedded in a layered velocity structure provides an adequate set of parameters for modeling observations in a deterministic sense. Unfortunately, such models appear inadequate to explain the higher frequency signals (velocities or accelerations) which apparently are not consistent with the radiation patterns predicted from the longer period studies. What causes this breakdown of the deterministic approach at high frequencies is not clear. Crustal scattering (inappropriate Green's function), micro-source complexity (irregular dislocation elements) and perhaps macro-source complexity (interference of waves produced by various portions of the fault) are possible reasons. The latter cause of complexity can be largely eliminated by selecting a small event where the dislocation is confined to a localized region. We propose to study such an event and to address the first two possibilities, namely crustal scattering and irregular source elements. The event modeled in this study is an aftershock of the October 15, 1979 Imperial Valley earthquake, that was very well recorded by the Imperial Valley strong-motion array at all azimuths and at distances ranging from 8 km to 26 km. Furthermore, we have the rare opportunity to compare P-waveforms with S-waveforms which allows the estimation of differential attenuation coefficients within the sedimentary basin.

The 23:19 Aftershock

The October 15, 23:19 aftershock (M_L=5.0) occurred about two and a half minutes after the mainshock, and unfortunately most of the far-field data are overwhelmed by the coda of the main event. The only available information for this aftershock is from the strong-ground motion recordings. Using these data as well as some low-gain array data, Brady (1982) located the epicenter at 32° 46.00' N and 115° 26.48' W, which is on the Imperial Fault near Highway 8 and close to the zone of high energy release for the mainshock (Hartzell and Helmberger, 1982; Le Bras, 1982). The source depth is suggested to be about 9.5 km.

Figures 2-B-1(a) and 2-B-1(b) show the transverse and radial horizontal ground velocities from sixteen array stations. The impulsive waves are the S arrivals, which are the main signals on the horizontal component. The ground accelerations indicate similar impulsive S waves but contain more high-frequency complications. Most of the traces start at the P-arrival times, except for the six stations (AR6, AR8, AR9, DFF, HOT and BOC) which were not retriggered by this aftershock. Due to the rather small P wave amplitude on the horizontal component, we can only identify the P-waves by the timing comparison between horizontal and vertical traces. The predominant strike-slip mechanism and the slow velocity structure near the surface produce negligible P waves on the horizontal components, a very common feature observed in most of the Imperial Valley accelerograms (Chapter 2-A, this thesis).

At most stations, the direction of the S wave particle motion is consistent with right-lateral strike-slip motion, with the strike nearly parallel to the Imperial Fault, N40°W. The fault plane solution (strike=N40°W, dip=90° and rake= 180°) satisfies most of the S-wave motions except those near the S wave

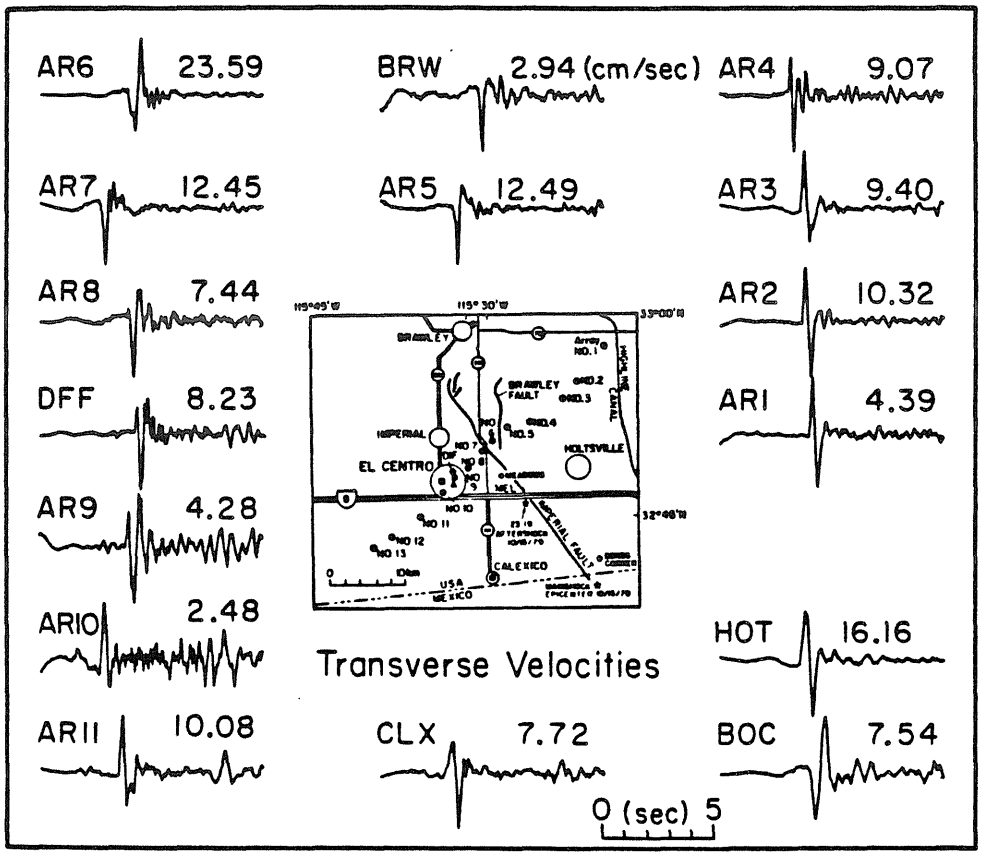

Figure 2-B-1(a) The transverse components of ground velocities from the 23:19, October 15, 1979 Imperial Valley aftershock.

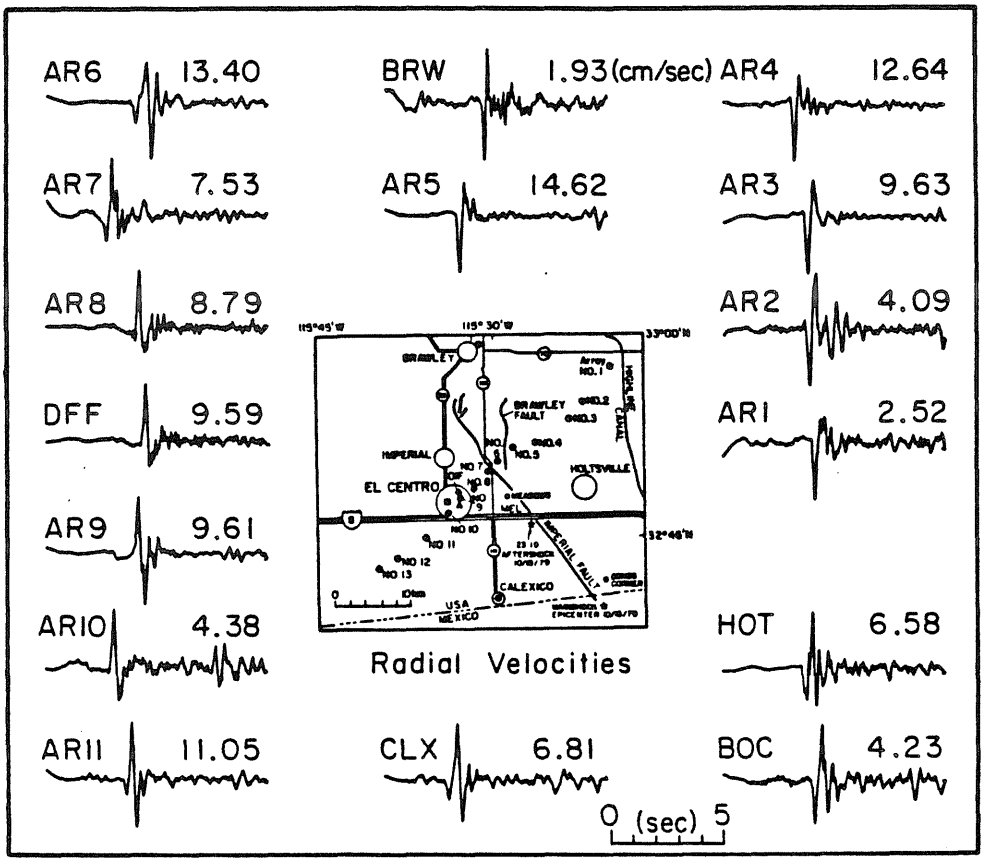

Figure 2-B-1(b) The radial components of ground velocities from the 23:19, October 15, 1979 Imperial Valley aftershock.

nodal directions.

There is an indication of directivity observed on the variation of signal durations at different azimuths (see Figure 2-B-1(a) or 2-B-1(b)). We can roughly estimate the fault length by using difference in time duration of S waves between station AR5 (.25 secs) and station BOC (.5 secs), which are located NW and SE along the strike direction, respectively. Assuming a rupture velocity of 3 km/sec towards the north, the fault length is estimated to be about 1.1 km.

The ground motions on vertical components are much smaller in amplitude and more incoherent in waveform. Only six stations (AR6, AR8, AR9, DFF, HOT and BOC) show complete P arrivals on the velocity traces, because only these six stations continued recording after the triggering for the main event. These vertical ground motions are valuable in quantifying the difference between P- and S-waves propagating within a sedimentary basin.

Forward Modeling

Forward modeling of the horizontal velocities is presented. Synthetics for a point source solution with a pure strike-slip mechanism are presented first to illustrate the general nature of the observed ground motions. The disagreement between the data and this single point source solution leads us to consider a complex source hypothesis; a solution obtained by trial and error from these considerations will be described in this section.

Velocity Structure. The velocity structure used to calculate the Green's function is listed on Table 2-B-1, which is modified from the structure described in Chapter 2-A (this thesis). The generalized ray method (Helmberger and Harkrider, 1978) is used to calculate the response. The time interval used in

Table 2-B-1 Velocity Structure

	Th(km)	α(km/sec)	β(km/sec)	ρ(g/cm^3)
1	0.105	1.69	0.35	1.52
2	0.105	1.70	0.40	1.53
3	0.105	1.72	0.50	1.56
4	0.105	1.79	0.60	1.61
5	0.105	1.93	0.70	1.74
6	0.105	2.05	0.80	1.85
7	0.105	2.10	0.90	1.89
8	0.105	2.15	1.00	1.94
9	0.105	2.25	1.15	2.03
10	0.105	2.38	1.30	2.15
11	0.339	2.50	1.50	2.26
12	0.480	2.67	1.64	2.36
13	0.160	2.85	1.74	2.39
14	0.160	3.15	1.91	2.44
15	0.160	3.45	2.08	2.48
16	0.160	3.57	2.15	2.50
17	0.640	3.70	2.22	2.52
18	0.160	3.85	2.30	2.55
19	0.160	4.20	2.50	2.60
20	0.160	4.55	2.71	2.63
21	2.271	4.70	2.75	2.65
22	5.0	5.50	3.40	2.75
23	10.0	7.20	4.10	2.80

computing is 0.005 seconds. Because the source depth is large relative to the distance from epicenter to station, we include only direct rays of P, SH and SV waves in the calculation. Table 2-B-2 lists the epicentral distances for all the recording sites and the observed and the calculated P and S-P times. Except for station AR10, the velocity model produces good agreement between the observed and calculated P and S-P times for most of the stations within 15 km of the epicenter. The short S-P time and small amplitude observed at station AR10 suggest that there exists some local high velocity structure which reduces the S travel time. Station AR6 and station AR7 have about 0.55 seconds S-P time difference, yet are only .3 km different in epicentral range. This indicates that the local structure near stations AR6 and AR7 is more complicated than the layered medium used in the calculation. The complex waveforms recorded at station AR6 also suggest that the rays probably experienced some multi-pathing as suggested by Rial and Scott (1983). At more distant stations, AR1, AR2 and BRW, the observed S-P times are shorter than the calculated. This is in agreement with the suggestion by Fuis et al. (1980) that sediments are thinning towards these stations.

One-Source Model. Synthetic velocity traces for a single vertical strike-slip point source model (N40° W) and the observed data are shown in Figure 2-B-2(a) and 2-B-2(b) for the transverse and radial components, respectively. A triangular time function (0.1-sec, 0.1-sec) is used to represent the far-field source time function. The numbers indicate amplitude ratios of the data to the synthetics for a seismic moment of 1.0×10^{24} dyne-cm. The waveforms agree reasonably well between the data and the synthetics, although the amplitudes are not well matched, especially at stations near the theoretical nodes.

Table 2-B-2 Epicentral Distances and Travel Times

Station	Distance (km)	Obs-P (sec)	Th-P (sec)	Obs S-P (sec)	Th S-P (sec)
AR1	24.3	5.78	5.872	4.0	4.466
AR2	18.3	4.88	4.809	3.65	3.855
AR3	14.8	4.28	4.203	3.5	3.475
AR4	10.4	3.50	3.478	3.05	3.016
AR5	10.7	3.48	3.525	3.0	3.046
AR6	9.2	3.38	3.294	3.1	2.897
AR7	8.9			2.55	2.868
AR8	9.6			2.8	2.936
AR9	10.5			2.9	3.025
AR10	12.1			2.7	3.189
AR11	14.1			3.5	3.401
DFF	10.0			2.8	2.975
HOT	7.5			2.8	2.739
CLX	11.6	4.09	3.669	3.0	3.138
BOC	12.7	3.88	3.862	3.2	3.259
BRW	25.6	5.84	6.105	4.3	4.659

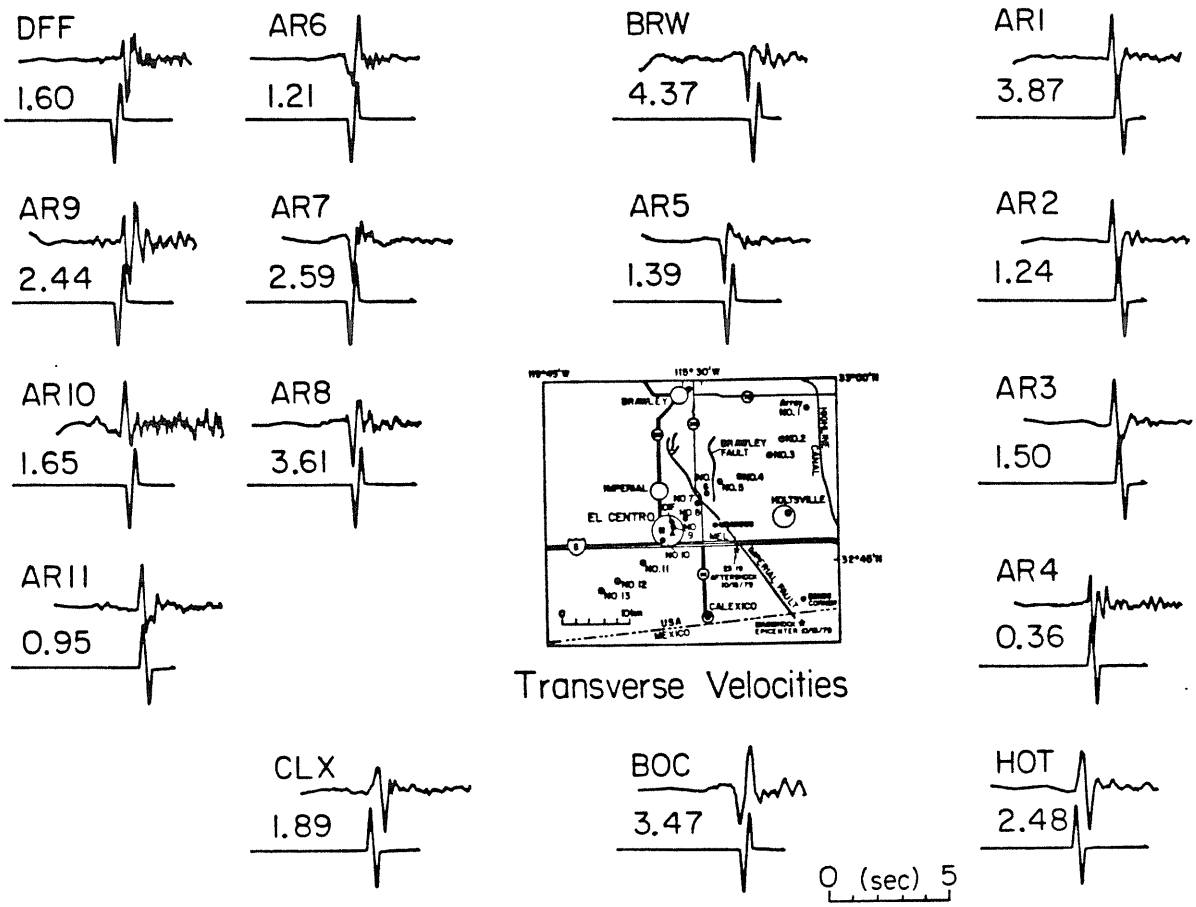

Figure 2-B-2(a) Waveform comparisons of the transverse ground velocities vs. synthetics. The synthetic velocities are computed from a pure right-lateral strike-slip point source along N40°W. The total moment is 1.0×10^{24} dyne-cm. A triangular source time function of (.1-sec, .1-sec) was used in this calculation. The numbers are the amplitude ratios of the data vs. the synthetics.

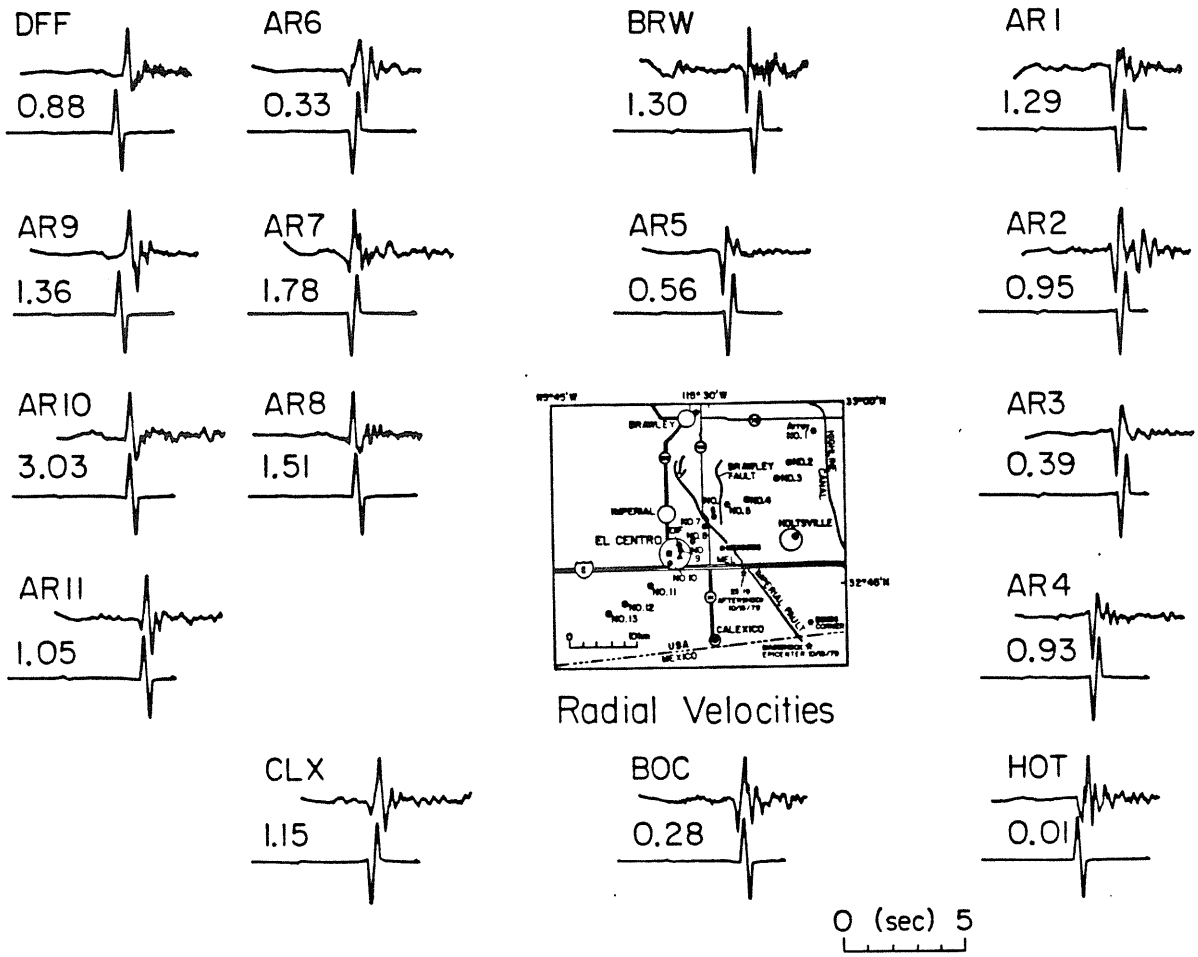

Figure 2-B-2(b) Waveform comparisons of the radial ground velocities vs. synthetics. The source mechanism is the same as that in Figure 2-B-2(a).

Figure 2-B-3 illustrates an example of ground motions near an SH node. By examining the horizontal displacement traces at stations AR3, AR4 and AR5, the polarity reversal in the transverse components suggests that the SH node for this aftershock passes somewhere between array station AR4 and AR5, but closer to AR4. However, in terms of amplitude, it is difficult to recognize that station AR4 is near an SH node, especially if accelerations are considered. In station AR4, the amplitude ratio of the transverse to the radial component is 0.7 in displacement and about 1.2 in acceleration. Thus a single source model which has clear nodes can reasonably explain the longer-period ground motions but fails to account for the high-frequency waves. Similar features can be observed at most of the other near-node stations, such as the transverse components of DFF and AR9 and the radial components of BOC, HOT, AR6 and AR7. For wavelengths less than the fault size of this aftershock (about 1 km), we might expect to see a more complex rupture mechanism, which can perhaps smear out the nodes. This corresponds to a period of about .3 seconds, thus for wave periods less than 0.3 seconds the effects of source irregularities are expected to become important.

Two-Source Model. We simulate a non-smooth rupture process by superposing two point sources rupturing one after the other with a given time delay. The effect of such a complex source on the radiation pattern is described next.

Through a trial and error test, we found that an extra point source with a different fault geometry can be added to improve the amplitude ratio at near nodal stations. In Figure 2-B-4, we show the waveform comparisons for horizontal velocities at station AR4 from both single point source solution (strike=N320° E, dip=90°, slip= 180° and M_o=1.0×10^{24} dyne-cm) and complex

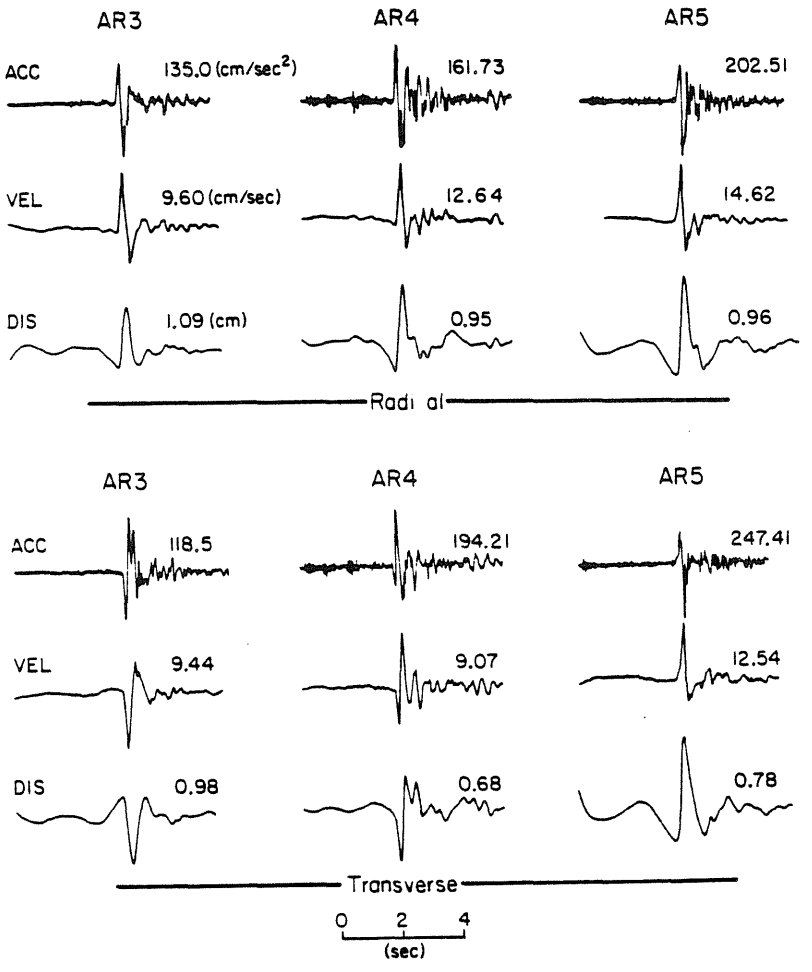

Figure 2-B-3 The horizontal accelerations, velocities and displacements at array stations No.3, No.4 and No.5. The SH node is near station No.4.

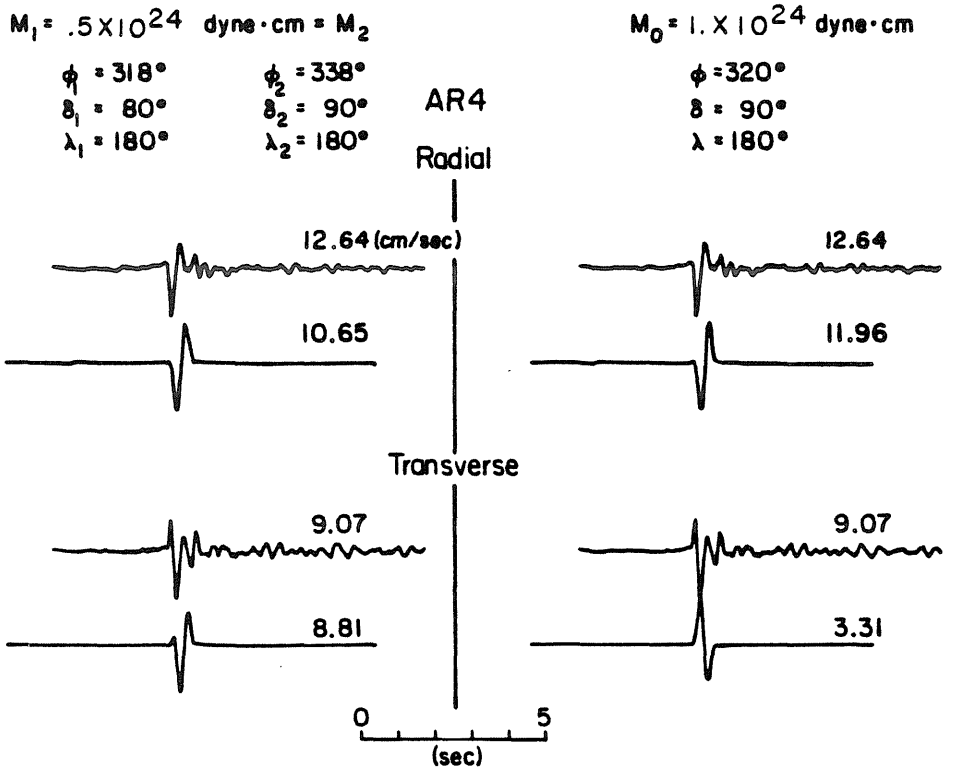

Figure 2-B-4 Comparisons of data vs synthetics for station AR4. On the right column, the synthetics are computed from a single point source model, which can account for about 30% of the amplitude on the transverse component. The left column shows the synthetics computed for complex two-source solution, which can produce amplitudes comparable to the observations in both components.

two-point source solution (first source : strike=N318°E, dip=80°NE, slip=180° and moment=.5×10^{24} dyne-cm ; second source: strike=N338°E, dip=90°, slip=180° and moment=.5×10^{24} dyne-cm; time delay between the sources = .1 seconds). As indicated in Figure 2-B-4, a variation in the source orientation along the rupture plane can easily smear out the node and may better explain amplitude ratio between the two components. However, this approach will increase the source parameters rapidly and the forward modeling method becomes too cumbersome to manage. In order to find a multi-source mechanism appropriate for all stations, we introduce an amplitude inversion scheme which allows the source orientation to vary freely and give an optimal solution by minimizing the integrated amplitude difference between the data and the synthetics.

Inversion Method

In order to include the amplitude information in the inversion procedure, we define an error function e_i for each seismogram i, as

$$e_i = \int_0^T \left[f_i(t) - g_i(t) \right]^2 dt,$$

where $f_i(t)$ represents the observed data trace, $g_i(t)$ is the synthetic seismogram generated from starting model parameters, and T is the time segment used in the inversion procedure.

Similar to the waveform inversion method used by Le Bras (1982), Wallace et al. (1981) and Mellman (1978), the optimal solution is obtained through an iterative least-squares scheme which minimizes the sum of the squares of the

error functions. The source parameters include the seismic moment, strike direction, rake and dip for each source element. The model variation , φ, can easily be obtained from A, the matrix of partials constructed from the derivatives of the error function with respect to the model parameters, and the error function, e, by applying the following relationship:

$$\varphi = (A^T A)^{-1} A^T e,$$

where -1 represents the inverse and the superscript T denotes the transpose.

Using the displacement expressions in cylindrical coordinates, (Helmberger and Harkrider, 1978) the error function can easily be calculated by the linear sum of the auto- and cross- correlations of the data and the Green's functions with coefficients dependent on source orientations (see Appendix I for detailed mathematical derivation). For each iterative inversion step, we need to evaluate the error function and partials, but the correlation functions need to be estimated only once.

Figure 2-B-5 shows an example of the inversion procedure. The synthetic data consist of two point sources; the first one has strike=N318° E, dip=80° NE and rake=180° and the second source has strike=N338° E, dip=90° and rake= 180°. Both sources have the same seismic moments. A time delay between these two sources is assigned for each data trace. The data are weighted so that all the observed peak amplitudes are normalized to unity. This can reduce the unknown amplification effects which are commonly observed in the near-field data. A damping coefficient of 0.05 is used to stabilize the inversion procedure. The initial model (N=0) shown in Figure 2-B-5 assumes two sources with the same fault orientations: strike=N300° E, dip=60NE and rake=150°. The initial

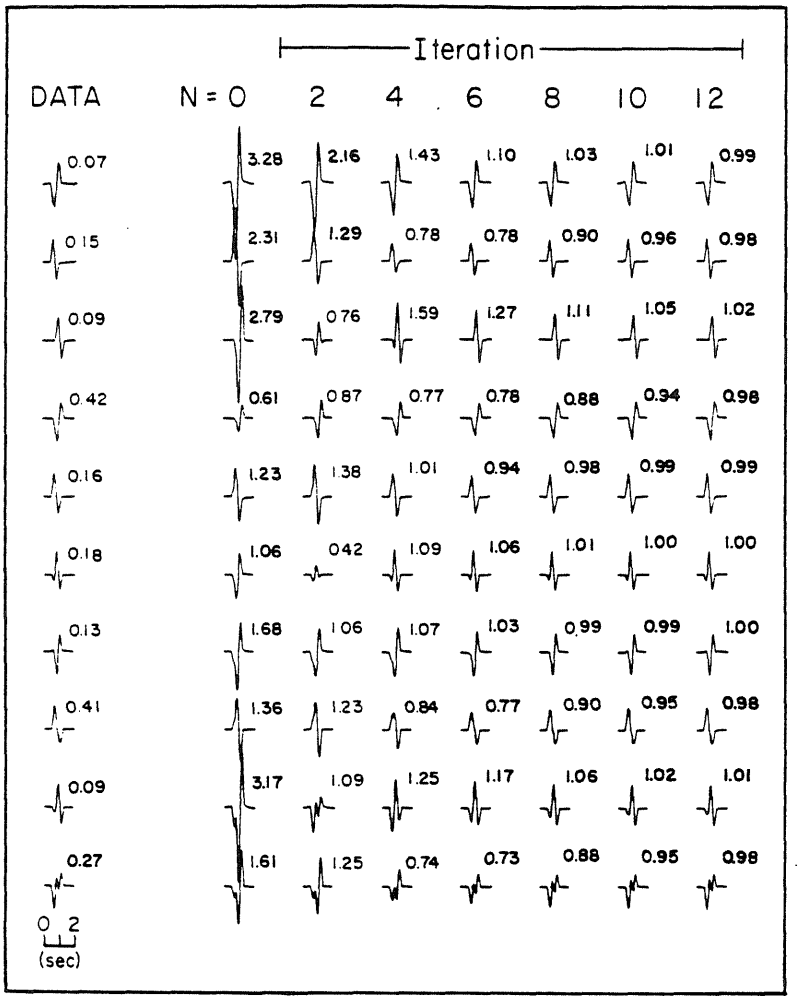

Figure 2-B-5 The amplitude inversion procedure. The data consist of two equal seismic moment sources. The absolute amplitudes for the synthetic data are also indicated. By using the damping coefficient of .05, we can reach reasonable solution after 8 iterations. The number associated with each seismogram in iteration procedure is the amplitude ratio of the synthetic to the data.

seismic moment for the second source is 4 times larger than the first source. The parameters which are allowed to vary in the inversion procedure are strike, dip, rake and seismic moment for each source element. As illustrated in Figure 2-B-5, after 8 iterations, a solution is found that matches the data very well.

Application to Modeling the Ground Velocities

We apply the inversion method to the ground velocities recorded during the 23:19 aftershock. The data from AR1, AR2, BRW and AR6 are not included in the calculation because we cannot adequately model the velocity structure. The remaining data seismograms are each weighted by the inverse of the peak amplitude on that component to increase the sensitivity of the inversion process to the waveform observed at low amplitude seismograms. In order to avoid extra noise, we use a 2-second time segment for auto- and cross- correlations in the inversion. Furthermore, we use observed S wave travel times to align the data and the synthetics to reduce the possible error introduced by travel time difference.

We constrain the model by assuming the source consists of two point sources. A 0.2 seconds symmetric triangular time function is convolved with the step response to approximate the dislocation time history for each point source. A time delay between point sources is assigned for each station from the best trial and error result (Table 2-B-3).

The starting model in the inversion is our best trial and error solution, which contains two sources (source 1: strike=N318°E, dip =80° NE, rake=180°, and source 2: strike=N338°E, dip=90°, rake =180°) and with equal seismic moments. In the solution obtained from the inversion procedure, the first

Table 2-B-3 Time Delays

	Delays (sec)
AR1	0.1
AR2	0.1
AR3	0.1
AR4	0.1
AR5	0.05
AR6	0.1
AR7	0.1
AR8	0.1
AR9	0.1
AR10	0.1
AR11	0.1
DFF	0.1
HOT	0.2
CLX	0.2
BOC	0.2
BRW	0.05

source has strike=N319°E, dip=42°NE, rake=165° and a moment of 0.7×10^{24} dyne-cm; the second source, about 1 km to the north, has strike=N324°E, dip=82°SW and rake= 181°, and a moment of 1.4×10^{24} dyne-cm. Comparisons of observed velocities and synthetic velocities obtained from this inversion method are shown in Figure 2-B-6-(a) and 2-B-6-(b) for the transverse and the radial components, respectively. The numbers are the amplitude ratios of the observed to the synthetic seismograms. We also show comparisons of observed data vs. synthetics for stations AR1, AR2, BRW and AR6, which were not used in the inversion procedure. Since we normalize the data to unit peak amplitude, high amplitude data do not dominate the inversion solution, and the waveform of small amplitude data is well restored.

We also show comparisons of six vertical velocities vs. synthetics from this inversion solution in Figure 2-B-7. For stations AR8, AR9, and DFF, which are near the maximum of P or SV waves, the synthetics match the data reasonably well between waveform and amplitude.

Ground Acceleration and Attenuation

We use the inversion solution obtained from velocity data to generate synthetic accelerograms for the 16 recording sites. Comparisons of data and synthetics are shown in Figure 2-B-8(a) and 2-B-8(b) for the transverse and radial components, respectively. The amplitude ratios of data vs. synthetics are also indicated. An extra triangular function (0.05-sec, 0.05-sec) is convolved with the seismograms to reduce the noise due to the time derivative. Although there is more high-frequency complexity in the data, the synthetic waveforms generally match the initial 1-second of the data quite well.

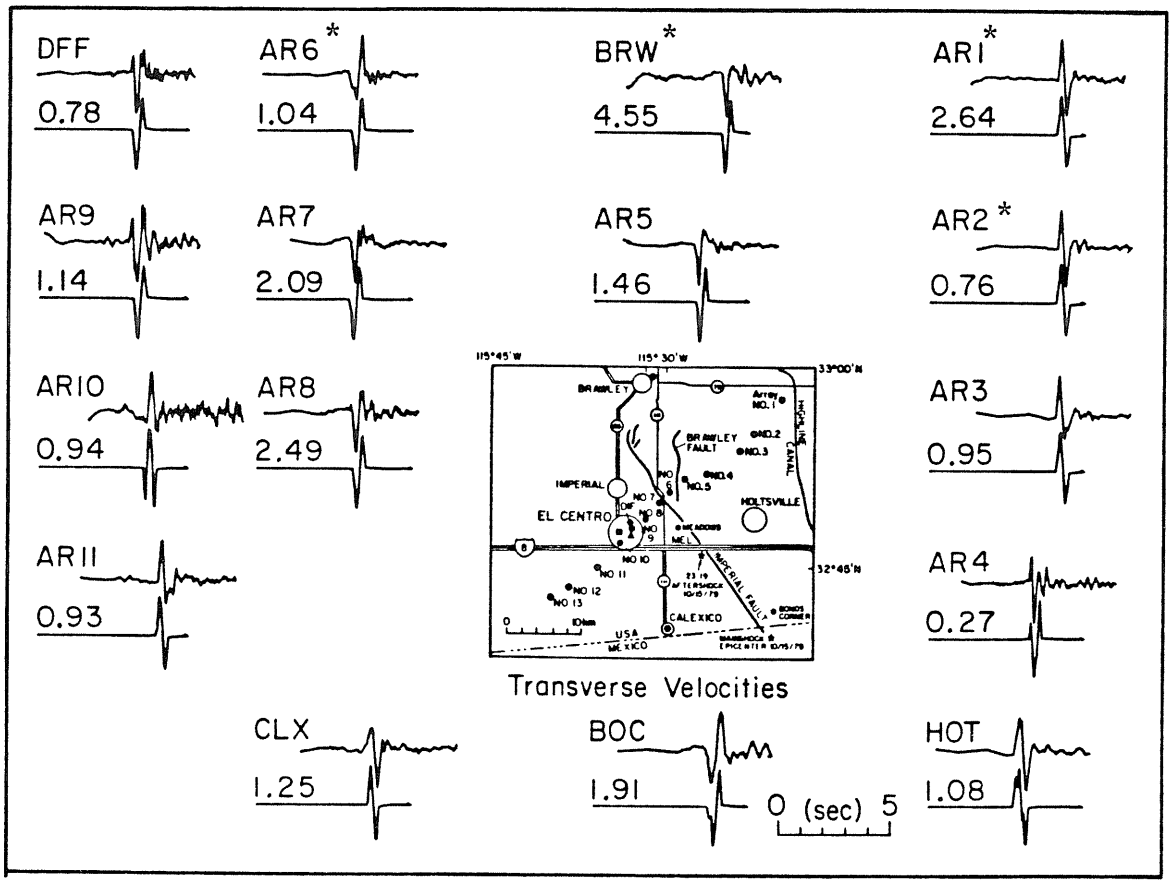

Figure 2-B-6(a) Comparisons of the synthetics from inversion method vs. the data for the transverse ground velocities. The numbers are amplitude ratios of the data to the synthetics. The inversion solution consists two sources: the first source has a seismic moment of 0.7×10^{24} dyne-cm and has strike=N319° E, dip=42° NE and rake=165°; the second source has twice of the first seismic moment and has strike=N324° E, dip=82° SW and rake=181°. * indicates station not used in inversion.

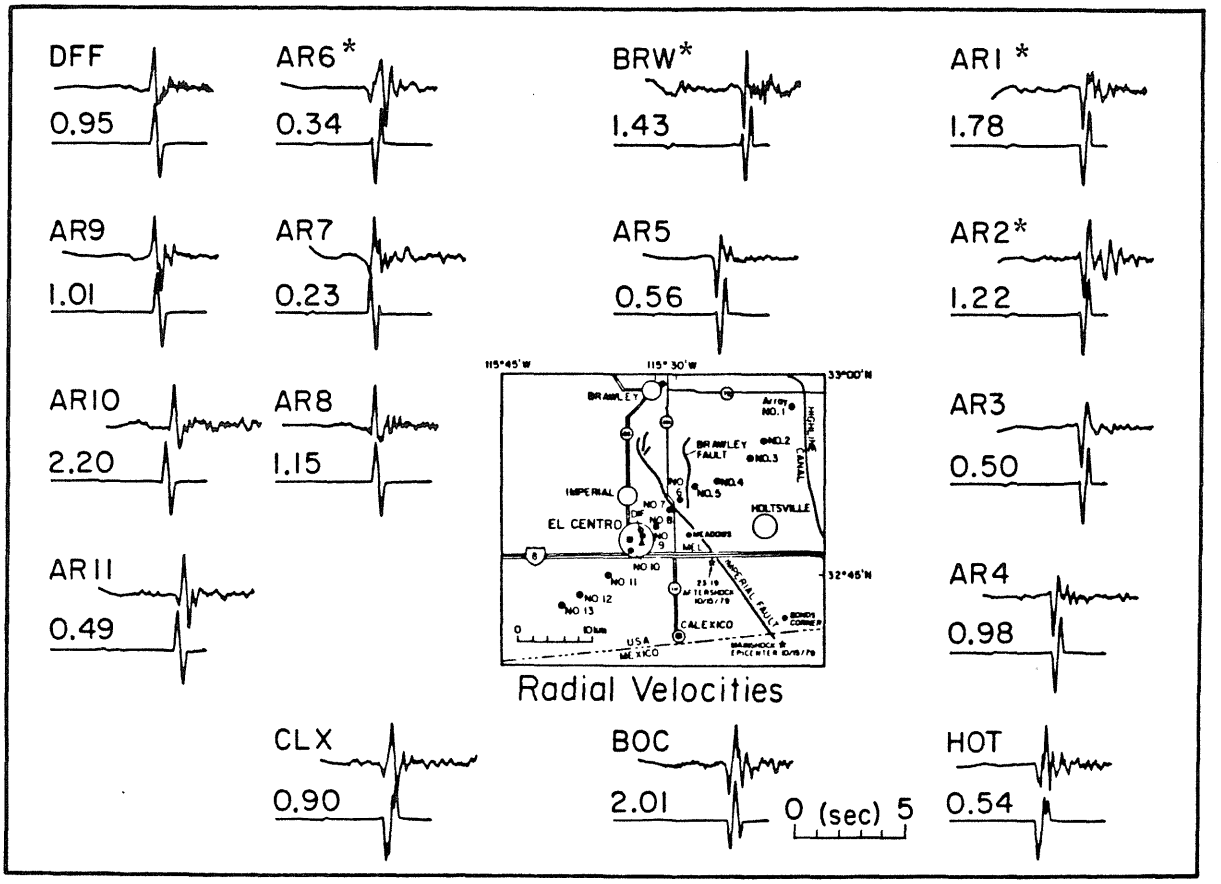

Figure 2-B-6(b) Comparisons of the synthetics from inversion result vs. the data for the radial ground velocities.

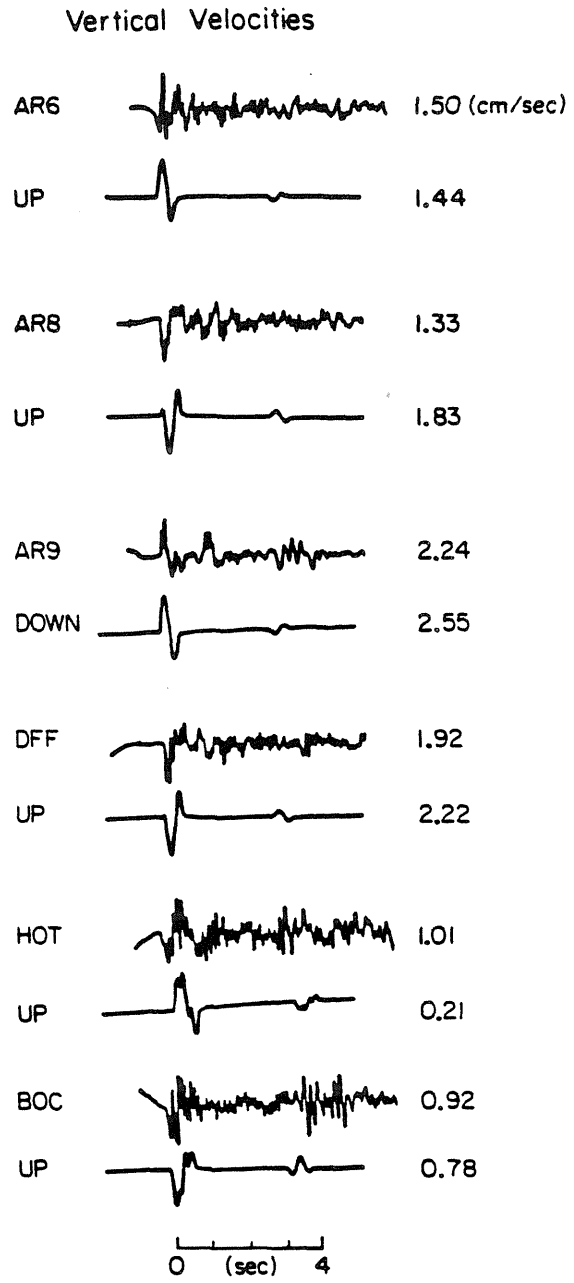

Figure 2-B-7 Comparisons of vertical velocities vs. synthetics. The synthetic seismograms are computed from the inversion solution derived from horizontal velocities.

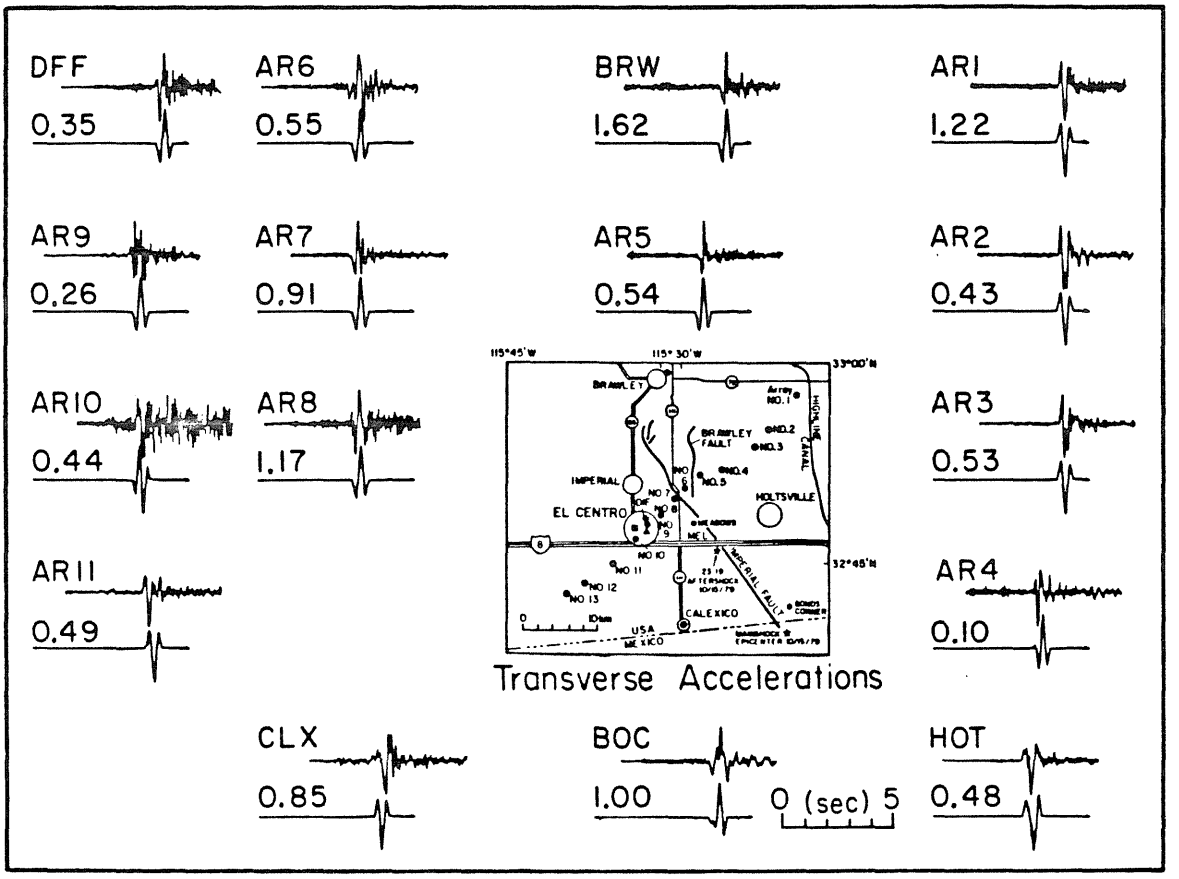

Figure 2-B-8(a) Comparisons of the transverse ground accelerations vs. the synthetics. The synthetic seismograms are computed from the inversion solution derived from velocities. The numbers are amplitude ratios of the data to the synthetics.

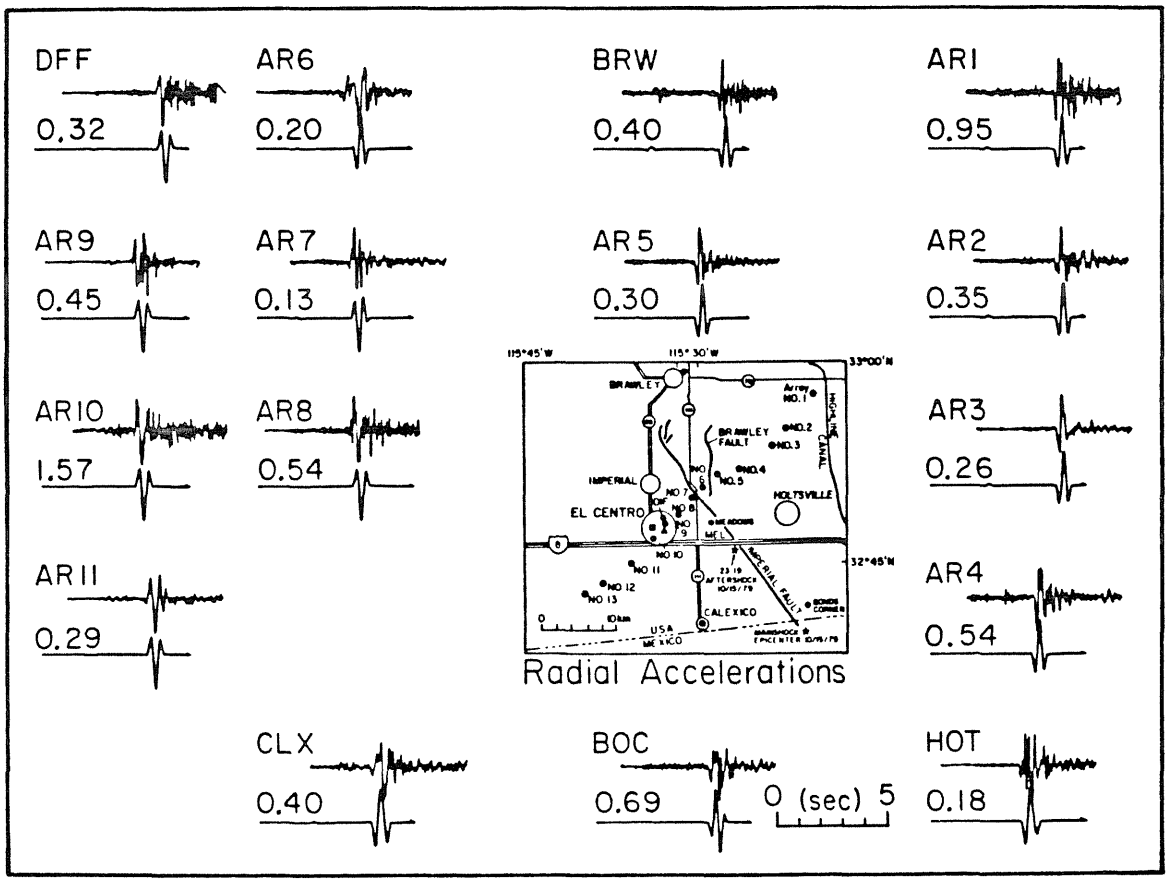

Figure 2-B-8(b) Comparisons of the radial ground accelerations vs. the synthetics.

We note that stations AR8, AR9, AR10 and DFF contain high frequency arrivals after the S-arrivals. These waves are too high frequency to become phases in velocity or displacement due to filtering implied by the integration. It is suggested that the local structure near these stations is the most probable cause of high-frequency waves. The radial components seem to have more complications than the transverse components, as seen in stations BOC, HOT, AR7 and AR6.

The vertical accelerations are rich in high-frequency waves. This is commonly observed in recordings of event in the Imperial Valley. As shown in Figure 2-B-9, the comparison of ground motions on the radial and vertical components of station AR8 indicates that the vertical acceleration is anomalous in both waveform (i.e. the frequency content) and amplitude. We have presented a solution derived from inverting horizontal ground velocities that can match the vertical velocity of station AR8 quite well (see Figure 2-B-7). This suggests that the longer period nature of the source seen from both P and S waves is the same. This also leads to speculation that high shear attenuation associated with the sediments has filtered the high frequency waves from the horizontal components. A similar conclusion was drawn from the high-amplitude, high-frequency vertical waves observed in October 16, 23:16 Imperial Valley aftershock (Chapter 2-A, this thesis).

In this aftershock (23:19, October 15), the amplitude ratio of vertical to the horizontal acceleration is at least 5 times larger than the vertical to horizontal velocity ratios. We suggest that the difference in P and S waves seen in accelerations is due to the different attenuation coefficients for these two types of waves. As illustrated in Figure 2-B-10, we test the attenuation effects by

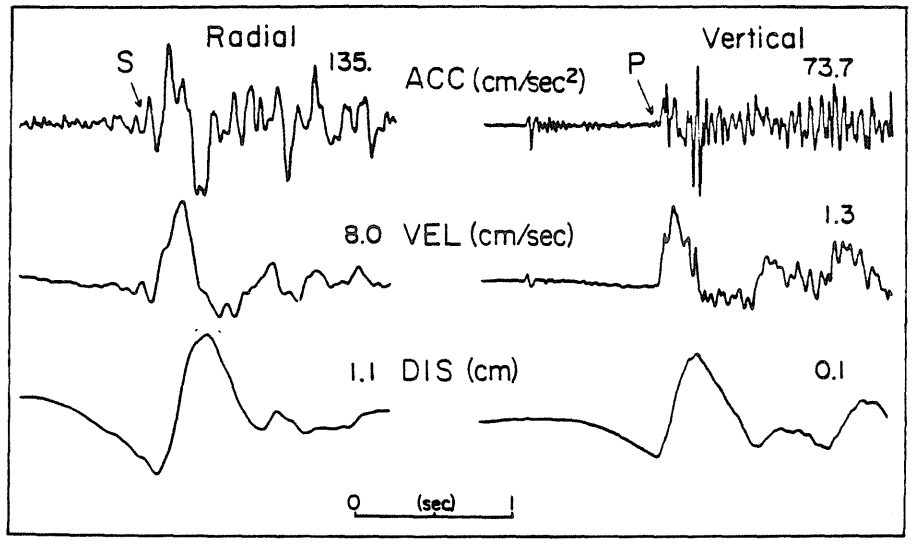

Figure 2-B-9 The radial and vertical ground motions recorded at station AR8.

convolving different Futterman Q operators on vertical accelerograms for the six available stations, AR6, AR8, AR9, DFF, HOT and BOC. It is suggested that the t_α^* should not be larger than 0.001, which would maintain the observed P waveforms. For t_β^* of 0.08 to 0.10, we can obtain reasonable amplitude and frequency content comparable to the observed S waves. These t^*s are close to the theoretical estimate from the layered medium used in Chapter 2-A (Table 2-A-4). The t_β^* derived from this aftershock study is lower than that in Brawley aftershock (Chapter 2-A, this thesis), from which a t_β^* of .25 to .4 is obtained. The significant difference between these two aftershocks is the source depth. We speculate that a source situated in a sedimentary basin, such as the Brawley aftershock, can generate anomalous high-frequency waves due to the rupturing through layered but not well compacted media. The severe shear loss in near-field associated with such a shallow event is perhaps partly due to the non-linear response of soft material to the source dislocation.

Ground Acceleration in the Mainshock

We recognize from near source seismograms that for longer faulting, such as the 1966 Parkfield earthquake or the 1979 Imperial Valley earthquake, that the phases corresponding to the peak accelerations have little association, in both time and space, with the peak ground displacements. An example of this is shown in Figure 2-B-11, which illustrates the ground acceleration, velocity and displacement recorded at station AR5 (230° component) from the mainshock. The peak acceleration phase corresponds more to the initiation of over-all ground motion, and this can be seen on the waveform correlation. Thus, the high ground accelerations generated from larger earthquake may result from a

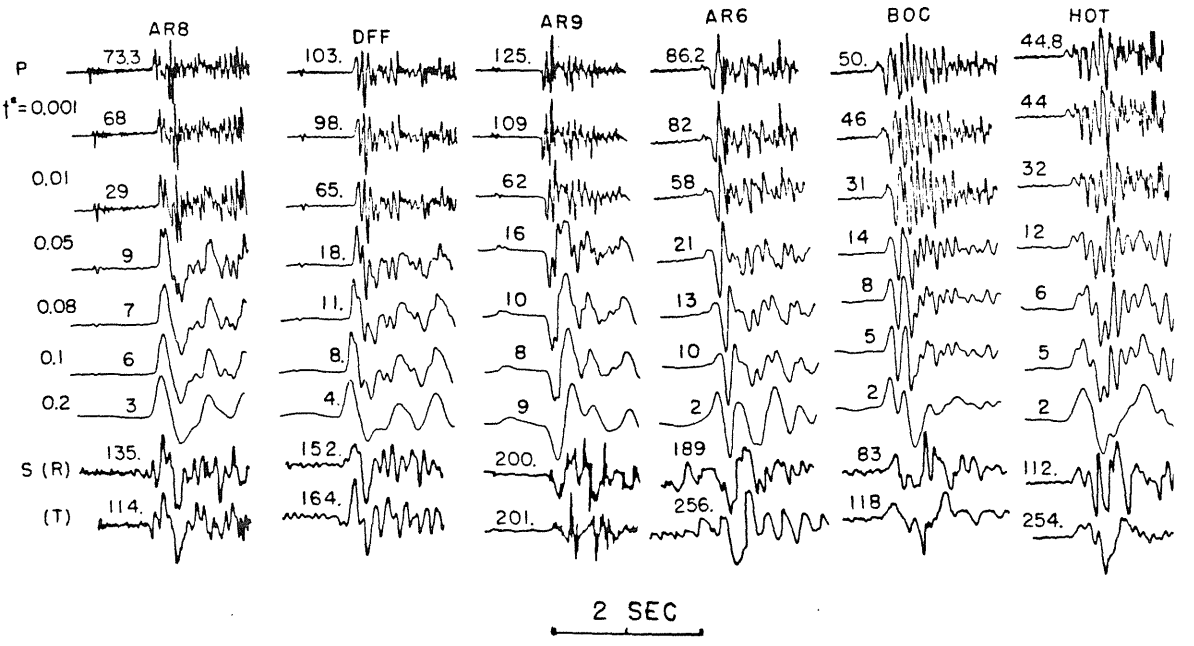

Figure 2-B-10 Comparisons of the resulting vertical seismograms after convolving with Futterman Q operators. The top traces are vertical accelerograms (P-waves) recorded from stations AR6, AR8, AR9, DFF, HOT and BOC. The bottom two traces are horizontal accelerations (S-waves). The numbers are the amplitudes.

very different mechanism.

As suggested by Le Bras (1982) and Hartzell and Helmberger (1982), the strongest asperity in the mainshock was located about 10 km south of the array and a depth of 5 km to 10 km. The duration of rupturing through this asperity is about 2 seconds. The close proximity of 23:19, October 15 aftershock to the major asperity in mainshock as inferred by Hartzell and Helmberger (1982) allows us to use the same Green's functions to invert the possible source mechanism which caused the high amplitude motion in mainshock. In Figure 2-B-12, we show these accelerations recorded in stations AR4, AR5, AR6, AR7 and AR8 (230° component). The time segment, T, shown in Figure 2-B-12, represents this about 2.5-second coherent long-period phase, bounded by a very strong starting phase and weaker ending phase. The S-P times for these strong phases are very close to the S-P times observed in the 23:19, October 15 aftershock and presumably they arrived from the same hypocentral region. We therefore propose to use the same method to study the possible mechanism that initiated the asperity rupturing.

We apply a band-pass filter (high-cut at 5 Hz and a ramp rising from .7 to 1.25 Hz) to the horizontal accelerations at stations AR4, AR5 and AR8. Stations AR6 and AR7 are not used due to their proximity to the fault. Although the locations of this asperity in the mainshock and the 23:19, October 15 aftershock are very close, the waveform differences indicate that the mechanisms may be different. The amplitudes of the accelerations in October 15, 23:19 aftershock are about two-thirds of those seen in mainshock. We use the same inversion method to study the filtered mainshock accelerations for stations AR4, AR5 and AR8. The time segment used in the integration is 1.2 seconds. The best solution

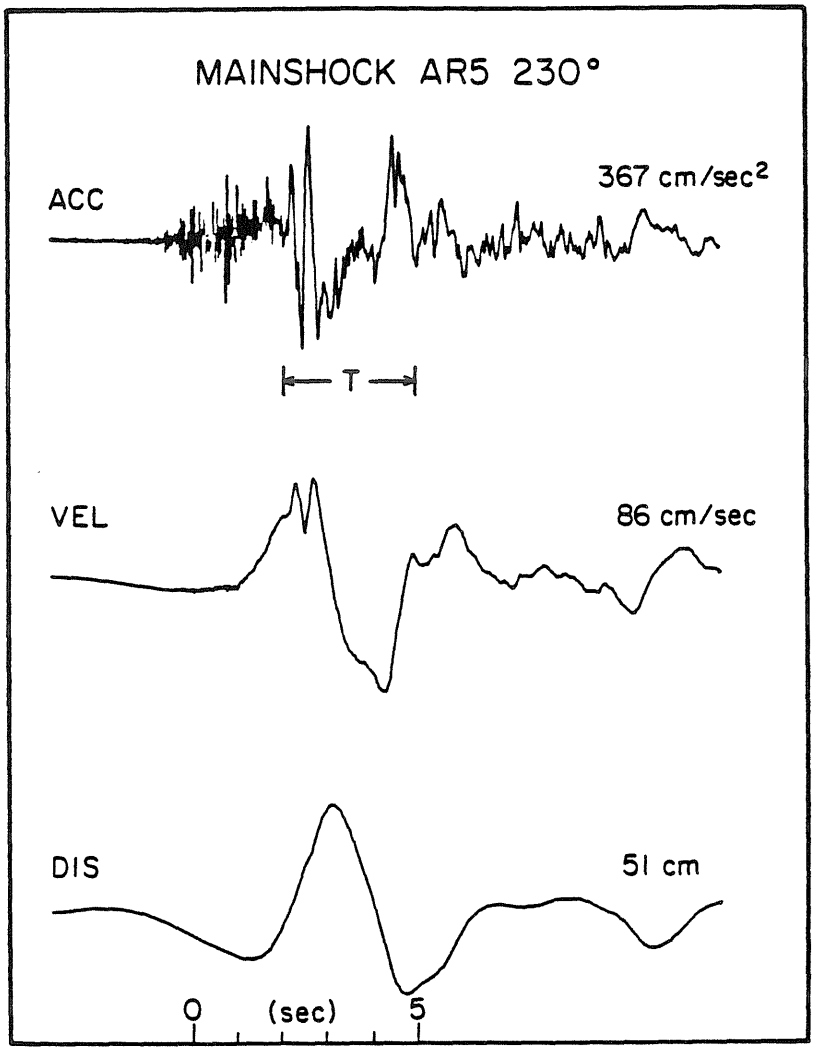

Figure 2-B-11 The ground acceleration, velocity and displacement recorded at array station AR5 (230°) for the October 15, 1979 Imperial Valley mainshock.

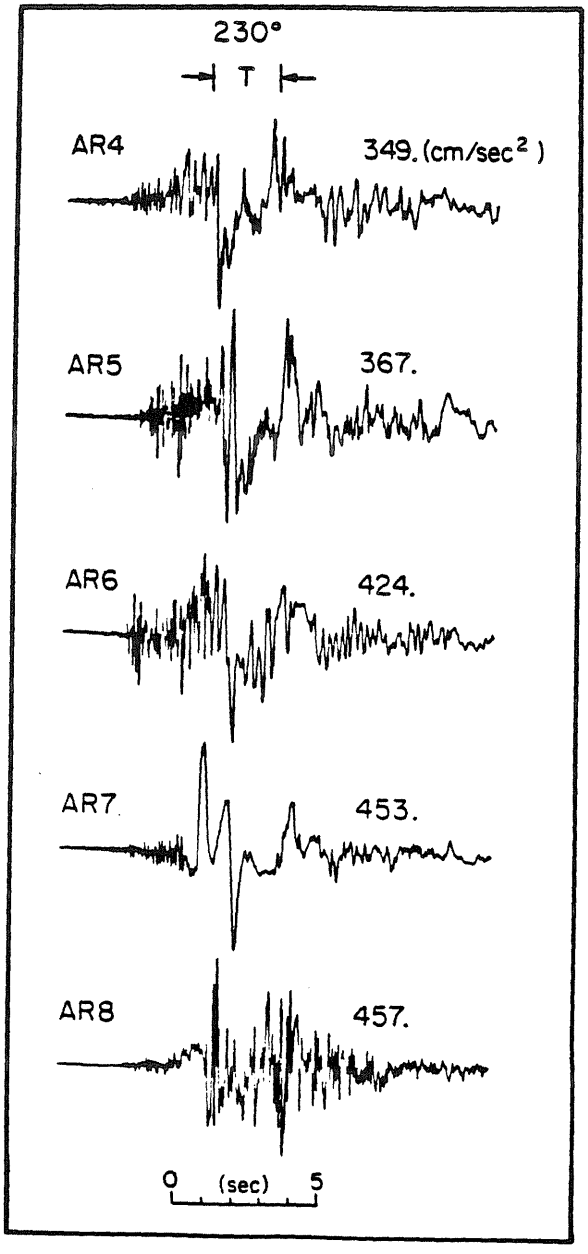

Figure 2-B-12 The ground accelerations (230°) at stations AR4, AR5, AR6, AR7 and AR8 recorded from the 1979 Imperial Valley mainshock.

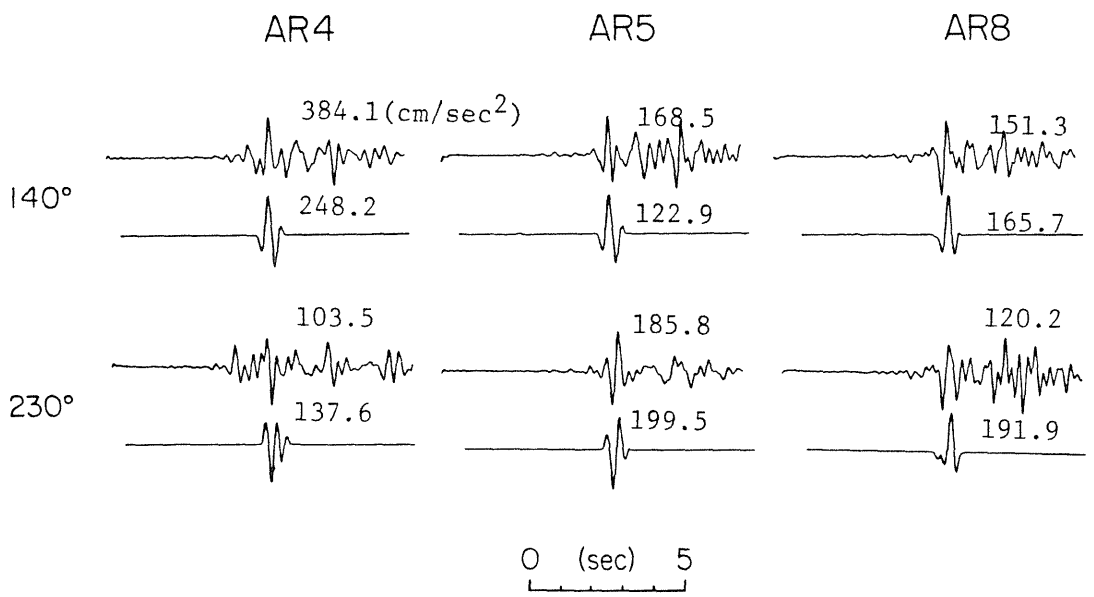

Figure 2-B-13 Comparisons of filtered horizontal ground accelerations vs. the inversion solution at array stations AR4, AR5 and AR8 from the 1979 Imperial Valley mainshock.

we obtained consists of two point sources with .2 seconds time delay; the first source has a seismic moment of $.25\times10^{25}$ dyne-cm and has strike=N333°E, dip=N76°E and rake=249°, and the second source has a moment of $.4\times10^{25}$ dyne-cm and strike=N356°E, dip=N76°E and rake=111°. Figure 2-B-13 shows the comparison of the filtered accelerograms vs. the synthetic seismograms for this solution. This mechanism suggests that the initial motion was dominated by thrust faulting on a nearly vertical plane. Although the solution is not well constrained due to the limited number of high quality stations used in this study, it suggests that the mechanism of initiation of rupturing can be very different from the over-all motion.

Discussion and Conclusion

In this section we will address the amplitude attenuation properties of the peak ground acceleration (PGA) data as conventionally treated in the engineering community. As shown in Figure 2-B-14, we include panels of filtered data for the October 15, 23:19 aftershock in the analyses. A list of the filtered data is given in Table 2-B-4. By examining these amplitude-distance plots in light of the modeling results, we will attempt to explain the large scatter seen in the PGA data in terms of the known source and propagational features, namely, site effects, directivity, and radiation patterns.

First, note that the amplitudes appear to decay by about a factor of two going from 8 km to 18 km which is about the rate found in other studies, e. g. see Hadley et al. (1982). From these plots we observe that the most anomalous station appears to be AR6 which has an especially large amplitude at longer periods. This station produced anomalous signals for the main event with very

interesting particle motions as discussed at length by Rial and Scott (1983). The S-wave apparently arrives late at this station as indicated in Table 2-B-2. On the other hand, we note that the accelerations recorded at station AR10 are smaller than the average at all frequencies and its S-wave arrival is earlier than normal travel time. Amplitudes for the main event are also low at this particular station, which suggests that these effects are caused by receiver structures. Early arrival time indicates a harder site which would probably suppress some of the surface amplification which occurs at the other stations. Thus, some of this scatter is caused by site effects which could be determined by other geophysical means independent of these earthquake generated motions.

Comparing station AR5 and Bonds Corner (BOC), it appears that the ground accelerations in AR5 are larger than the average, whereas at BOC they are smaller. However, this difference is no longer seen at accelerations filtered at 1-sec. We interpret this as a directivity effect, where the source ruptured through about 1 km length of fault towards the north, and produced high-amplitude, high-frequency accelerations at station AR5 (northern station) and low-amplitude, longer-period accelerations at BOC (southern station) as discussed earlier.

Finally, we address the question of radiation pattern as the usual cause for high frequency signals. Generally, seismologists plot the amplitudes as a function of azimuth for strike-slip faults and observe a classical four-lobed pattern for long period signals. However, in this situation where receiver and directivity effects are prevalent we need to modify this presentation slightly. It appears that dividing the tangential motion (T) and radial motion (R) by the root-mean-square is one way to suppress these complications, since the S-waves

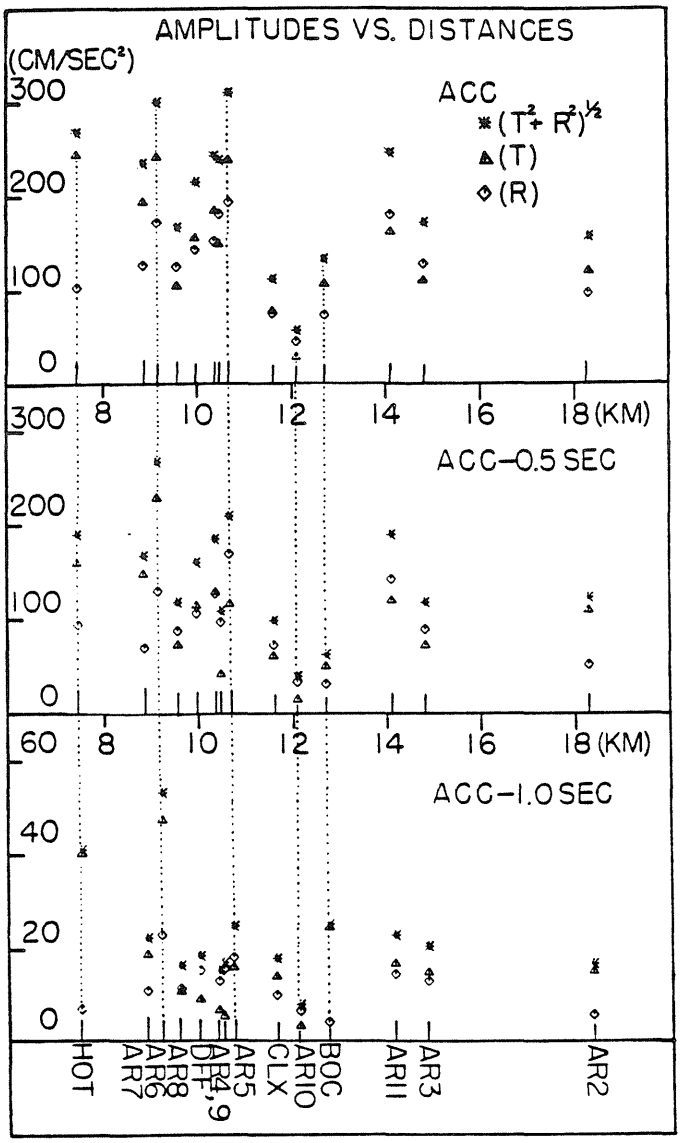

Figure 2-B-14 Amplitude vs. distance plots for ground accelerations and filtered accelerations (band passed filters near .5-sec and 1.0-sec).

Table 2-B-4 Peak Amplitudes

Station	Acc.(R)	Acc(T)	.5-sec(R)	.5-sec(T)	1-sec(R)	1-sec(T)
AR1	35.28	66.79	20.80	57.96	4.59	8.10
AR2	104.27	127.69	57.69	115.42	7.48	16.75
AR3	136.15	118.29	96.65	79.80	14.59	16.45
AR4	161.13	193.43	136.77	138.43	14.44	8.26
AR5	202.38	247.24	178.80	125.81	19.55	17.41
AR6	180.90	251.04	140.12	238.47	24.28	48.77
AR7	135.88	203.28	79.80	158.34	12.39	20.09
AR8	134.29	113.65	97.57	82.54	12.88	12.24
AR9	189.78	158.05	106.40	51.04	17.10	6.94
AR10	54.11	37.57	41.91	23.59	8.17	4.94
AR11	188.68	170.42	150.41	128.00	16.08	18.36
DFF	152.35	164.38	116.12	124.16	16.74	10.62
HOT	112.52	253.95	104.50	170.48	8.46	41.47
BOC	81.97	115.02	39.69	58.54	5.86	26.02
CLX	84.03	86.43	81.49	69.70	11.56	15.48
BRW	49.08	59.35	30.80	29.83	1.77	4.39

* The filter used for .5-sec window has a high-cut at 5 Hz and a ramp rising from 1 Hz to 1.25 Hz. Similarly, the 1.0-sec filter has a high-cut at 1.3 Hz and a ramp rising from .6 to .7 Hz.

should be affected in roughly the same manner at each station. These normalized amplitude plots as a function of frequency are displayed in Figures 2-B-15(a) and 2-B-15(b) for the transverse and radial components, respectively. We have also included the the synthetic modeling results for comparison. However, for higher frequencies, there does not appear to be much evidence for distinct nodes especially in the tangential motions. This feature can be simulated by complex faulting where the strikes of the two sources have slightly different orientations, as the two-source radiation pattern indicated in Figures 2-B-15(a) and 2-B-15(b).

In conclusion, we found that one of the best recorded aftershocks to date could be modeled reasonably well by assuming a complex rupture involving two sources; the first source (strike=N319°E, dip=42°NE, and rake=165°) has a moment of $.7\times10^{24}$ dyne-cm and the second source (strike=N324°E, dip=82°SW, and rake=181°) lies about 1 km to the north and has a seismic moment twice that of the first source. We obtained these source parameters by applying the amplitude inversion method with all the other parameters fixed. The advantage of this inversion method is the usage of the relative amplitude information which can provide better constraints on the source mechanism. However, there are many uncertain factors which can introduce noise in the amplitudes, among these the source time function is the most important one. In this study, the source time function for each station is derived from a trial and error result.

The source parameters derived from horizontal strong motion velocities can also model the observed vertical velocities at least at the six available stations. This constrains the moment of longer-period P waves and quantifies the apparent attenuation difference for high-frequency P- and S-waves. It is

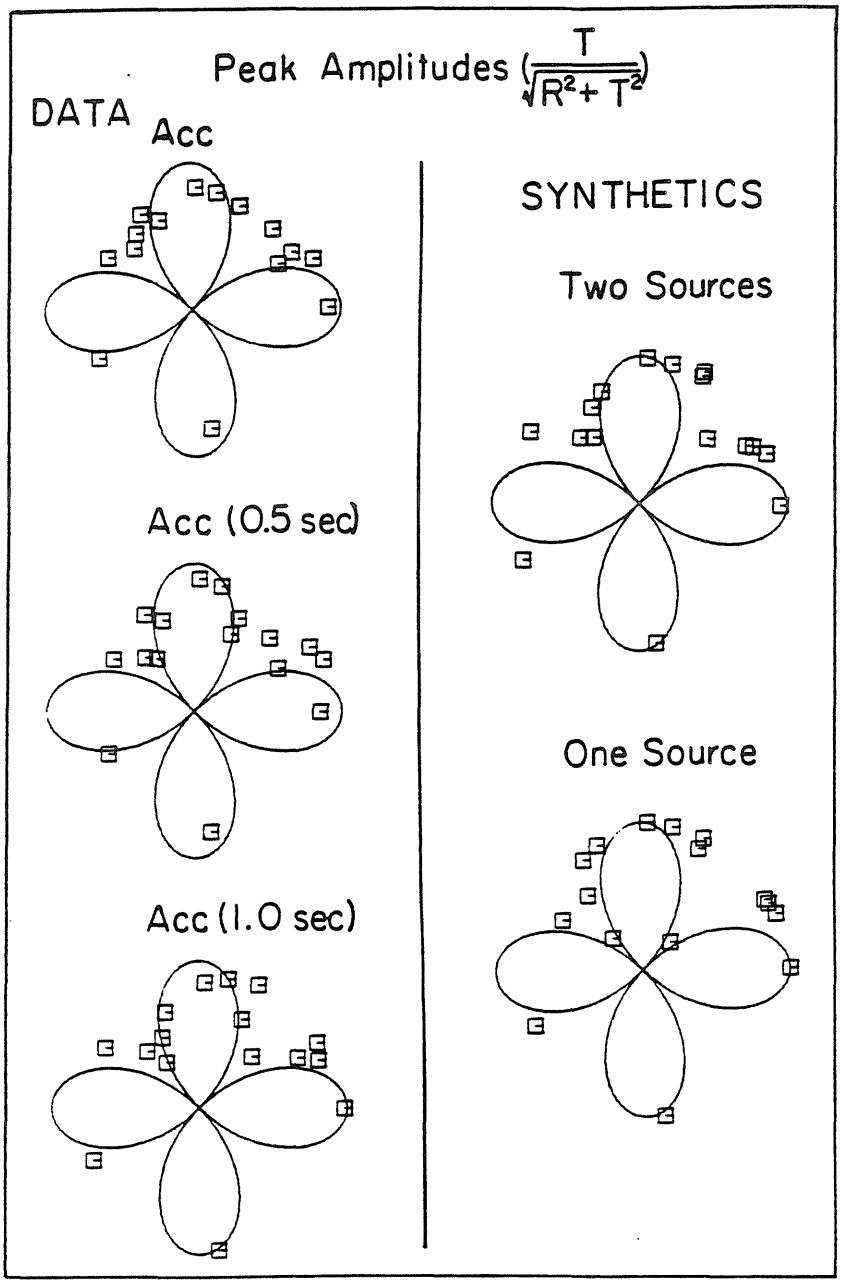

Figure 2-B-15(a) The normalized amplitude plots for the ground accelerations in transverse components. The left column illustrates the radiation patterns from the recorded accelerations and filtered accelerations (passed bands near .5-sec and 1.0-sec). The right column shows the radiation patterns from both two-source and one-source solutions.

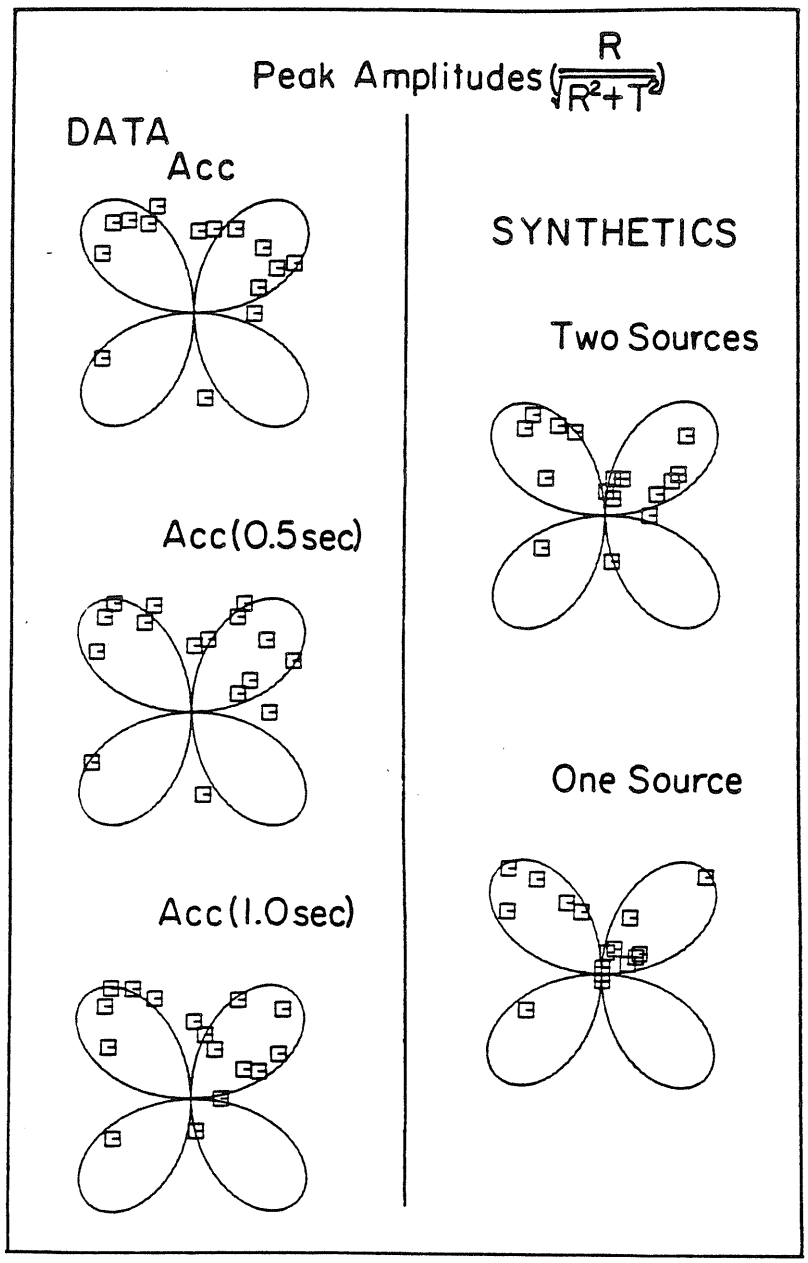

Figure 2-B-15(b) The normalized amplitude plots for the ground accelerations in radial components.

suggested that high shear loss in high-frequency waves is the main cause of the anomalous waveform and frequency differences seen in vertical and the horizontal accelerations. We suggest that a layered basin structure separates the P waves from the S waves onto vertical and horzontal components. The high apparent attenuation for S waves, mainly in the very top 1 km of the sediments, is responsible for producing low amplitude and the longer-period S phases. The t_α^* of 0.001 and t_β^* of about .08 to .1 can explain this commonly observed feature for P- and S-waves seen in this sedimentary basin.

Chapter 3 Array Analysis of the Ground Motions from the 1971 San Fernando California Earthquake

Introduction

An important new field of strong ground motion research is modeling of an earthquake source and the associated wave propagation in a deterministic way. This type of modeling has significantly increased our understanding of the longer-period parts of strong ground motions. However, a proper model is often difficult to obtain. An accurate characterization of the wave phenomenon, (e.g., wave types, coherent phase velocities, propagation direction and the wave variability) is essential to evaluate the validity of the models.

Hanks (1975) analyzed the ground displacements from the 1971 San Fernando strong-motion data and found strong coherence appeared in the longer-period waves. He also identified direct shear phases and subsequent surface waves at certain ranges. However, a deterministic source model for the 1971 San Fernando event is still uncertain as pointed out by Heaton (1982). Heaton constructed models consisting of finite faults within a half-space to explain waveforms observed at 5 strong-motion stations as well as long-period teleseismic body waveforms. His preferred finite source model implies a fairly complex double source earthquake, with two events of approximately equal size and separated by about 4 seconds. However, modeling of this type is limited by our incomplete knowledge of the strong motions propagating through the complex

structure encountered in the real earth. Thus, we believe that there is a great need for a detailed description of the wave types represented by the ground motions.

In this study, we extend Hanks' study (1975) to examine the ground velocities and accelerations observed by the accelerograph array during the 1971 San Fernando earthquake. A display of the ground velocity profiles together with the topographic features and geologic structure (Yerkes et al., 1965) will be presented and possible wave types and apparent phase velocities will be discussed.

Given the distribution of strong motion recordings of the San Fernando earthquake, it is possible to construct profiles along three azimuths. Figure 3-1 shows the station distribution and corresponding profiles. All profiles originate in the epicentral region. Profile I extends 65 km southward across the San Fernando and Los Angeles basins to a station on the Palos Verdes Peninsula. Profile II extends 95 km S40°E along the front of the San Gabriel mountains and then across the San Gabriel and Los Angeles basins. Profile III runs 90 km N40°W across the San Gabriel and Tehachapi mountains.

The San Fernando earthquake was also well recorded by strong motion instruments which are required in high-rise buildings. These buildings are clustered in three locations on the north side of the Los Angeles basin; the Miracle Mile area of Wilshire Boulevard (local array 1), downtown Los Angeles (local array 2), and Century City (local array 3). Station locations for these dense local arrays are shown in Figure 3-2.

Time histories of ground velocity and acceleration are all taken directly from EERL, Caltech reports (1974). Ground motions are rotated into radial,

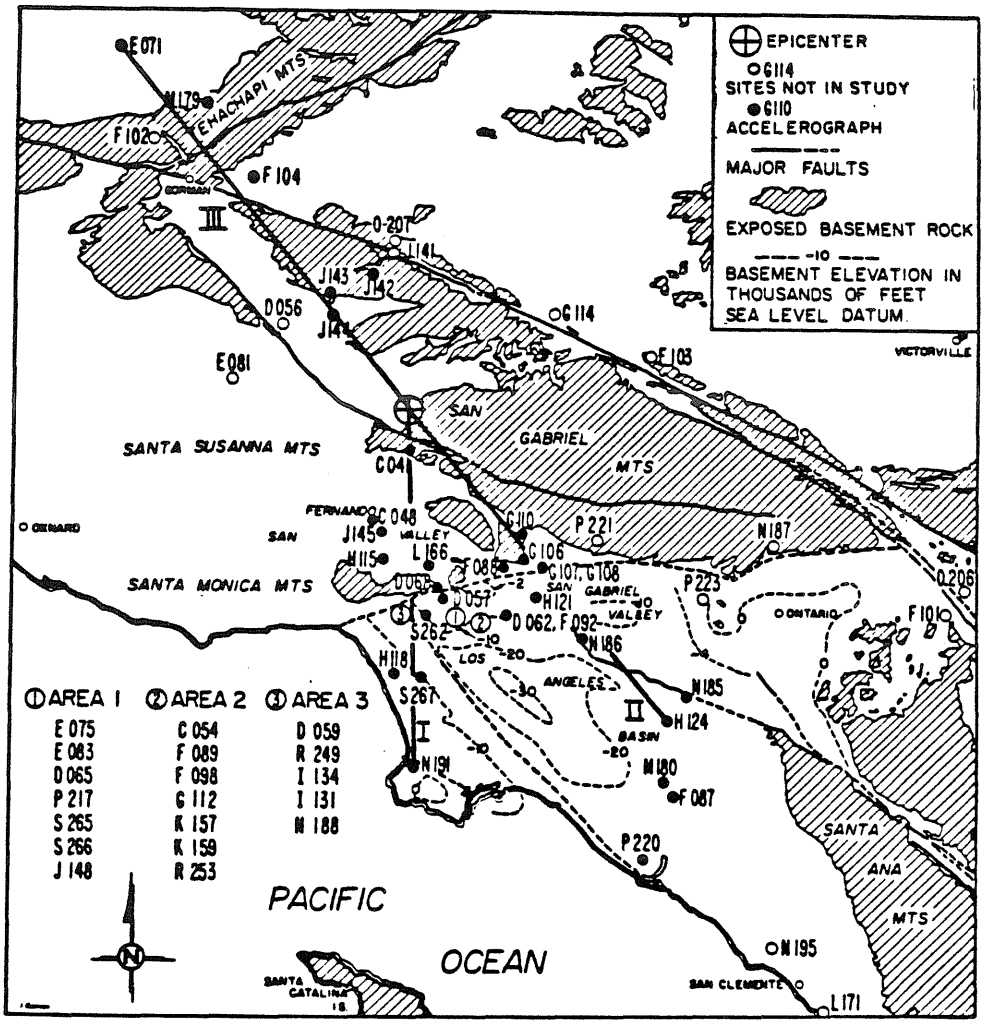

Figure 3-1 The long profiles, I, II and III, and site locations of accelerometer recordings of the 1971 San Fernando earthquake (modified from Hanks, 1975).

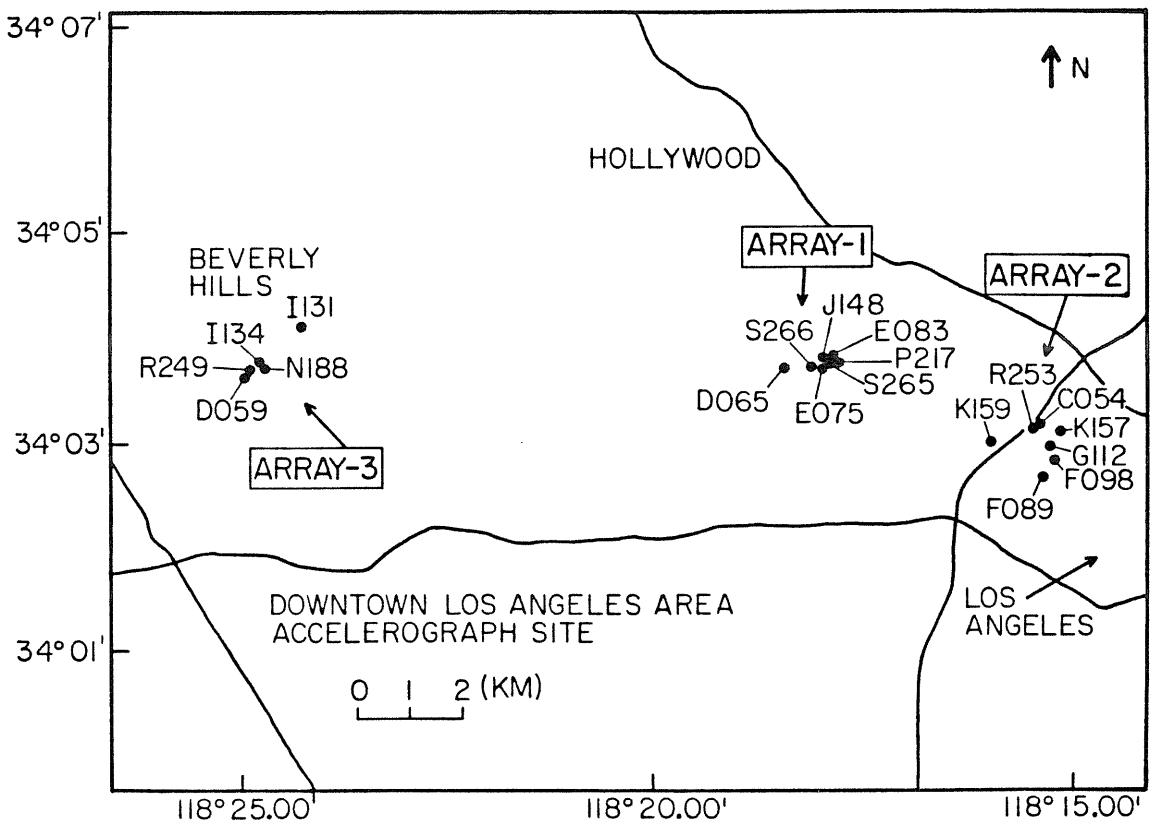

Figure 3-2 The site locations of 3 local arrays used in this study.

transverse, and vertical components and are then displayed as functions of time and distance from the epicenter as reported by Allen et al. (1973). Since absolute time is not available for any records, some assumptions need to be made to correlate phases from one station to another. We shifted records such that the apparent first shear-wave arrivals, which are named S! by Hanks (1975), are aligned vertically in the profile. S! minus trigger times are listed in Table 3-1 for all stations used in this study. Unfortunately, in some cases, the identification of S! is very difficult, and thus some of the more distant stations are probably not aligned on the first shear-wave arrival. Once the profiles are constructed, we find that the ground velocity waveforms are surprisingly coherent from station to staion, allowing us to estimate apparent phase velocities, to identify possible wave types, and qualitatively separate the source from the path effects. The features of each profile will be described in more detail as follows.

Long Profiles

a. Profile I. The velocity traces together with the corresponding free surface and basement surface topography profiles are displayed in Figure 3-3. Velocity traces begin with the S! arrivals. The two-fault system suggested by Heaton (1982) is also illustrated in the same Figure. H1 is the first hypocenter which ruptured along the Sierra Madre fault, and 4 seconds later, the second hypocenter H2 initiated on the San Fernando fault. According to Heaton's (1982) interpretation, the high peak velocity observed at station C041 (Pacoima Dam) is caused by rupture directivity along the Sierra Madre fault. Although the faulting process is rather complicated, the total source time duration is only about 7 seconds. We believe that the signal duration at Pacoima Dam (C041)

Table 3-1 S! minus trigger times

Station	Time(sec)	Station(#Fl.)	Time(sec)
Azimuth I		Local Array-1	
C041	3.0	D065(11)	0.0
C048	1.6	E075(11)	1.3
D057	1.1	E083(7)	0.8
D068	0.0	J148(17)	5.6
H115	4.0	P217(12)	0.8
H118	0.0	S265(31)	5.6
J145	1.6	S266(21)	5.6
L166	1.3	Local Array-2	
N191	0.0	C054(39)	1.3
S262	1.9	F089(8)	5.1
S267	6.1	F098(8)	4.5
Azimuth II		G112(43)	1.9
G110	1.3	K157(16)	2.7
G106	2.1	K159(8)	4.3
G108	4.3	R253(10)	5.6
H121	5.6	Local Array-3	
M180	0.0	D059(19)	0.0
F087	0.0	I131(10)	5.6
N186	0.0	I134(15)	6.1
P220	0.0	N188(16)	5.6
Azimuth III		R249(27)	5.1
E071	0.0		
F102	0.0		
F104	0.0		
J142	5.0		
J143	0.0		
J144	0.0		
M179	0.0		

Building height in terms of floors.

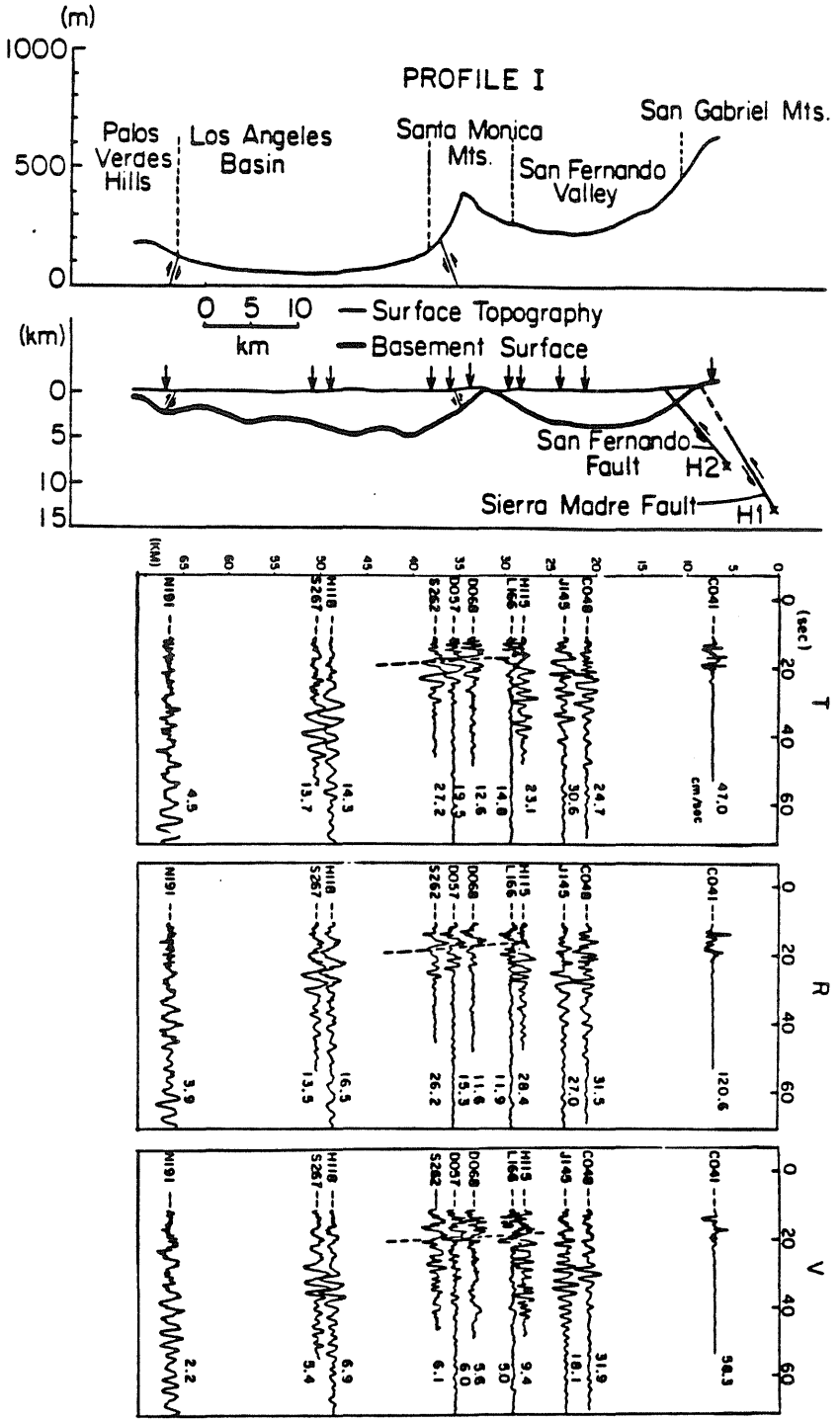

Figure 3-3 Transverse, radial and vertical components of ground velocity along profile I. The corresponding free surface and basement surface are shown on the top. Dashed lines crossing 30 km to 40 km indicate the possible phase arrivals of the surface waves.

represents the approximate duration of the source.

One of the most impressive features seen in Figure 3-3 is the correlation of ground motion waveform with the topography of the subsurface basins. There are three stations C048, J145 and H115 located within the San Fernando Valley. The waveforms recorded at these stations are poorly correlated and the signal durations are about 30 seconds. These durations are much longer than those seen at neighboring and more distant stations located near Santa Monica Mts., such as L166, D068 and D057. This contrast can easily be seen in Figure 3-3. Coherent waveforms begin to appear at station L166 and signal durations drop to only about 10 seconds. Furthermore, the amplitudes also drop quite drastically by about one-half after passing the San Fernando Valley stations. Amplitudes again increase at stations D057 and S262 when the waves reach the Los Angeles Basin. The waveforms are quite coherent in the beginning 6 seconds and there appears to be little moveout from the S! phase. The dashed lines passing stations L166, D068, D057 and S262 indicate the possible arrival of surface waves, which are characterized by gradual moveout from the S phases. They also appear dispersive in nature, this was also suggested by Hanks (1975) from his study of particle trajectories. It seems that, at epicentral distances of near 30 km, body waves dominate the waveforms at the bedrock sites, and the surface waves start to develop rapidly from there. For epicentral ranges beyond 40 km, surface waves start to dominate the wavetrain. At ranges of 50 km and beyond, it is hard to identify the body waves. Most of the signals appear to be surface waves with visibly dispersive character. The apparent moveout velocity of the surface wave phase from S! phase is estimated to be 5.7 km/sec. If we assume that the phase velocity corresponding to the S! phase is 3.5 km/sec, then the

phase velocity of these surface waves is about 2.2 km/sec.

It is useful to contrast the nature of wave propagation for waves observed in the San Fernando valley and the Los Angeles basin. Peak ground velocities observed in both basins are high with respect to sites in the Santa Monica mountains. Although long-period surface waves are clearly visible in both basins, the duration of these surface waves is up to 20 seconds longer in the San Fernando valley, the basin which is closer to the earthquake source. The earthquake ruptured into the northern part of the San Fernando valley which is a closed sedimentary basin. Thus it is likely that the long signal durations are caused by surface waves which are trapped within the valley, thereby causing severe ringing. The short signal durations seen at adjacent stations indicates that these reverberating waves which developed in the San Fernando valley did not propagate away from the valley. The interpretation from the numerical simulation result will be presented later.

In Figure 3-4, we show the radial components of the ground acceleration for stations located along profile I. Traces begin at their trigger time and are aligned vertically with the S! phase. Although there is considerable variation in the observed waveforms from station to station, the duration of the high-frequency motions is a fairly constant 10 seconds. Furthermore, strong phases can be seen on many records at about 4 seconds and 8 seconds after the initial S arrivals. We speculate that the overall duration and timing of arrivals seen on the relatively high-frequency acceleration time history is directly related to the details of the faulting process. It is suggested that the basin geometry has less effect on these higher frequency waves.

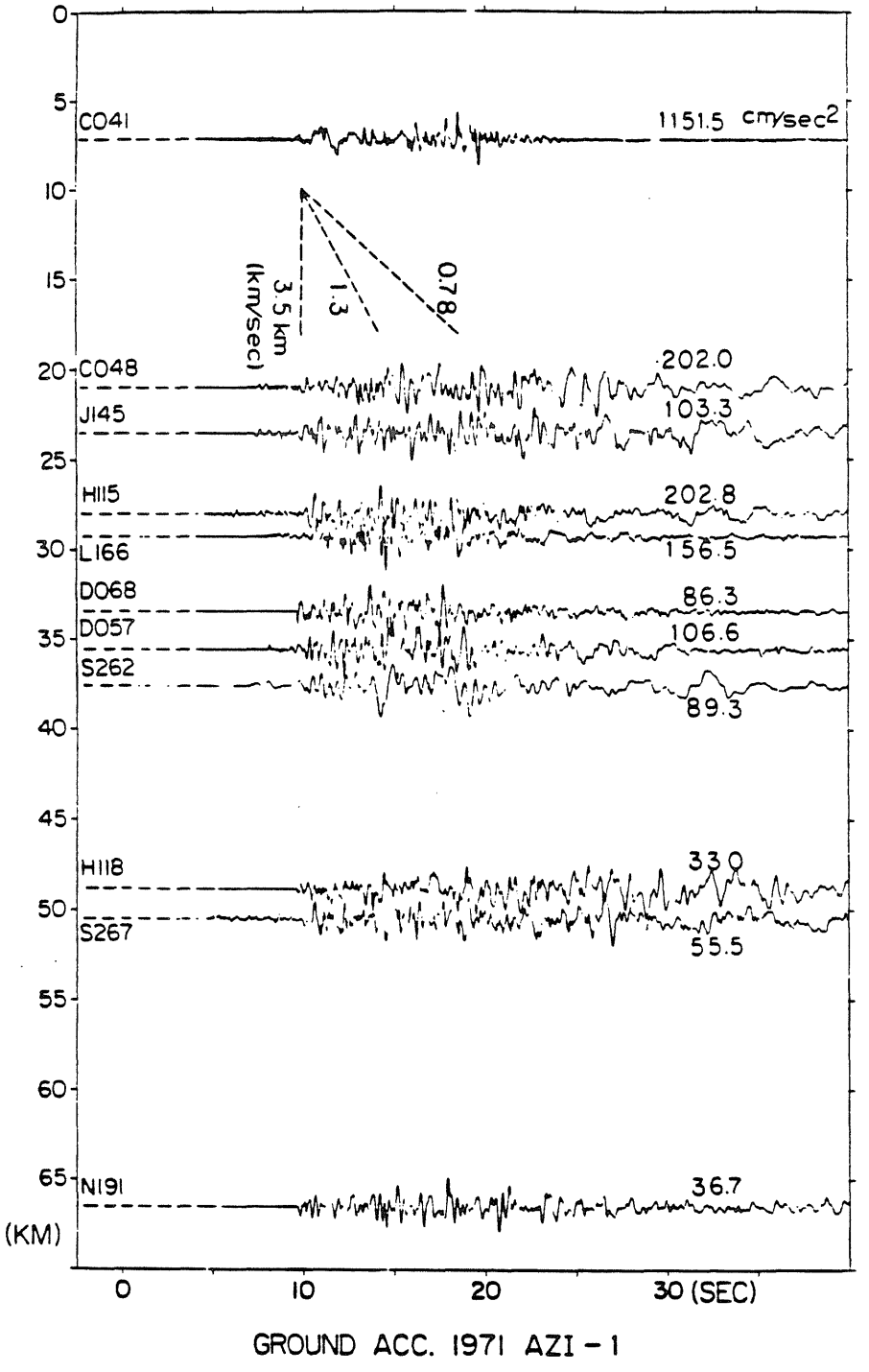

Figure 3-4 The radial component of ground acceleration along profile I.

b. Profile II. Profile II is roughly along the southwest border of the San Gabriel mountains and part of the Los Angeles basin. The velocity traces (beginning at S!) together with the path profile are shown in Figure 3-5. Somewhat different features are observed along this profile. The signal duration of what appear to be mainly the S! phase is about 8 seconds at station G110. Surface waves develop gradually with distance from there. The amplitudes along this path are, on average, lower than those in Profile I. Perhaps part of the reason for this is the lack of thick sediments along profile II from about 30 km to 50 km. Well dispersed surface waves can hardly be identified at this portion of the profile. Instead, the S! phase, which is characterized by zero moveout can still easily be recognized. Even at station N186, which has an epicentral distance of 52 km, the high-frequency S! phase can still be identified, this suggests that the relatively thin sediments along profile II prohibit the rapid development of the surface waves seen in profile I. However, there may still be a strong fundamental Rayleigh wave which is hard to distinguish from the S wave (see Heaton and Helmberger, 1979). The dashed lines crossing station G110 to station N186 indicate the possible surface wave phases. If we assume a horizontal phase velocity of 3.5 km/sec for the S! phase, then the phase velocity corresponding to the dashed line is approximately 2.7 km/sec.

In Figure 3-6, we show the radial components of the ground acceleration for stations located along Profile II. Peak amplitudes and the duration of high-frequency shaking are remarkably similar to that seen along Profile I. However, the strong phases seen at 4 and 8 seconds in S wavetrain on Profile I are not as evident in Profile II. Instead, the strongest phase seen along Profile II appears to be about 6 seconds after the beginning of the S wavetrain.

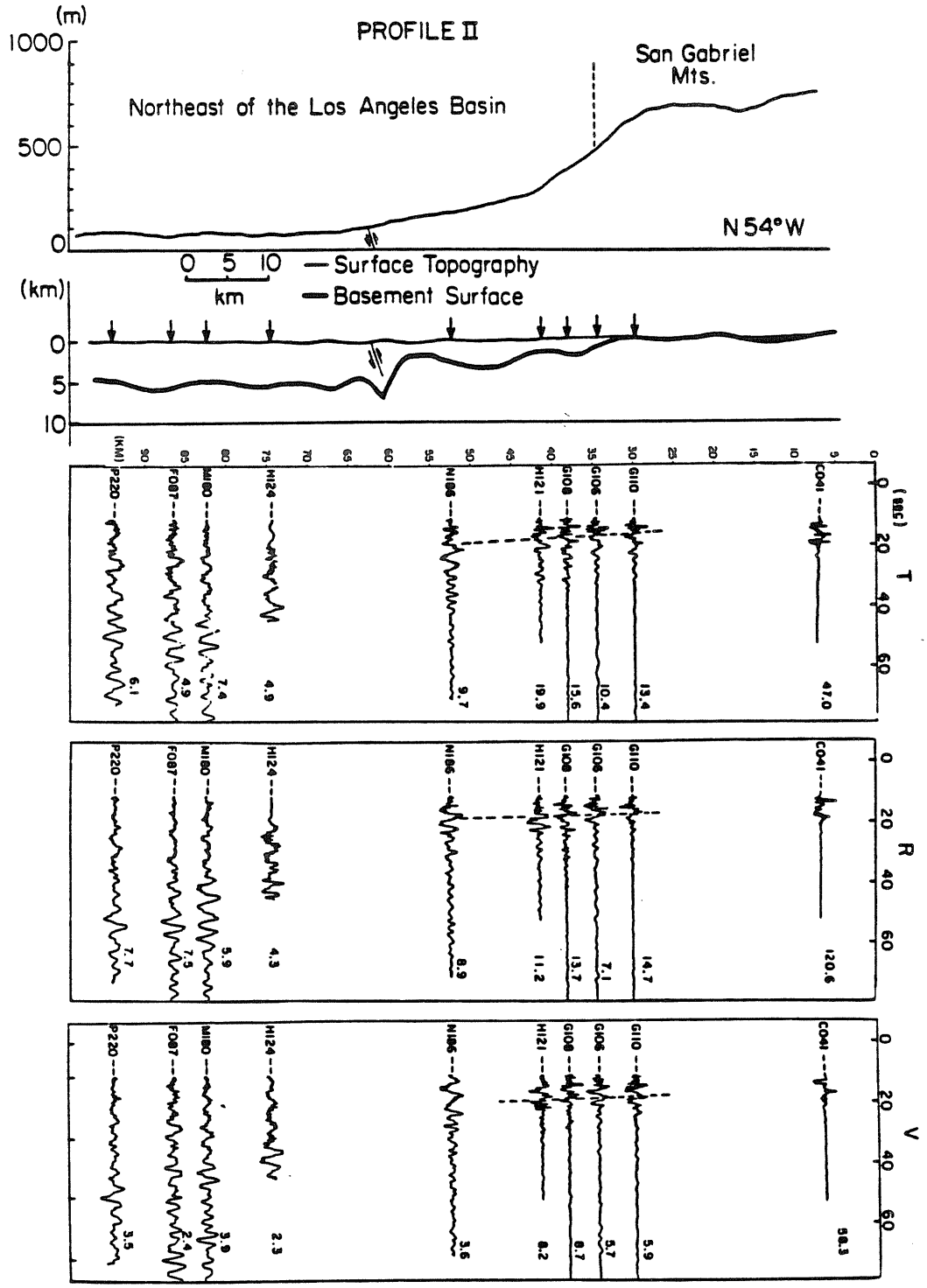

Figure 3-5 Transverse, radial and vertical components of ground velocity along profile II. The corresponding topography and the basement surface are shown on the top. Dashed lines indicate the possible phase arrivals of surface waves.

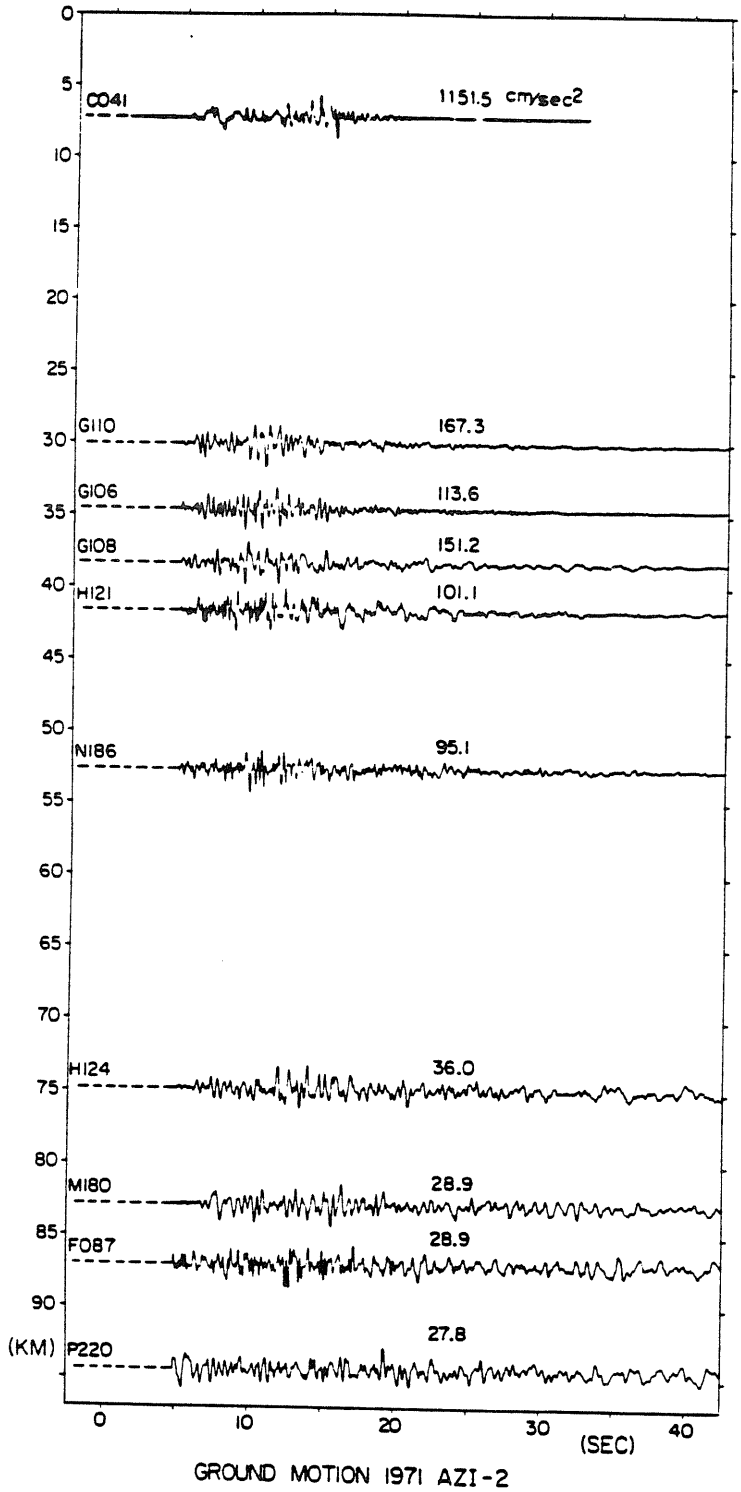

Figure 3-6 The radial component of ground acceleration along profile II.

c. Profile III. Profile III runs N40° W across mostly mountainous terrain and ground velocity traces along this profile are shown in Figure 3-7. Ground velocities are strikingly different along this profile from the other two profiles, which cross deep sedimentary basins. The duration and amplitude of the ground velocity seem to be considerably less on this northern profile. Heaton and Helmberger (1979) shows that displacements observed at station J142 can be reasonably modeled with a simple half-space structure. This is obviously not the case for many of the stations located along profiles I and II.

Radial ground accelerations observed along Profile III are shown in Figure 3-8. Ground accelerations appear to be shorter-period and of shorter duration than those observed along the other two profiles. Furthermore, it is difficult to identify any coherent phases.

In Figure 3-9, we compare peak radial velocities amplitudes along the three profiles. It seems clear that peak velocities are larger on stations to the south, except for those stations on or adjacent to the Santa Monica or San Gabriel mountains. It appears likely that the deep sedimentary basins are the principal reason for this amplitude variation.

In Figure 3-10, we compare peak radial acceleration amplitudes along the profiles. Peak accelerations are surprisingly similar for these three profiles. This conclusion was previously reported by Trifunic (1976). Using data mainly from the San Fernando earthquake, he concluded that peak ground motions were greater on 'soft' sites than on 'hard' sites, with the effect being considerable at long periods and almost negligible at high-frequencies.

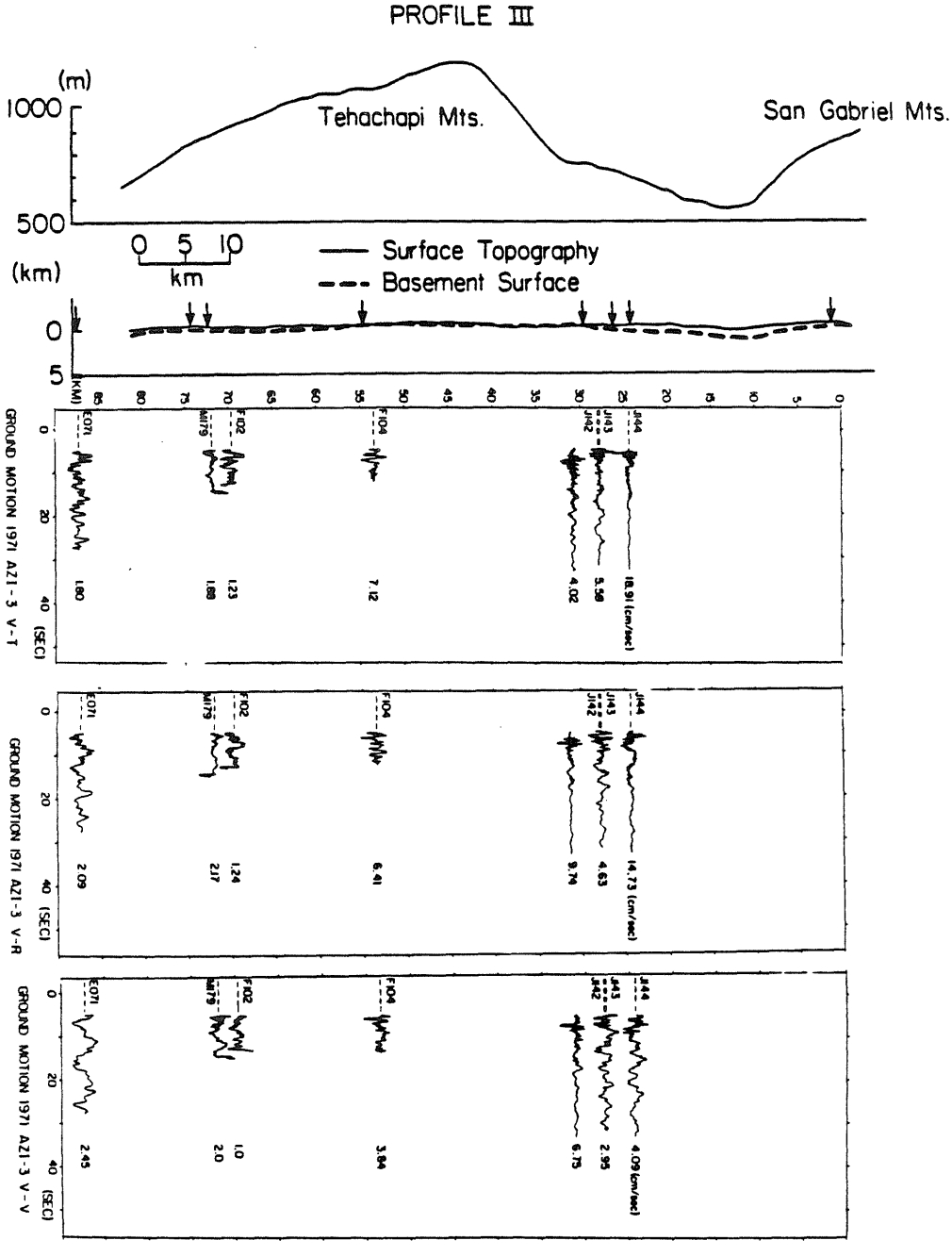

Figure 3-7 Transverse, radial and vertical components of ground velocity along profile III. The corresponding topography and the basement surface are shown on the top.

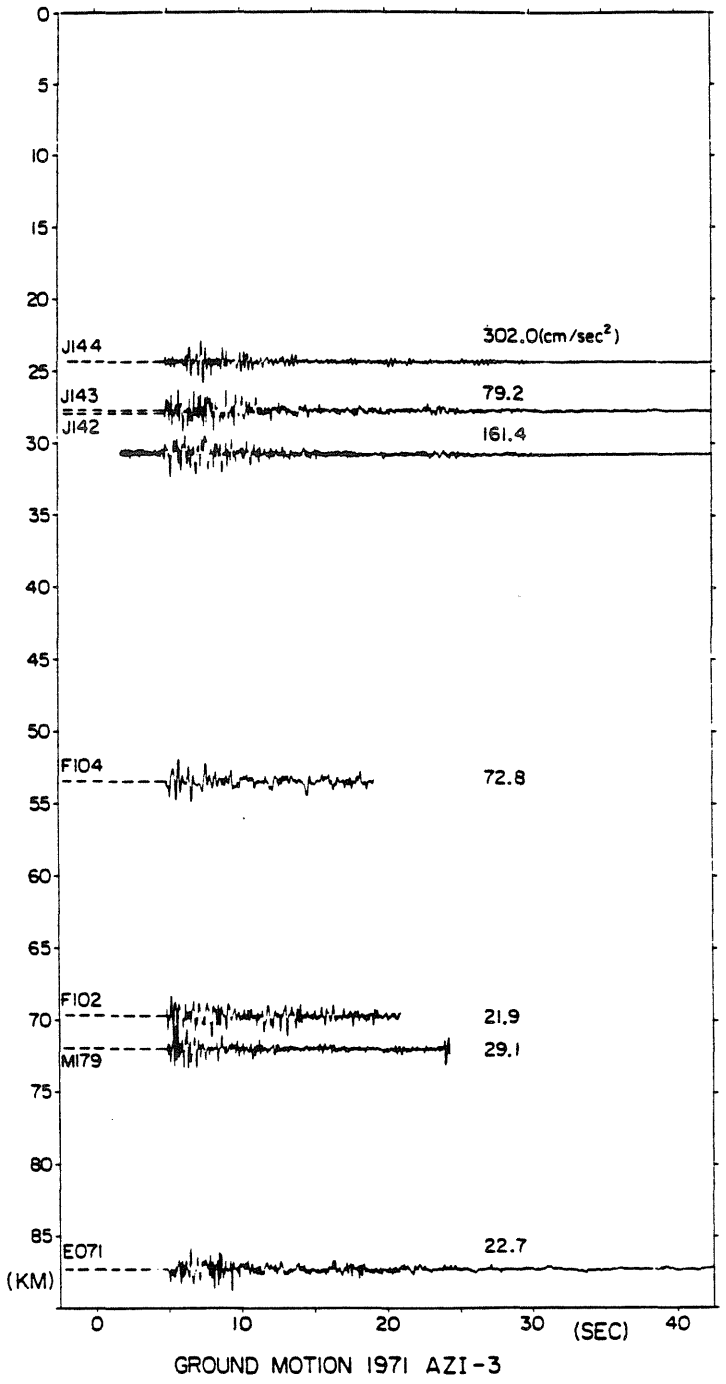

Figure 3-8 The radial component of ground acceleration along profile III.

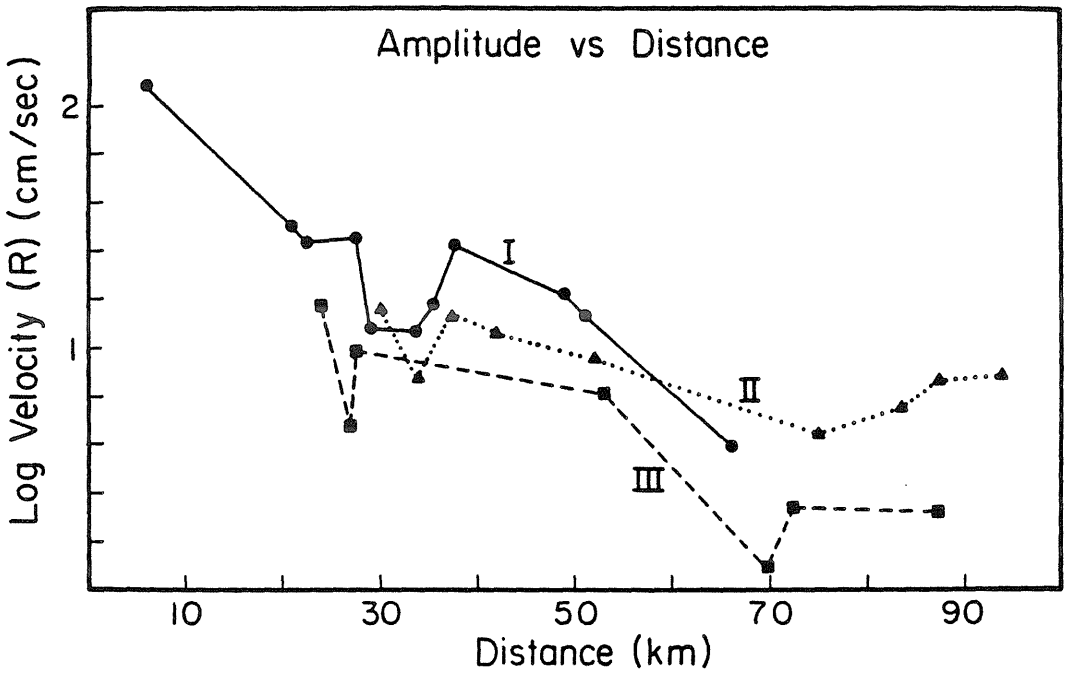

Figure 3-9 Peak radial velocities vs. epicentral distance for the three long profiles.

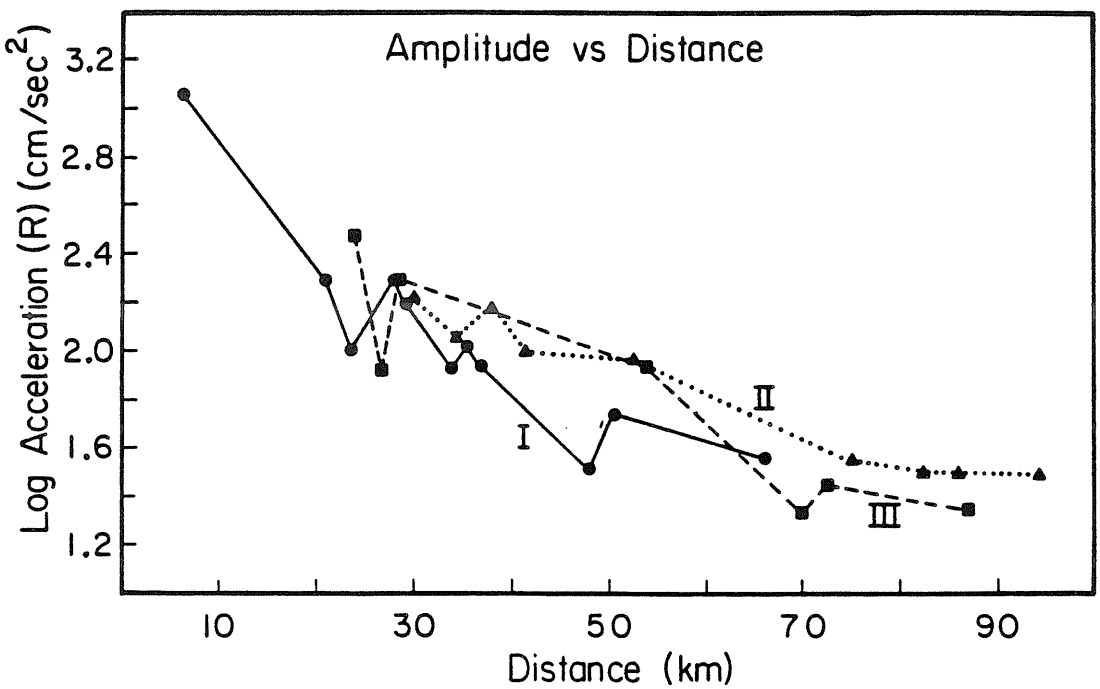

Figure 3-10 Peak radial accelerations vs. epicentral distance for three long profiles, I, II, and III.

Local Arrays

In Figure 3-11, 3-12 and 3-13, we show three components of ground velocity as functions of time and epicentral distance for local arrays 1, 2 and 3, respectively. Since stations in these arrays are not generally aligned along a radial line from the epicenter, the distances shown in Figure 3-11 through 3-13 may not be indicative of the true inter-station spacing.

The most obvious feature of the ground velocity is the remarkable degree of coherence across each array. Since the velocity waveforms are dominated by waves with frequencies of less than 5 Hz, we expect that most of the motion has horizontal wavelengths of greater than 0.5 km. Thus, there is good reason to expect the ground velocity to be coherent over these small arrays. However, there are several other implications of this coherence. First, the record processing must introduce very little noise into the velocity traces. This is especially impressive when one considers that the horizontal components require component rotations before they can be compared. Second, the effect of building interaction is apparently minimal on velocity waveforms. The average standard derivation of peak velocity within each array is about 12%. Furthermore, it is difficult to see the systematic dependence of peak velocity with building height (see Table 3-1) within each array that is suggested by Boore et al. (1980).

We show the radial component of ground acceleration for local array 1 in Figure 3-14. Although less coherent than the velocities, accelerations still show strong coherence along the profile. Prominent phases can be seen at 2, 4, and 8 seconds after the initial S! phase. It is difficult to see moveout of any phase for these local arrays. This is not surprising since a variation in phase velocity between 4 and 2 km/sec yields a moveout of only .25 sec/km. Such small time

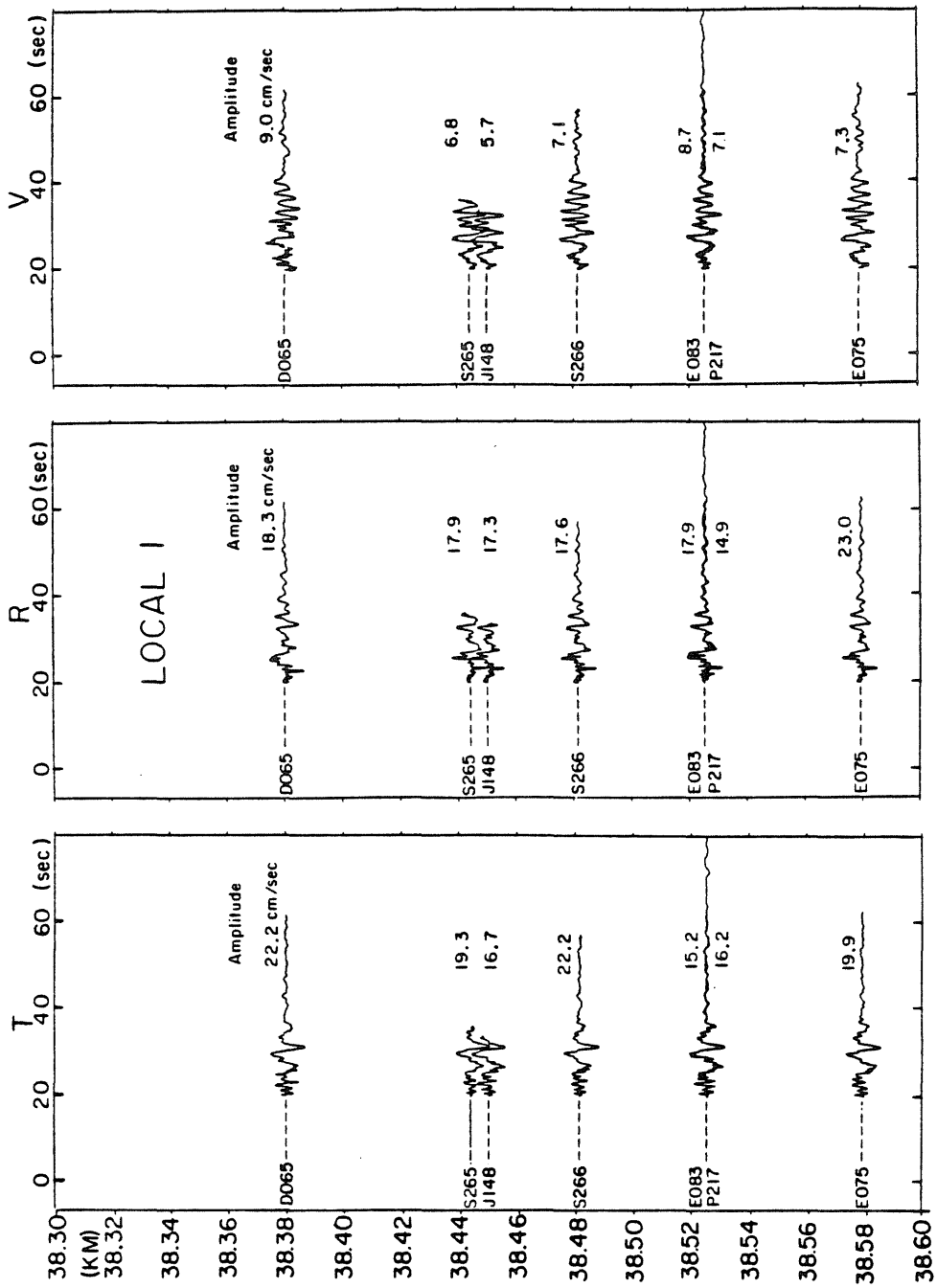

Figure 3-11 Transverse, radial and vertical components of ground velocity in local array-1.

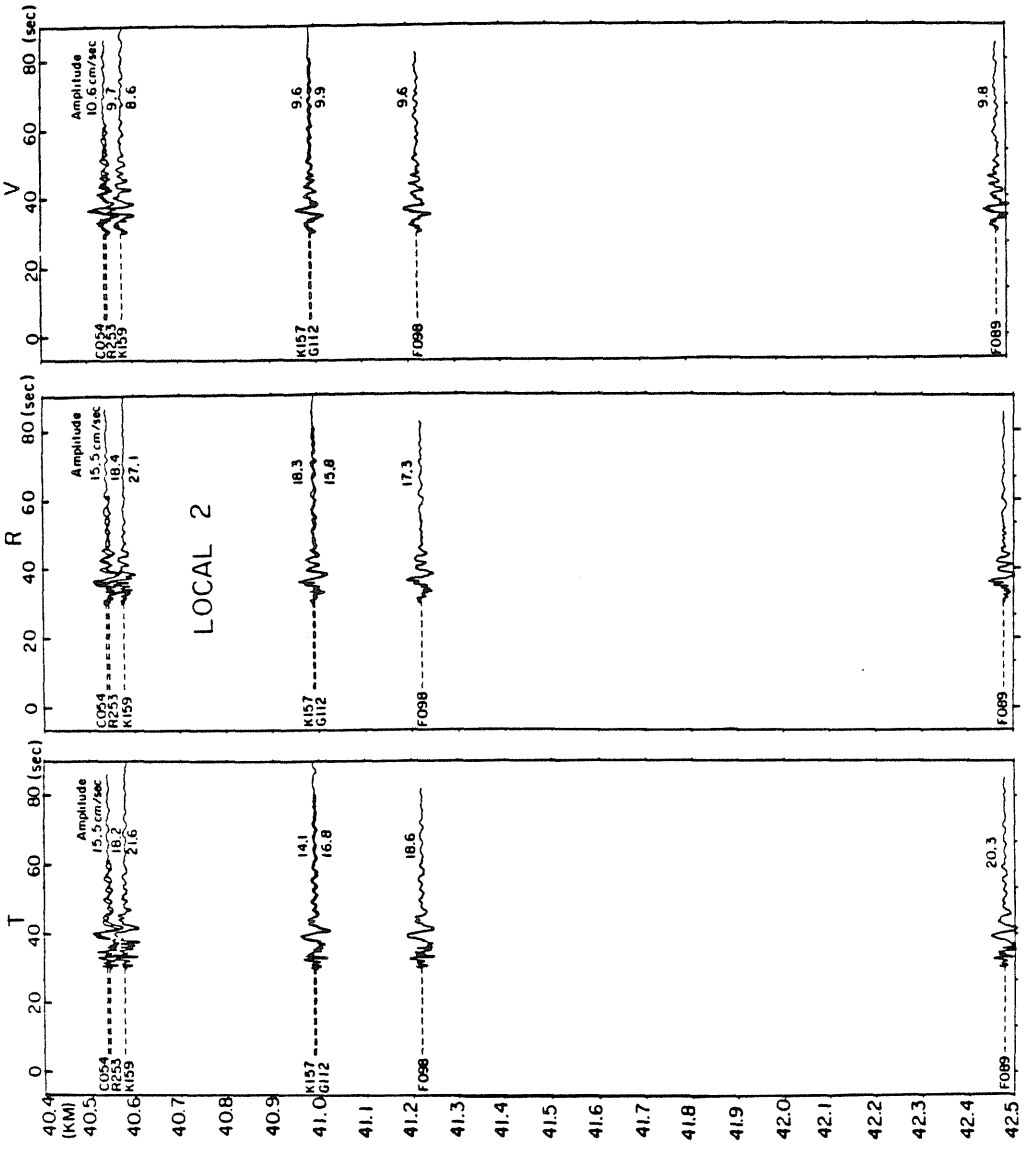

Figure 3-12 Transverse, radial and vertical components of ground velocity in local array-2.

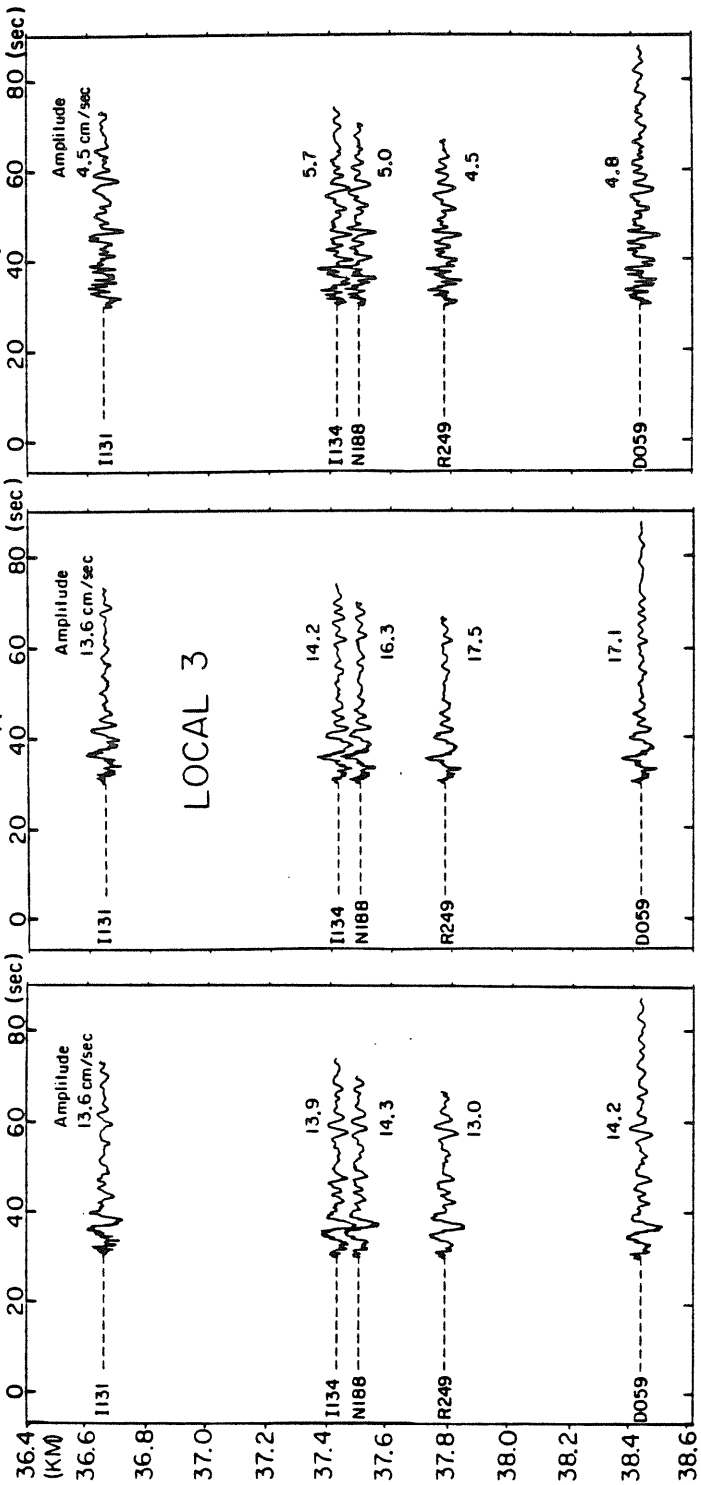

Figure 3-13 Transverse, radial and vertical components of ground velocity in local array-3.

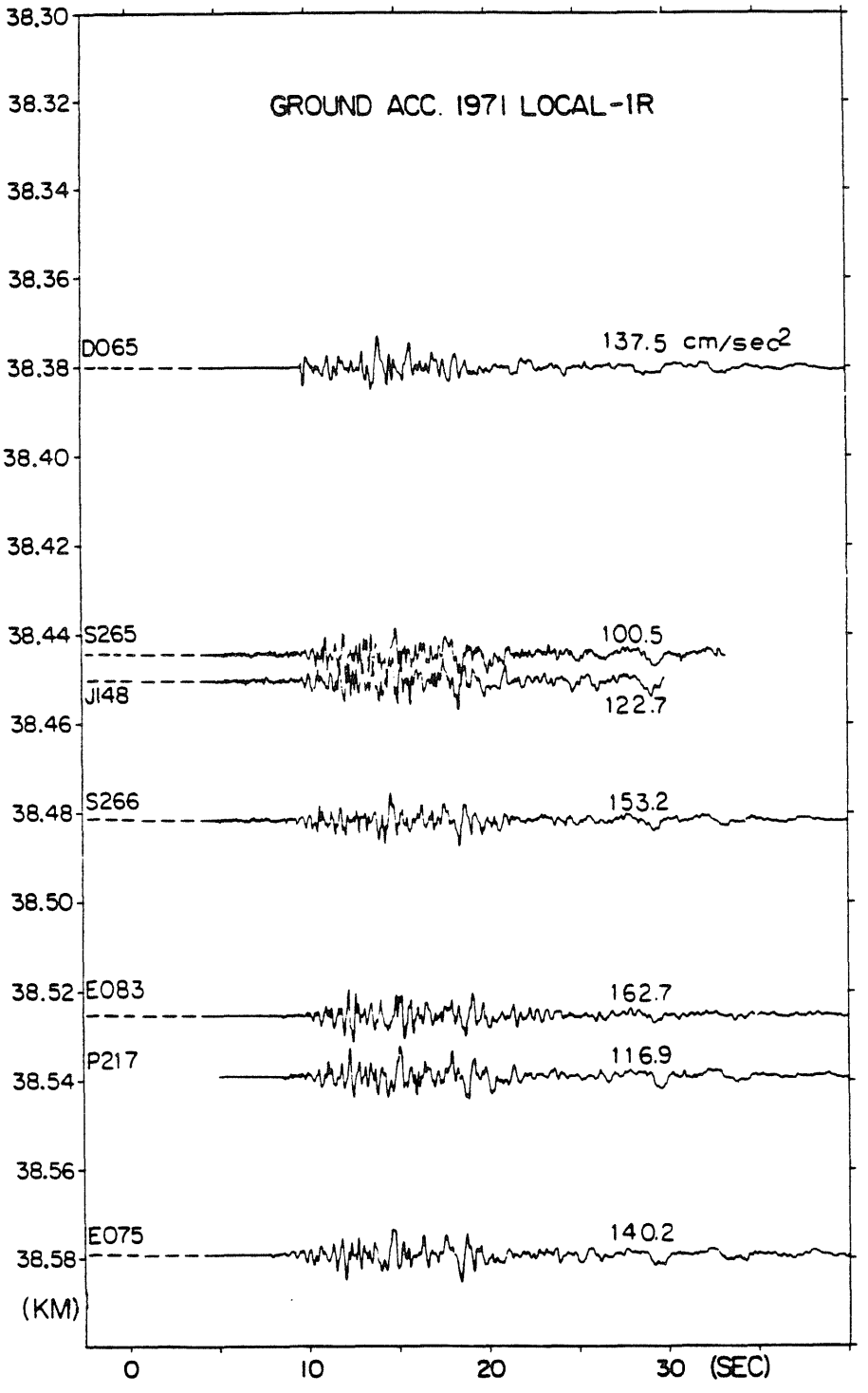

Figure 3-14 The radial component of ground acceleration in local array-1.

shifts could only be detected through very careful analysis.

Simulation by Finite Difference Method

The strong correlation of observed ground motions with geological structure profiles encourages our further investigation of these irregular structure effects. We use the acoustical 2D finite difference method (Brown and Clayton, 1983) to generate synthetic seismograms along both profile I and profile II. The main emphasis here will be on phenomena which occur on waves propagating through these irregular structures from different source depths. We investigate amplitude amplification, signal duration and wave type development.

According to Heaton's (1982) double event solution for the 1971 San Fernando earthquake, there are mainly two areas in which the dislocation is concentrated. One area is near the first hypocenter at a depth of about 13 km and has a maximum dislocation of about 2.5 meters. Another is very near the surface (at depth of about 1 km) along the San Fernando fault with a maximum dislocation of about 3.5 meters, as illustrated in Figure 3-15. In order to study the effect of sources at different depths, we calculated the structure response along each profile for three source depths, namely 1 km , 7km and 13 km. The difference method is applied to the 2D acoustical wave equation

$$\frac{\partial^2 P(x,z)}{\partial t^2} = v^2(x,z)\cdot\nabla^2 P(x,z)$$

, where x,z are the 2D coordinates and $v(x,z)$ is the medium velocity. The normal stress or the pressure $P(x,z)$ is continuous along all boundaries and vanishes on the free surface. The details are described in a paper by Brown and

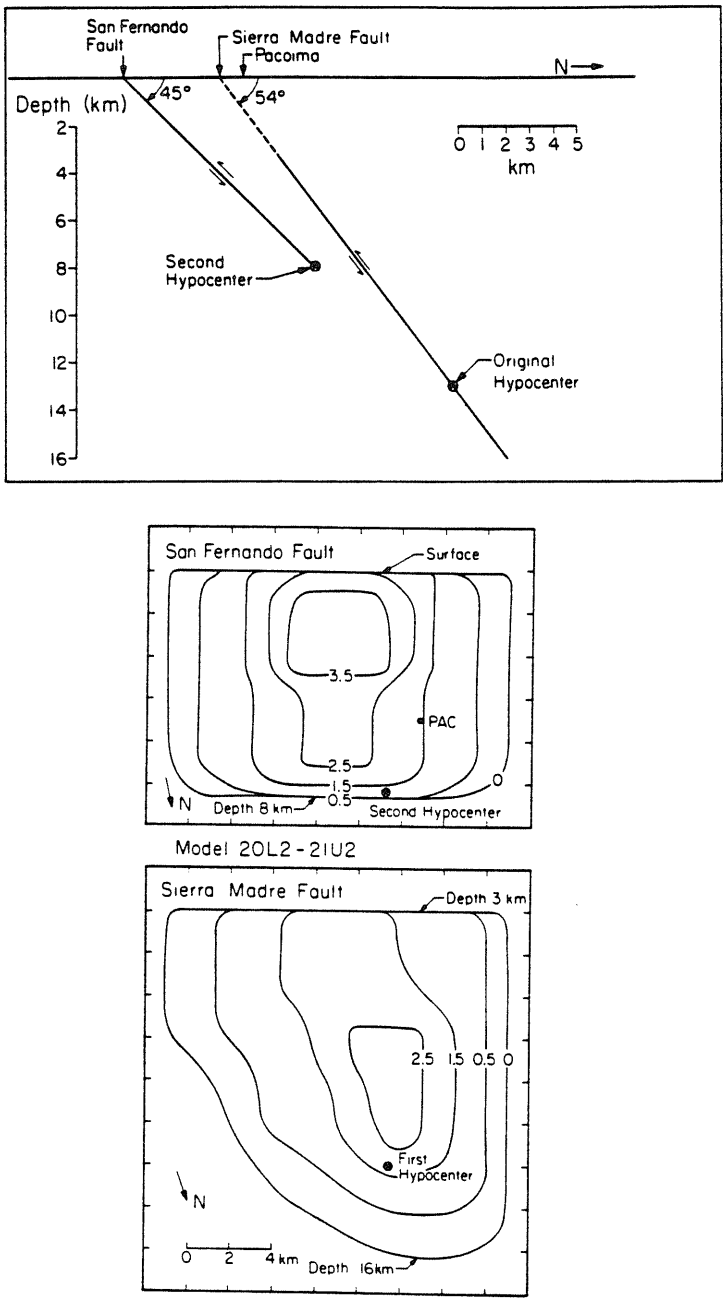

Figure 3-15 The dislocation distribution along the two faults in 1971 San Fernando earthquake determined by the waveform modeling of Heaton (after Heaton, 1982).

Clayton (1983). We used a 0.2 km grid size for both horizontal and vertical ranges, this corresponds to about 10 samples per wavelength at a period of 1 second. Since the maximum velocity in our model is 3.5 km/sec, we chose the difference time step dt to be 0.03 seconds to satisfy the stability criteria,

$$dt < \frac{dh}{\sqrt{2} \cdot v_{max.}}$$

where dh is the grid size. In this way we constrain the time step to be small enough that disturbances do not propagate faster than the maximum velocity within a grid.

a. Irregular Structure along Profile I We approximate earth structure along our profiles as a simple low-velocity (2.1 km/sec) basin embedded within a high-velocity (3.5 km/sec) bedrock half-space, as illustrated in the left of Figure 3-16(a). The source is introduced as an initial condition whereby wave motions in the source region are specified to be the derivative of a Gaussian function. The details can be found in Brown and Clayton (1983). All the profiles are computed assuming a 400x300 grid, which corresponds to dimensions of $80km \times 60km$. Synthetic seismograms computed along profiles 50 km long are shown in Figures 3-16(a), 3-16(b) and 3-16(c) for source depths of 1 km (S3), 7 km (S2) and 13 km (S1), respectively. The total signal duration is 45-second for all the synthetic traces presented in this Chapter. Full scale amplitude is 0.07 for all the profile traces. Thus, waveform amplitudes are comparable for different sources.

Although the synthetics are computed assuming a 2D acoustic line source, the resulting synthetics show good resemblance to the observed ground

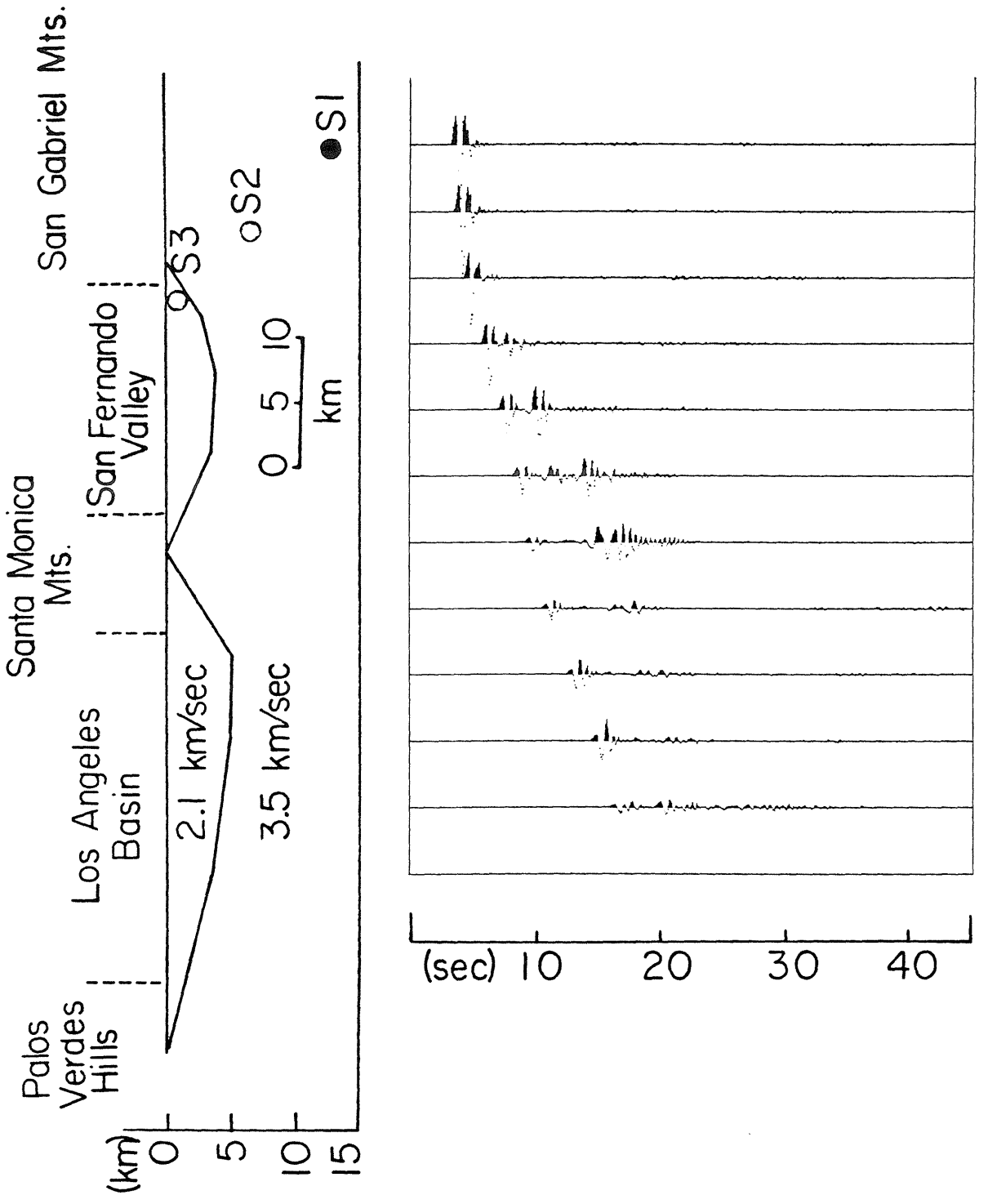

Figure 3-16(a) Synthetic seismograms along the profile I from a source at a depth of 13 km. The full scale amplitude is 0.07 for all the profile traces.

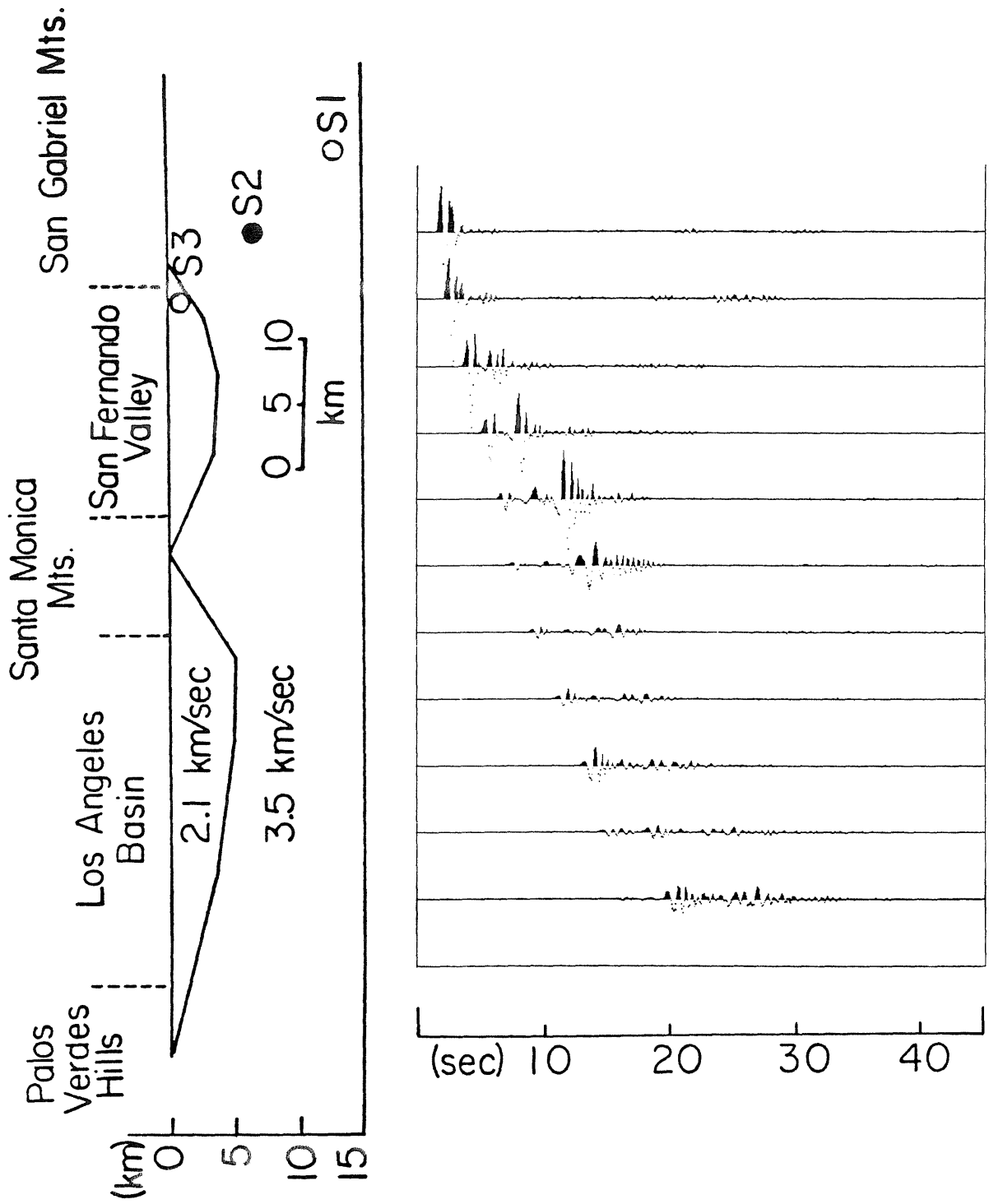

Figure 3-16(b) Synthetic seismograms along profile I from a source at a depth of 7 km.

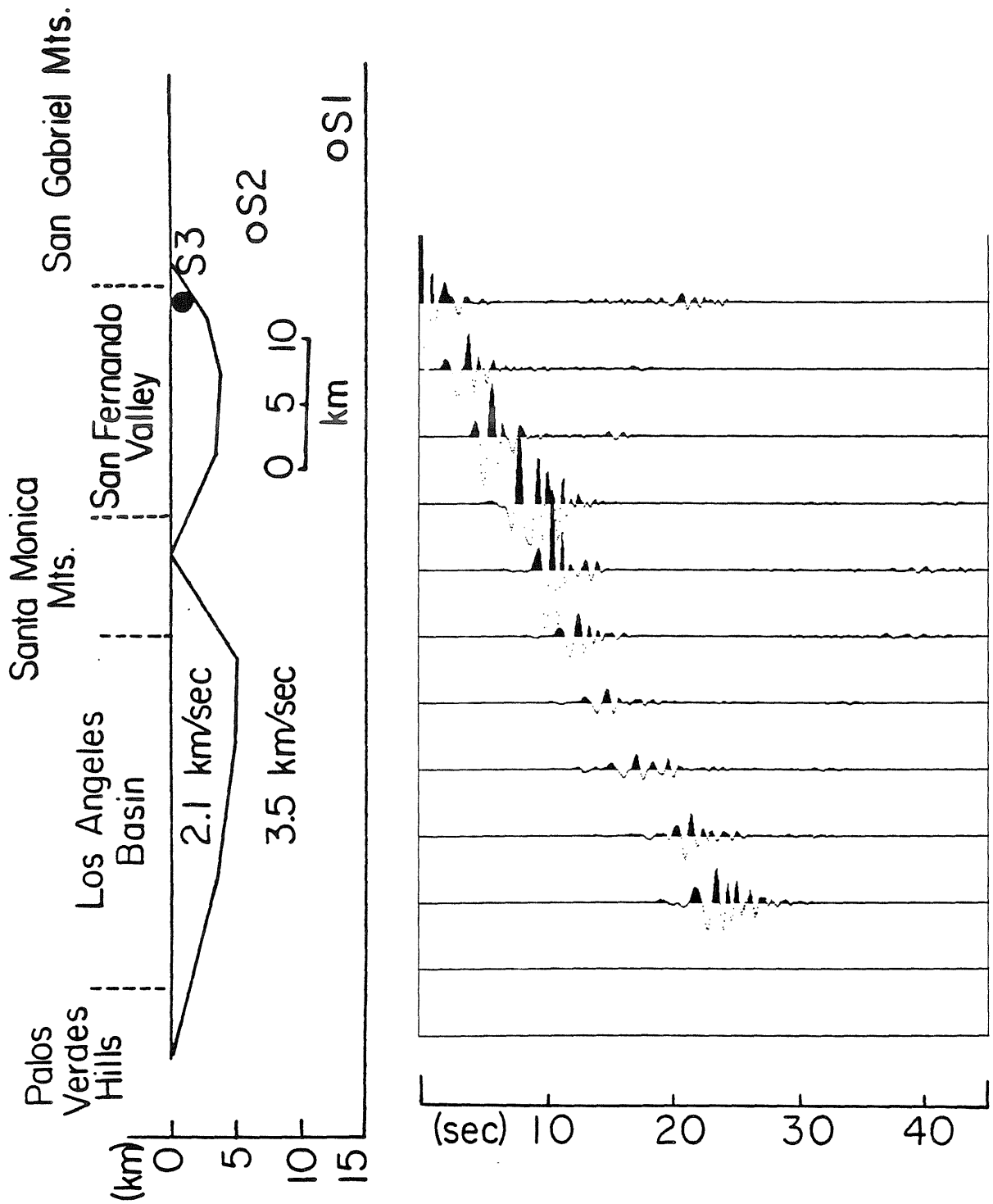

Figure 3-16(c) Synthetic seismograms along profile I from a source at a depth of 1 km.

velocities along profile I. In our model, the San Fernando Basin is an obstacle, creating a shadow for those receiver sites on the Santa Monica Mountains. The strong amplification in the San Fernando Basin can be seen very well for all three source depths. Strong energy focusing is seen near the edge of the basin. This phenomenon is discussed in more detail in Appendix II and is illustrated for a simpler geometry in Figures II-5, II-6 and II-7.

Little energy from the shallow source transmits into the ridge of basement (Santa Monica Mountains), which separates the two low-velocity basins. However, for deeper source (say at 13 km) direct arrivals actually become stronger in the ridge of basement since waves can reach this region from below the basin.

Entering the Los Angeles Basin, we see that surface waves become the dominant arrivals. Wave development here is similar to examples of down-dip wave propagation discussed in Appendix II (see Figures II-1, II-2, and II-3). For the deeper sources, energy reaches the Los Angeles Basin without strong effects from the San Fernando basin. This can be recognized by comparing between the profiles in Figure 3-16(a) and Figure II-3. However, in this range, the interpretation of wave propagating through the ridge from the shallow source is not straightforward. We demonstrate this by comparing the synthetics along two different ridge structures. In Figure 3-17(a), the San Fernando basin is simulated by a simple soft layer with an up-dip thinning edge. The synthetic seismograms suggest that little energy propagates through the basin and into the half-space region beyond. However, when a second basin is added to form a ridge as illustrated in Figure 3-17(b), then surface waves gradually develop in the second basin after passing the ridge area. Thus, the energy leaking through the up-dip edge of the San Fernando basin is trapped again by the down-dip slope in the Los

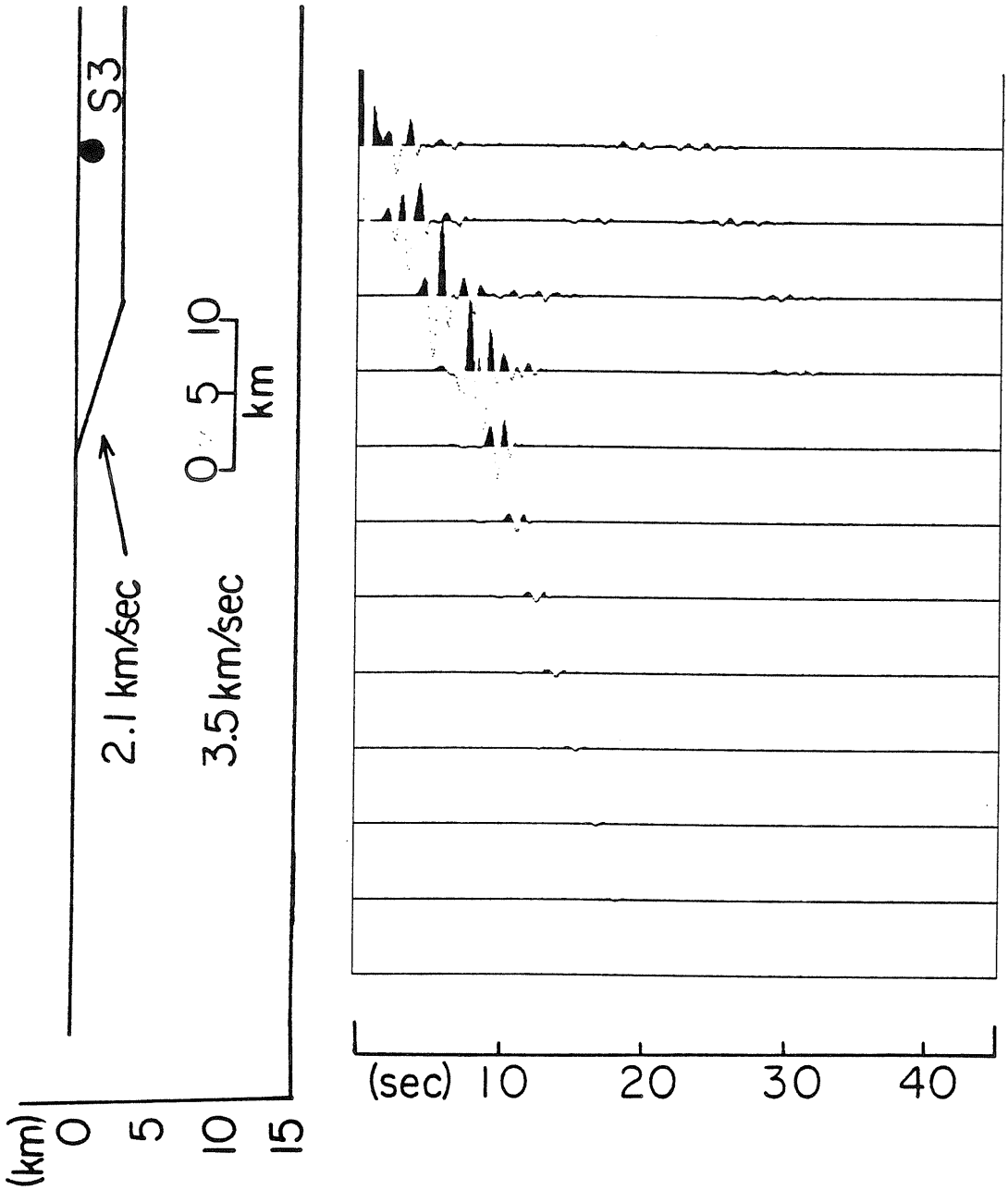

Figure 3-17(a) Ridge structure simulation; up-dip edge of the basin. This illustration shows that little energy can pass the up-dip basin edge and reach the surface receivers. Energy that leaks through the slope propagates mainly toward the half-space.

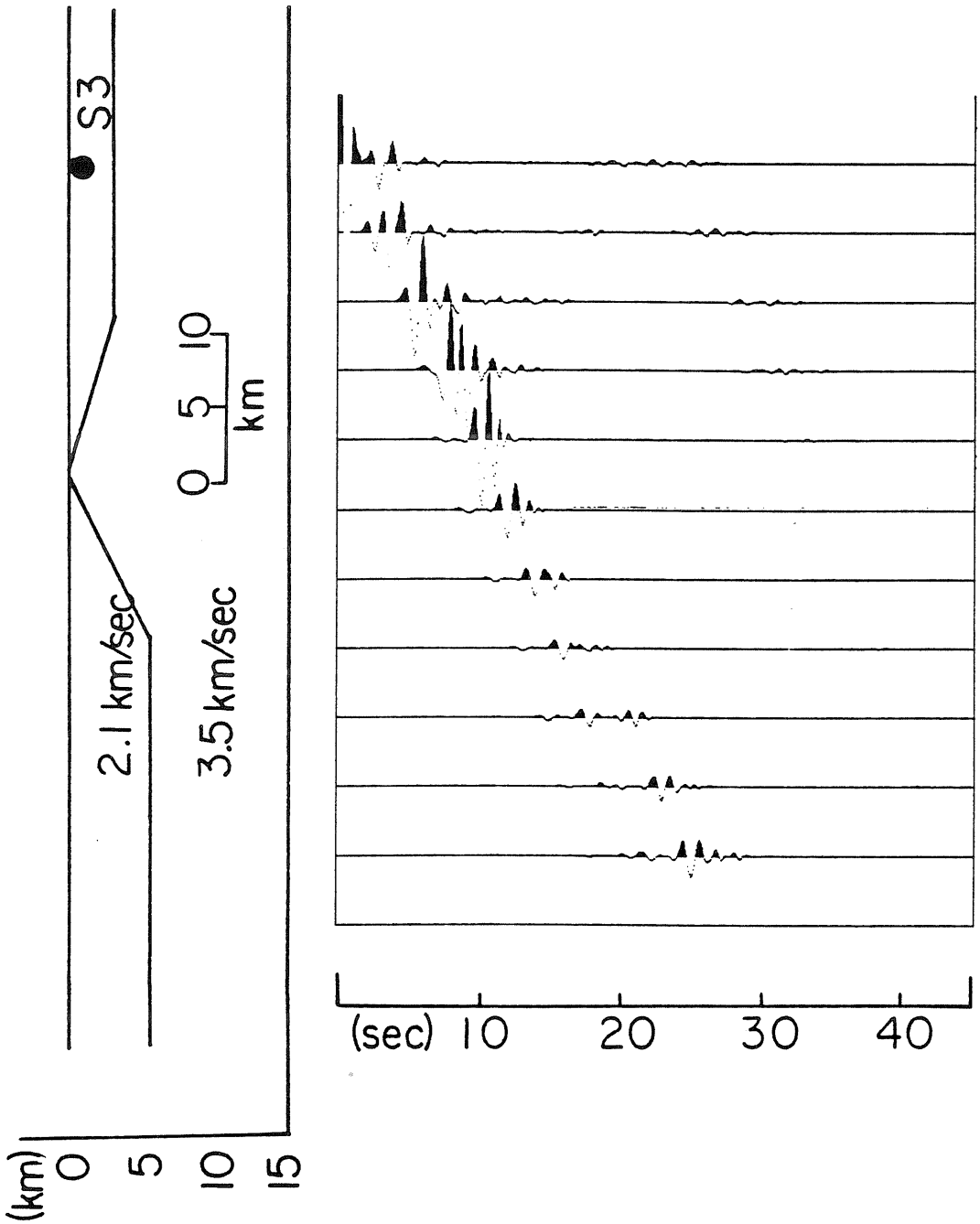

Figure 3-17(b) Ridge structure simulation; formed by both up-dip and down-dip edges of the basins. This ridge is constructed based upon the slopes seen from the San Fernando and Los Angeles basins. After passing the ridge, surface waves are gradually developed from energy trapped by the down-dip edge from Los Angeles basin.

Angeles basin to produce surface waves at further distances. The geometry of the ridge is an important for determining the amount of the energy which is trapped in the second basin.

Assuming Heaton's source model (1982), the rupture delay between source S1 (at 13 km) and S2 (at 7 km) is estimated to be about 4 seconds. Assuming that S1 and S3 (at 1 km) represent areas of the largest dislocations , we can roughly estimate the timing of arrivals and corresponding wave types seen along profile I. The time delay between S3 and S1 due to rupture is about 6 seconds and the corresponding travel time delay is about -4 seconds. Thus we concluded that the S! phases observed along profile I are mainly derived from S1 (13 km source). The strong later arriving waves seen near the Santa Monica Mountains are surface waves from both S1 (deep source) and S3 (shallow source). For the three stations in the San Fernando Basin, C048, J145 and H115, the high amplitude waves seen in the velocity waveforms are combinations of surface waves from both deep and shallow sources and body waves from the shallow source. Thus, the reason that the S! phase maintains strong coherence along this structurally complex path is that S! is derived mainly from the deeper part of the rupture. The S! travel path from deeper sources is affected relatively little by the presence of local basins.

b. Irregular Structure along Profile II Ground motions observed along profile II show very different features from those observed along profile I. Again, we generate synthetic seismograms along the profile II for three source depths, namely 1 km (source S3), 7km (source S2), and 13 km (source S1). The results are illustrated in Figures 3-18(a), 3-18(b) and 3-18(c), respectively. Since the wave path is more or less following the northeastern boundary of the

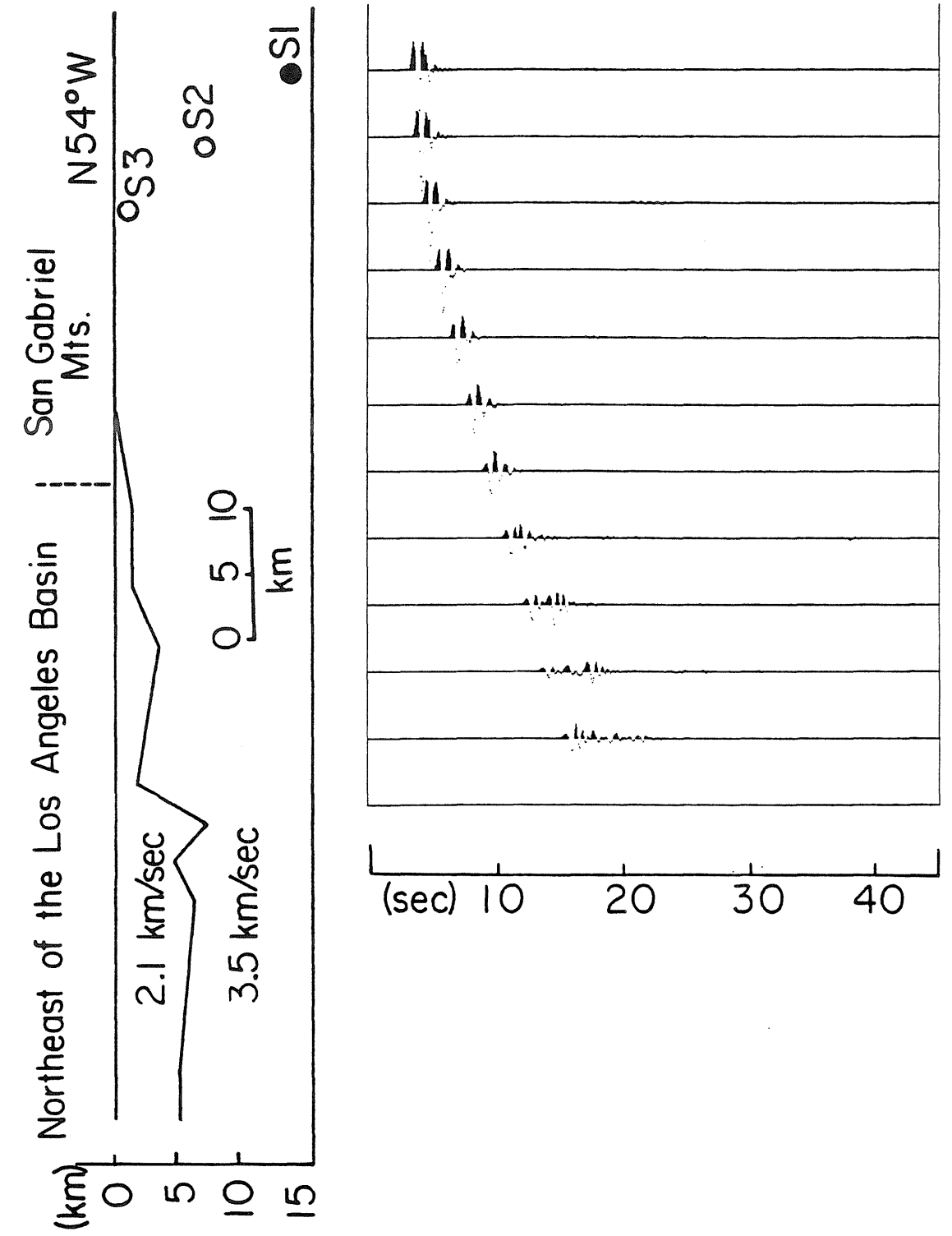

Figure 3-18(a) Synthetic seismograms along profile II from a source at a depth of 13 km.

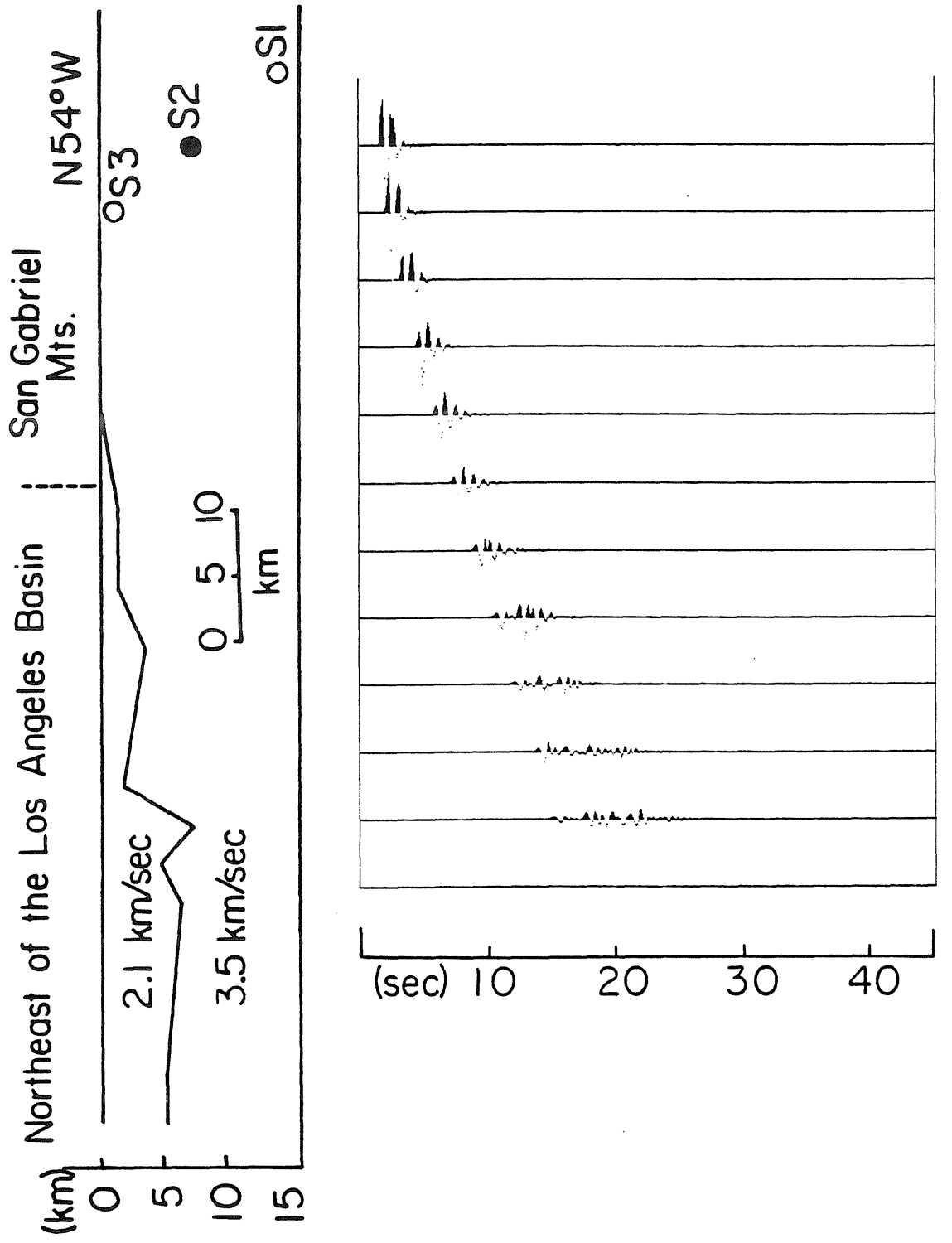

Figure 3-18(b) Synthetic seismograms along profile II from a source at a depth of 7 km.

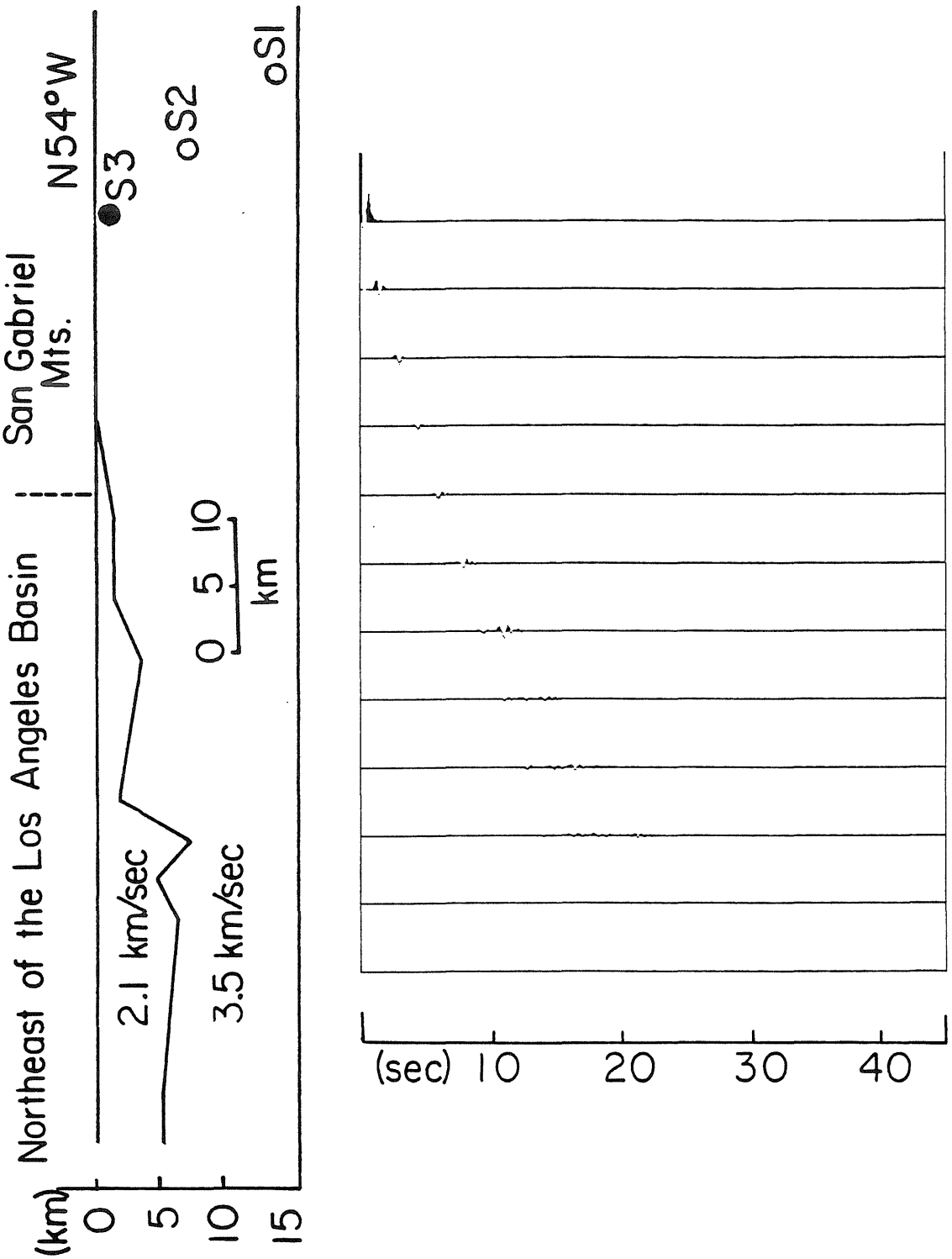

Figure 3-18(c) Synthetic seismograms along profile II from a source at a depth of 1 km.

Los Angeles Basin, the wave development is quite different from that seen along profile I. We approximate the structure along this profile as a basin (shear velocity of 2.1 km/sec) embedded in a half-sapce (3.5 km/sec), as illustrated in the left of Figure 3-18(a). In spite of this rather simplified structure model , the synthetics compare well with the motions observed along profile II (Figure 3-5).

As was the case for profile I, that the S! phase is primarily composed of direct S-wave arrivals from S1 (source at 13 km). In our synthetics, surface waves are gradually developed after distance of about 40 km, which agrees well with the observations. According to our 2D modeling, the shallow source (S3) contributes little to ground motions observed along this path. Because the structure in the source region is approximated by a half-space, little energy from the shallow source is trapped within the basin.

Discussions and Conclusions

Velocity profiles recorded from the 1971 San Fernando earthquake demonstrate strong path effects due to topography of the basement surfaces. The different waveform pattern observed along three long profiles implies that valley or basin structures can produce significant reverberation and amplification effects. It is suggested that the proper geometry of basins and earthquake sources needs to be considered in order to predict waveforms along these wave paths.

Velocity profiles along three local arrays in the Los Angles basin suggests that, within 3 km in range, the waveforms are almost identical. It is also suggested that higher frequency waves, as represented by ground accelerations,

are less affected by these large scale basin structures.

Profiles of displacement traces, which are not shown in this study, display characteristics similar to those observed in the velocity profiles. That is, the waveforms show good correlation with variations in the basement surfaces. However, due to its high-frequency nature, the S! phase is more easily recognized in velocity records than in displacement records.

Along profile III, displacements have relatively simple waveform. This is consistent with our understanding of the basement surface along profile II, since a half-space seems to be an adequate approximation for the propagating path. We speculate that only deeper sources effectively transmit short-period energy along this profile as suggested in Figures 3-18(a) through 3-18(c). This is probably the main reason that the duration of high-frequency motion is rather short for all the stations recorded along this azimuth.

We use the 2D finite difference method to compute synthetic seismograms for irregular structures which exist along profile I and profile II. Although the structure used in the calculation is rather simplified and the numerical code is for acoustical media, the general features of the synthetics agree quite well with the observed ground motions. We approximate Heaton's (1982) source model, which has two major areas of dislocation by point sources , at depths of 13 km and 1 km. Using the relative timing, amplitude and signal duration of major arrivals observed in the ground motions along both profile I and profile II, we suggest that the coherent S! phase (the S waves) is primarily from the first source, at 13 km. The shallow source (near 1 km) contributes little to the stations along the profile II. However, it does produce strong surface waves for the stations in the San Fernando Basin region and also contributes to the generation

of surface waves in the Los Angeles Basin. This study suggests that the observed ground motions are indeed affected strongly by propagation paths along different structural provinces.

References

Abdel-Ghaffar A. M. and R. F. Scott (1978), An investigation of the dynamic characteristics of an earth dam, REPORT NO. EERL 78-02, California Institute of Technology

Aki K. (1968), Seismic displacements near a fault, J. of Geoph. Res., 73, 5359-5376.

Aki K. (1979), Characterization of barriers on an earthquake fault, J. of Geoph. Res., 84, 6140-6148.

Allen, C. R., T. C. Hanks, J. H. Whitcomb (1973), San Fernando earthquake: Seismological studies and their implications in San Fernando California Earthquake of February 9, 1971, Vol. I, Geological & Geophysical Studies, U. S. Government Printing Office, Washington, D. C.

Anderson J. G. and T. H. Heaton (1979), Aftershock accelerograms recorded on a temporary array, U. S. Professional Paper.

Angstman B. G., P. K. P. Spudich and J. Fletcher (1979), The Coyote Lake earthquake : 0.42 G acceleration from an S-P converted phase, Trans. Am. Geoph. Un., 60, No. 46, S 121.

Archuleta, R. (1979), Rupture propagation effects in the Coyote Lake earthquake, EOS, 60, No. 46, Nov. 13, S 122.

Archuleta, R. J. and S. M. Day (1980), Dynamic Rupture in a layered medium: The 1966 Parkfield earthquake, 70, 671-689.

Boore, D. M., W. B. Joyner, A. A. Oliver, III and R. A. Page (1980), Peak acceleration, velocity and displacement from strong-motion records, Bull. Seis. Soc. Am., 70, 305-321.

Boore, D. M. and M. D. Zoback (1974), Near-field motions from kinematic models of propagating faults, Bull. Seis. Soc. Am., 64, 321-342.

Bouchon M. and K. Aki (1979), Predictability of ground displacement and

velocity near an earthquake fault: An example: The Parkfield earthquake of 1966, J. of Geoph. Res., 84, 6149-6156.

Bouchon, M. (1982), The rupture mechanism of the Coyote Lake earthquake of 6 August 1979 inferred from near-field data, Bull. Seism. Soc. Am., 72, 745-757.

Brady, A. G., P. N. Mork, V. Perez and L. Porter (1979), Processed data from the Gilroy array and Coyote Creek records, Coyote Lake, California earthquake 6 August 1979, USGS OPEN-FILE REPORT, 81-42.

Brady, A. G., V. Perez and P. N. Mork (1980), The Imperial Valley earthquake, October 15, 1979, digitization and processing of accelerograph records, USGS OPEN-FILE REPORT, 80-703.

Brady, A. G. and R. L. Porcella (1982), Imperial Valley aftershocks during the first 24 hours; A discussion of the strong-motion records (in press).

Brown, D. and R. Clayton (1983), Difference approximations for forward modeling problems (in preparation).

Burdick, L. J. and C. A. Langston (1977), Modeling crustal structure through the use of converted phases in teleseismic body-wave forms, Bull. Seism. Soc. Am., 67, 677-691.

Carpenter, E. W. (1967), Teleseismic signals calculated for underground, underwater, and atmospheric explosion, Geophysics, 32, 17-32.

Duke, C. M. and A. M. Mal (1978), Site and source effects on earthquake ground motion, NSF GRANT REPORT G144056, UCLA.

Eaton, J. P., M. E. O'neill and J. M. Murdock (1970), Aftershocks of the 1966 Parkfield Cholame, California earthquake: A detailed study, Bull. Seis. Soc. Am., 60, 1151-1197.

EERL, Caltech (1974), Strong Motion Earthquake Accelerrgrams, Vol. II, Report from Earthquake Engineering Research Laboratory, California Institute of Technology.

Fuis G. S., W. D. Mooney, J. H. Healy and G.A. McMechan and W. J. Lutter (1981),

Crustal structure of the Imperial Valley region, USGS OPEN-FILE REPORT.

Hadley, D. M., D. V. Helmberger and J. A. Orcutt (1982), Peak acceleration scaling studies, Bull. Seis. Soc. Am., 72, 959-979.

Hanks, T. C. (1975), Strong ground motion of the San Fernando, California earthquake: Ground displacements, Bull. Seism. Soc. Am., Vol. 65, No. 1, 193-225.

Hartzell, S. T. (1978), Interpretation of earthquake strong ground motion and implications for earthquake mechanism, Ph.D. Dissertation, U. C. San Diego, 115-119.

Hartzell, S. T. (1980), Faulting process of the May 17, 1976 Gazli, USSR earthquake, Bull. Seism. Soc. Am., 70, 1715-1736.

Hartzell, S. T. and D. V. Helmberger (1982), Strong-motion modeling of the Imperial Valley earthquake of 1979, Bull. Seis. Soc. Am., 72, 571.

Heaton, T. H. and D. V. Helmberger (1978), Predictability of strong ground motion in the Imperial Valley: Modeling the M_L 4.9, November 4, 1976 Brawley earthquake, Bull. Seism. Soc. Am., 68, 31-48.

Heaton T. H. and D. V. Helmberger (1979), Generalized ray models of the San Fernando earthquake, Bull. Seis. soc. Am., 1131-1341.

Heaton, T. H. (1982), The 1971 San Fernando earthquake: A double event?, Bull. Seis. Soc. Am., 2037-2062.

Helmberger, D. G. and G. Engen (1980), Modeling the long-period body waves from shallow earthquakes at regional ranges, Bull. Seism. Soc. Am., 70, 5, 1699-1714.

Helmberger, D. V., G. Engen and P. Scott (1979), A note on velocity density and attenuation models for marine sediments, J. Geoph. Res., 84, 667-671.

Helmberger, D. G. adn D. G. Harkrider (1978), Modeling earthquakes with generalized ray theory, Proceedings of IUTAM Symposium: Modern Problems In Elastic Wave Propagation, published by John Wiley & Sons, Inc., 499-518.

Herd, D. G., R. J. Mclaughlin, A. M. Sarna-Wojcicki, M. M. Clark, W. H. K. Lee, R. V. Sharp, D. H. Sorg, W. D. Stuart, P. W. Harsh and R. K. Mark (1979), Surface faulting accompanying the August 6, 1979 Coyote Lake earthquake, EOS, 60, No. 46, 890.

Langston, C. A and D. V. Helmberger (1975), A procedure for modeling shallow dislocation source, Geophs. J. Res. Astron. Soc., 42, 117-130.

Le Bras, R. (1982), An inversion algorithm for strong ground motion data application to the 1979 Imperial Valley earthquake (in preparation).

Lee, W., D. Herd, V. Cagnetti, W. Bakun and A. Rapport(1979), A preliminary study of the Coyote Lake earthquake of August 6, 1979 and its major aftershocks, USGS OPEN-FILE REPORT 79-1621.

Lindh, A. G. and D. M. Boore (1981), Control of rupture by fault geometry during the 1966 Parkfield earthquake, Bull. Seism. Soc. Am., 71, 95-116.

Lindh A. G., D. M. Boore, P. Mutch and D. Reneau (1982), future studies on the 1966 Parkfield earthquake (in press).

Johnson, C. E. and L. K. Hutton (1981), Aftershocks and prior seismicity of the 1979 Imperial Valley earthquake, U. S. Geological Survey open-file report, Menlo Park.

Joyner, W. B., R. E. Warrick and T. E. Fumal (1981), The effect of Quaternary alluvium on strong-ground motion in the Coyote Lake, California earthquake of 1979, Bull. Seis. Soc. Am., 71, 4, 1333.

Madariaga, R. (1977), High-frequency radiation from crack (stress drop) models of earthquake faulting, Geophys. J. Res. Astro. Soc., 51, 625-651.

Mellman, G. R. and D. V. Helmberger (1974), High-frequency attenuation by a thin high-velocity layer, Bull. Seism. Soc. Am., 64, 1383-1388.

Mellman, G. R. (1978), A method for waveform inversion of body-wave seismograms, Ph.D. Thesis, California Institute of Technology, Pasadena.

Nabelek, J. (1982), Teleseismic constraints on the 1979 Coyote Lake and 1981 El

Asnam earthquake (in press).

Olson, A. H. (1982), The discrete wavenumber/finite element method for synthetic seismograms, Part I, Ph.D. Thesis, U. C. San Diego.

Rial, J. A. and P. Scott (1983), Ray path effects in strong motion seismology: Caustics and focusing by sedimentary basins (in preparation).

Trifunac, M. D. (1974), A three dimensional dislocation model for the San Fernando, California earthquake of February 9, 1971, Bull. Seis. Soc. Am., 64, 149-172.

Trifunac, M. D. and F. E. Udwadia (1974), Parkfield, California earthquke of June 27, 1966: A three dimensional moving dislocation, Bull. Seism. Soc. Am., 64 , 511-533.

Trifunac, M. D. (1976), Preliminary analysis of the peaks of strong ground motion; Dependence of peaks on earthquake magnitude, epicentral distance, and recording site conditions, Bull. Seism. Soc. Am., 66, 189-219.

Uhrhammer, R. (1980), Observations of the Coyote Lake, California earthquake sequence of August 6, 1979, Bull. Seism. Soc. Am., 70, 559-570.

Wallace, T., D. V. Helmberger and G. Mellman (1981), A technique for the inversion of regional data in source parameter studies, J. Geophs. Res., 86, 1679-1685.

Yerkes, R. F., T. H. McCulloh, J. E. Schoellhammer and J. G. Vedder (1965), Geology of the Los Angeles Basin California-- An introduction, Geological Survey Professional Paper 420-A.

Appendix I Inversion Method

In order to include the amplitude information in the inversion procedure, we define the error e_i for each seismogram i as

$$e_i = \int_0^T \left[f_i(t) - g_i(t) \right]^2 dt \tag{1}$$

where $f_i(t)$ represents the observed data trace, $g_i(t)$ is the synthetic seismogram generated from starting model parameters, and T is the time segment used in inversion procedure.

The inversion scheme is similar to the waveform inversion method of Le Bras (1982), Wallace et al. (1981) and Mellman (1978). The optimal solution is obtained by changing the model parameters which minimizes the sum of the square of the error function. This can be expressed as

$$\varepsilon^2 = \sum_{j=1}^{N} e_j^2 \tag{2}$$

where N is the total available data traces. For an initial model m_o and the corresponding error e_j^o, the model change δm, which minimizes the sum of the square error $\varepsilon^{o\,2}$ can be written as

$$\varepsilon_j^{o\,2}(\delta m) = \left[e_j^o + \delta e_j \right] \left[e_j^o + \delta e_j \right] \tag{3}$$

and

$$\delta e_j = \frac{\partial e_j}{\partial \theta_k} \delta \theta_k \tag{4}$$

where θ_k are the source parameters, including the seismic moment, strike, rake and dip for each source element.

Following (3), the error functions and the partials can also be expressed in a matrix form as,

$$\varepsilon^2(\delta m) = \left[e + A\varphi\right]^T \left[e + A\varphi\right] \tag{5}$$

where A is an $N \times M$ matrix with elements

$$a_{ij} = \frac{\partial e_i}{\partial \theta_j} ,$$

M is the number of source parameters, and φ is the matrix of the variation of source parameters, $\delta \theta_k$. Calculating the variation of $\delta\varphi$ and setting to zero, we have

$$\varphi = (A^T A)^{-1} A^T e \tag{6}$$

where -1 represents the generalized inverse and superscript T denotes the transpose. Thus, the model variation φ can be obtained from the partial matrix A and the error function e. In order to stabilize the inversion scheme, an extra damping term is added, thus the final equation used for inversion is

$$\varphi = \left[A^T A + \sigma I\right]^{-1} A^T e \tag{7}$$

where σ is the damping coefficient and I is the unit matrix.

In the following, a brief summary of expressing the synthetic seismograms in terms of the dislocation source model will be described. The displacements in cylindrical coordinate can be expressed as

$$w(r,z,\theta,t) = \frac{M_o}{4\pi\rho}\left\{\dot{D}(t)*\sum_{i=1}^{3} W_i(t)A_i\right\} \tag{8}$$

$$q(r,z,\theta,t) = \frac{M_o}{4\pi\rho}\left\{\dot{D}(t)*\sum_{i=1}^{3} Q_i(t)A_i\right\} \tag{9}$$

$$v(r,z,\theta,t) = \frac{M_o}{4\pi\rho}\left\{\dot{D}(t)*\sum_{i=1}^{2} V_i(t)A_{i+3}\right\} \tag{10}$$

where $\dot{D}(t)$ is the source time function, M_o is the seismic moment, and W_i, Q_i and V_i are the step responses for radial, vertical and transverse components, respectively. The orientation constants A_i are given by :

$$\begin{aligned}
A_1(\theta,\lambda,\delta) &= \sin 2\theta\cos\lambda\sin\delta + \tfrac{1}{2}\cos 2\theta\sin\lambda\sin 2\delta \\
A_2(\theta,\lambda,\delta) &= \cos\theta\cos\lambda\cos\delta - \sin\theta\sin\lambda\cos 2\delta \\
A_3(\theta,\lambda,\delta) &= \tfrac{1}{2}\sin\lambda\sin 2\delta \\
A_4(\theta,\lambda,\delta) &= \cos 2\theta\cos\lambda\sin\delta - \tfrac{1}{2}\sin 2\theta\sin\lambda\sin 2\delta \\
A_5(\theta,\lambda,\delta) &= -\sin\theta\cos\lambda\cos\delta - \cos\theta\sin\lambda\cos 2\delta
\end{aligned} \tag{11}$$

where θ is the strike, λ is the rake and δ is the dip angle.

For the application in Chapter 2-B, several source elements or fault segments can be inverted simultaneously. Thus, the synthetic seismogram, $g_i(t)$ is simply the sum of the contribution from all the fault elements and can be

expressed as

$$g_i(t) = \sum_{j=1}^{L} d_j \cdot \bar{g}_{ij}(t) \tag{12}$$

where d_j is the scaling factor and is proportional to the moment of the source element j, and $\bar{g}_{ij}(t)$ is the unit moment contribution at station i from source element j.

Combining equations (1) and (12), the error function e_i then can be expressed as

$$e_i = \int f_i^2 - \sum_{j=1}^{L} 2d_j \cdot \int f_i \bar{g}_{ij} + \sum_{l=1}^{L}\sum_{j=1}^{L} d_j d_l \cdot \int \bar{g}_{ij} \cdot \bar{g}_{il}. \tag{13}$$

where $\bar{g}_{ij}$ can be one of (8), (9) or (10), which relate directly to the model parameters, θ_j, δ_j and λ_j. Thus the partials can be obtained by taking derivatives with respect to d_j, θ_j, δ_j and λ_j in equation (13).

Appendix II Difference Synthetic Seismograms for Dipping Structures

The irregular polygonal structure used for numerical simulation of profiles I and II in Chapter 3 are constructed from several down-dip and up-dip boundary segments of various dip angles. In order to gain some physical insights into wave propagation along these irregular structures, in this appendix, we investigate ground motions produced by dipping structure.

The difference method described in Chapter 3 is used to generate both down-dip and up-dip structure responses for three interested source depths, namely 1 km (source S3), 7km (source S2) and 13 km (source S1). The slope we use for both down-dip and up-dip cases is 0.1 radian (5.7 degrees), which is rather gentle compared to that appearing in either profile I or profile II.

Figures II-1, II-2 and II-3 show the down-dip synthetic profiles for source depths of 1 km, 7km and 13 km, respectively. The velocity structure is also illustrated in the left of each figure. The down-dip structure shows the tendency to trap energy in the low velocity layer as pointed out by Hong and Helmberger (1979), who constructed similar models using the generalized ray technique. This feature is especially evident for those multiples derived from the deepest source (13 km) as shown in Figure II-3. In Figure II-4, we show the synthetic profile for a shallow source (1 km) recorded at receiver sites at depths of 10 km to demonstrate that energy leaks through this dipping structure into the half space below.

The up-dip structure profiles for the same source depths (1 km, 7 km and 13 km) are shown in Figures II-5, II-6 and II-7, respectively. Since both shallower sources (1 km and 7 km) are situated in the low velocity layer, ground motion amplitudes are quite high, even at large distances. For the deepest source (13 km, see Figure II-7), we see that the up-dip structure does not trap energy as effectively as the down-dip structure shown in Figure II-3. Figure II-8 shows the synthetic profile for a source at 1 km and receivers at depths of 10 km. The multiples in the up-dip structure leak severely when compared to the down-dip structure as illustrated in Figures II-8 and II-4.

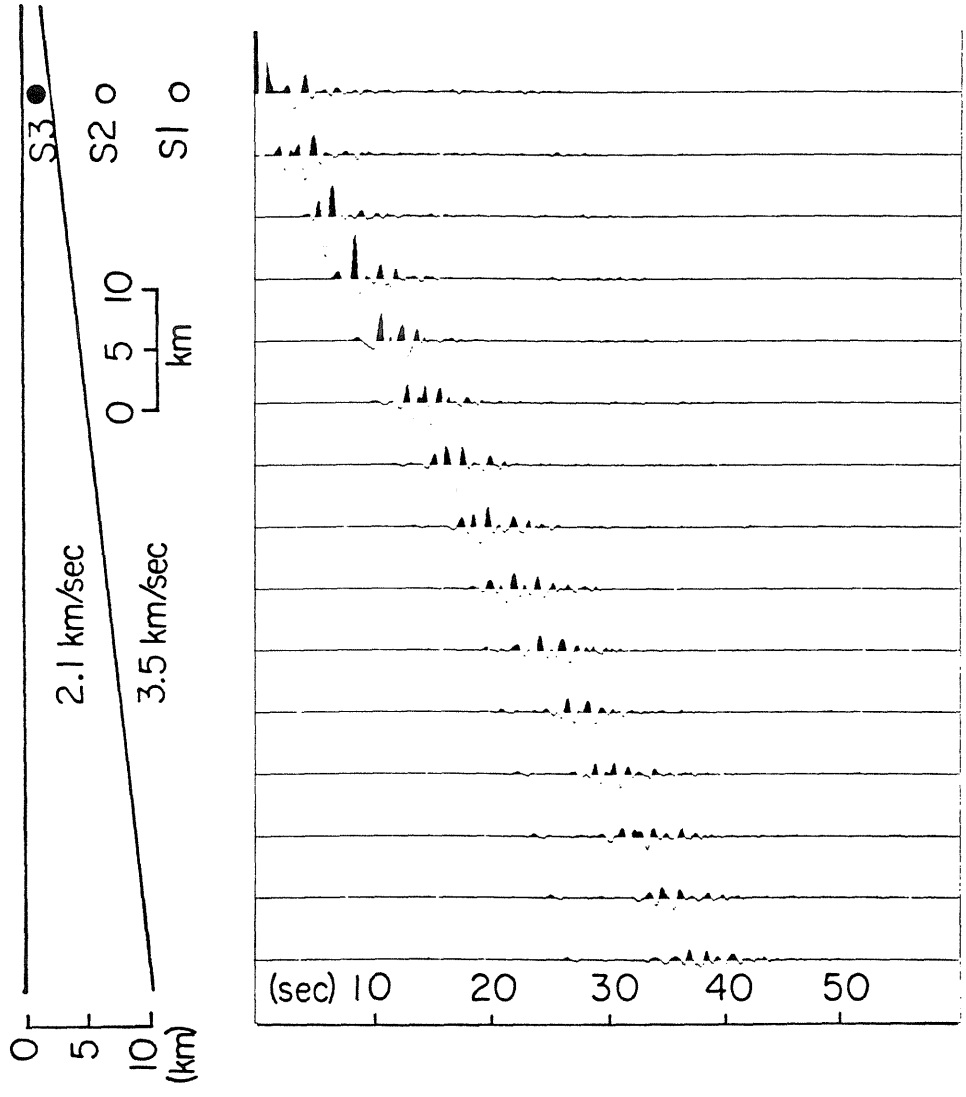

Figure II-1 Synthetic seismograms computed by the difference method for the structure shown in the left. The source depth is 1 km (S3) and the receivers are on the surface. The traces are plotted for every 5 km in distance. The total signal length is 60 seconds and the full scale amplitude is 0.07 for all the figures shown in this Appendix.

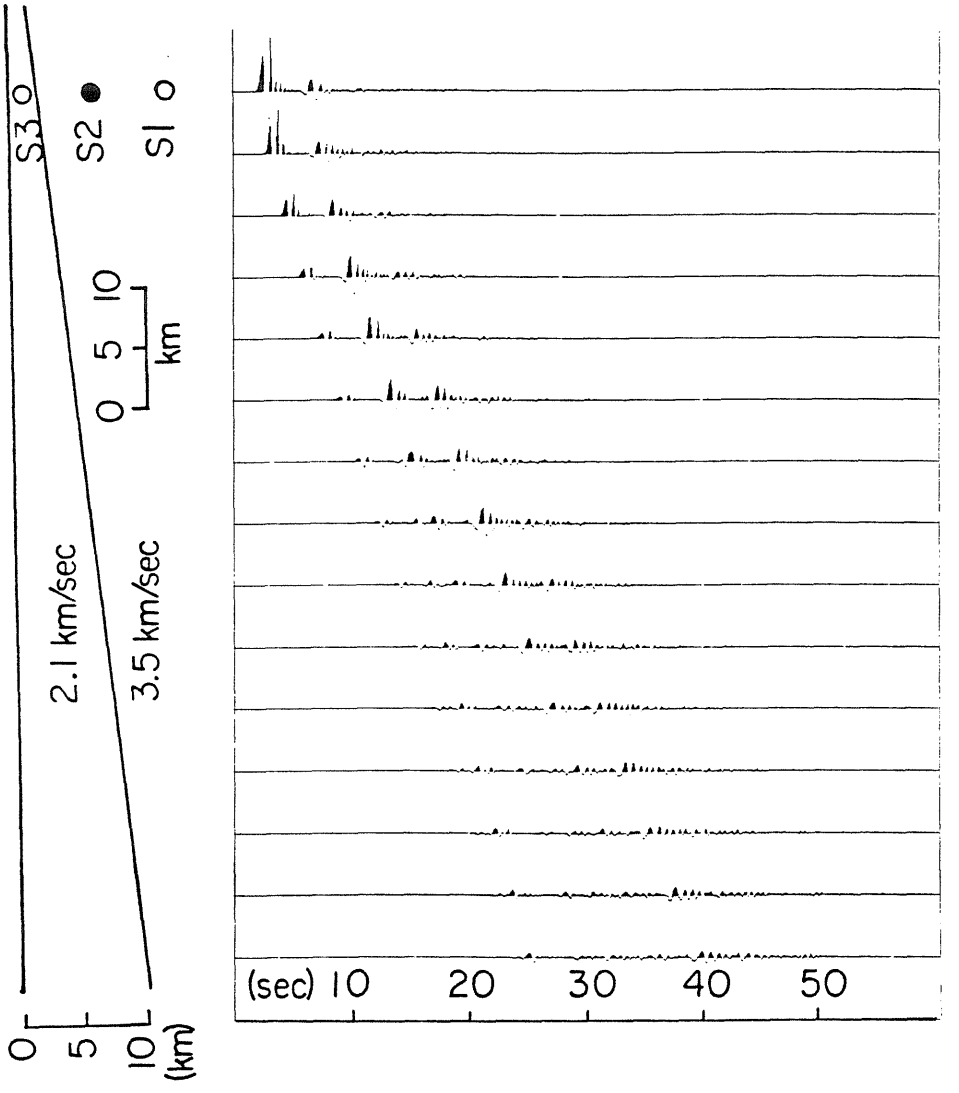

Figure II-2 Synthetic seismograms from source S2 (depth=7 km) for surface receivers.

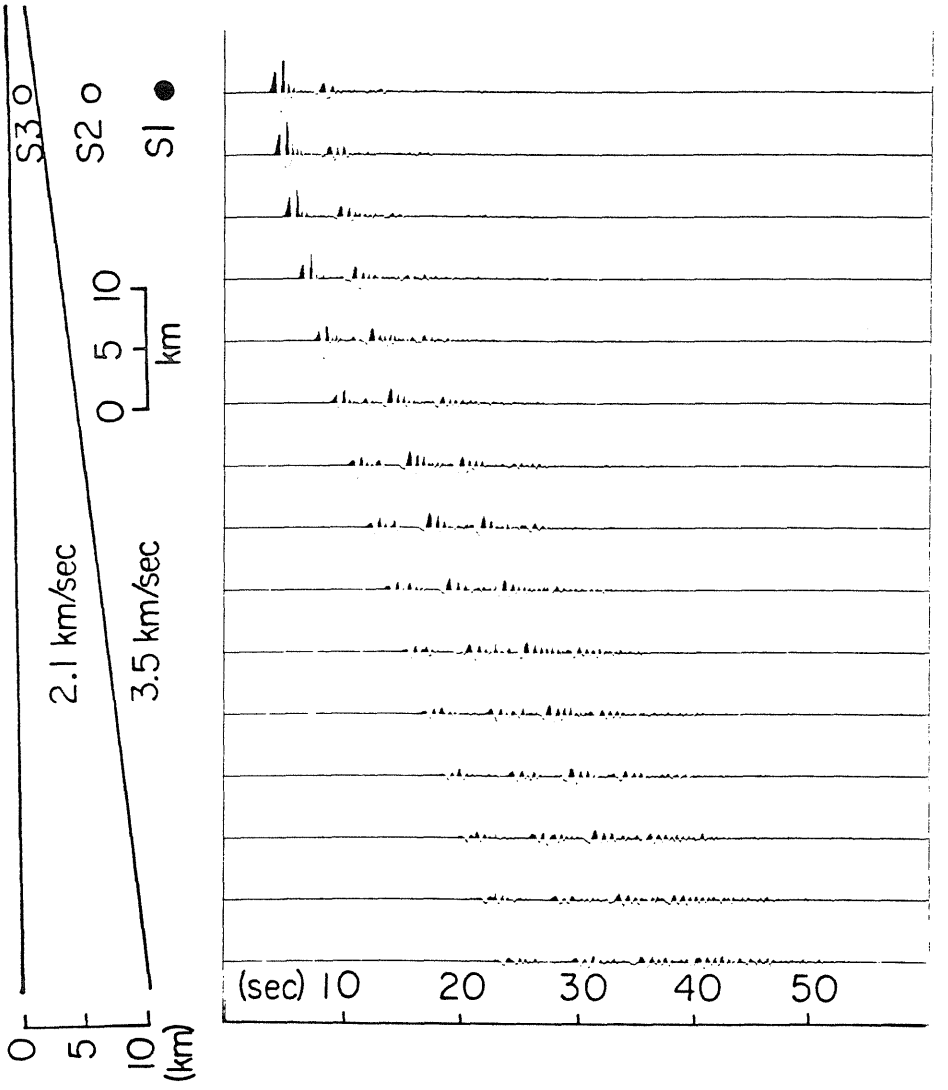

Figure II-3 Synthetic seismograms from source S1 (depth=13 km) for surface receivers.

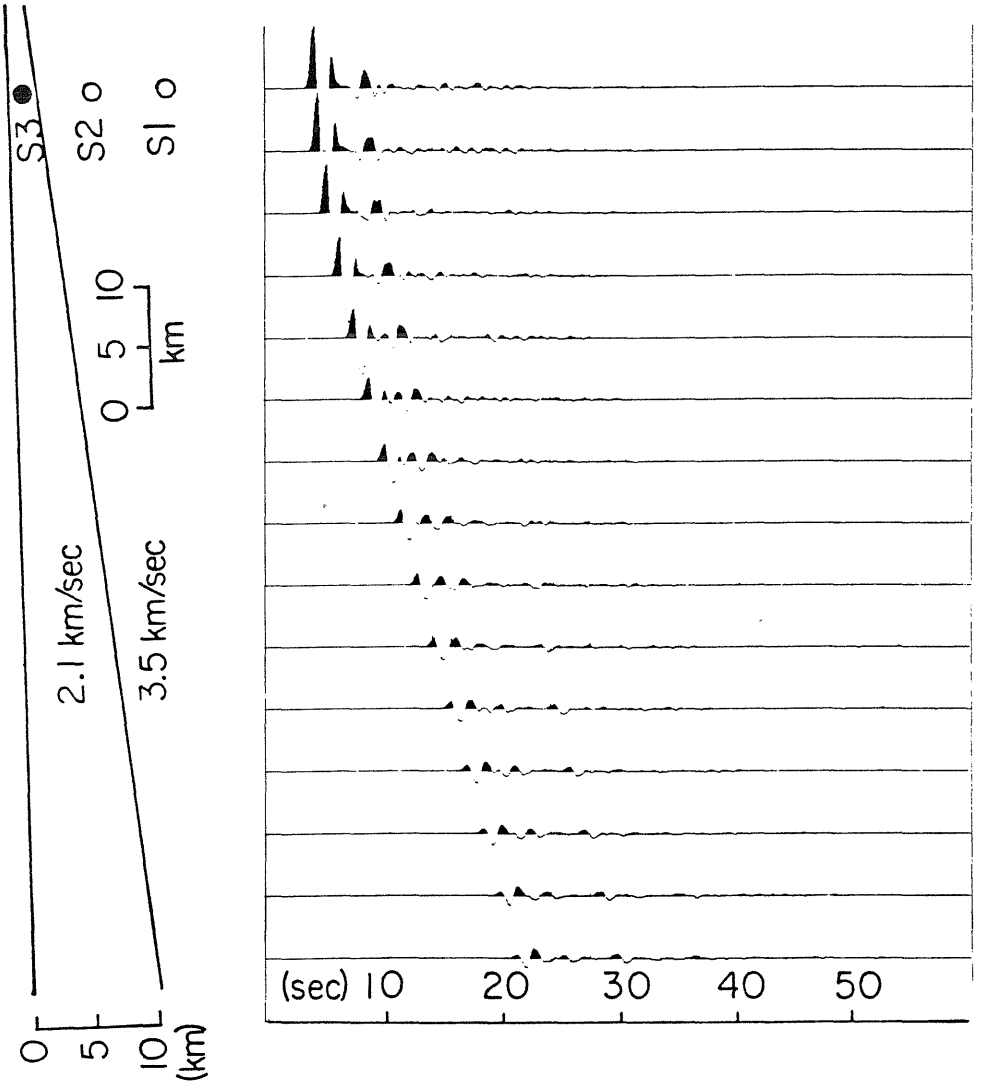

Figure II-4 Synthetic seismograms from source S3 (depth= 1 km) for the receivers at depth of 10 km.

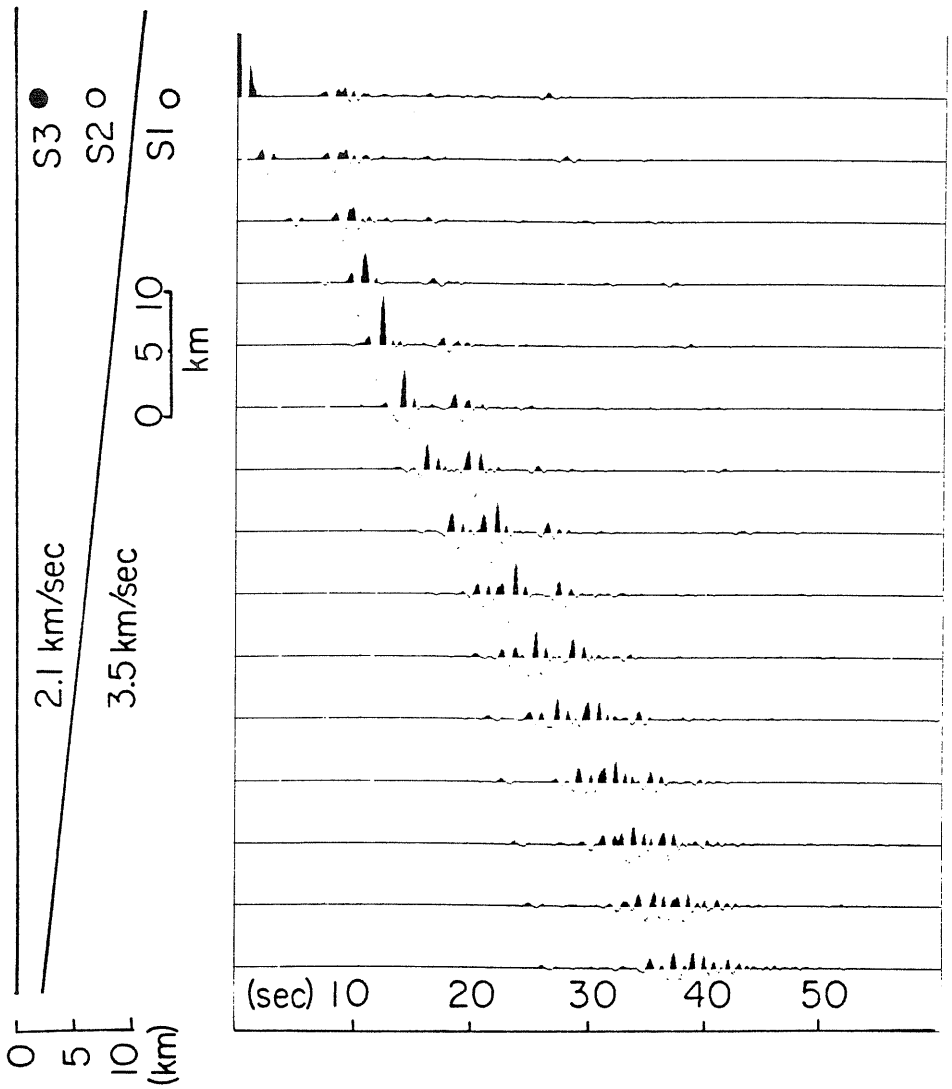

Figure II-5 Synthetic seismograms from source S3 (depth= 1 km) for surface receivers.

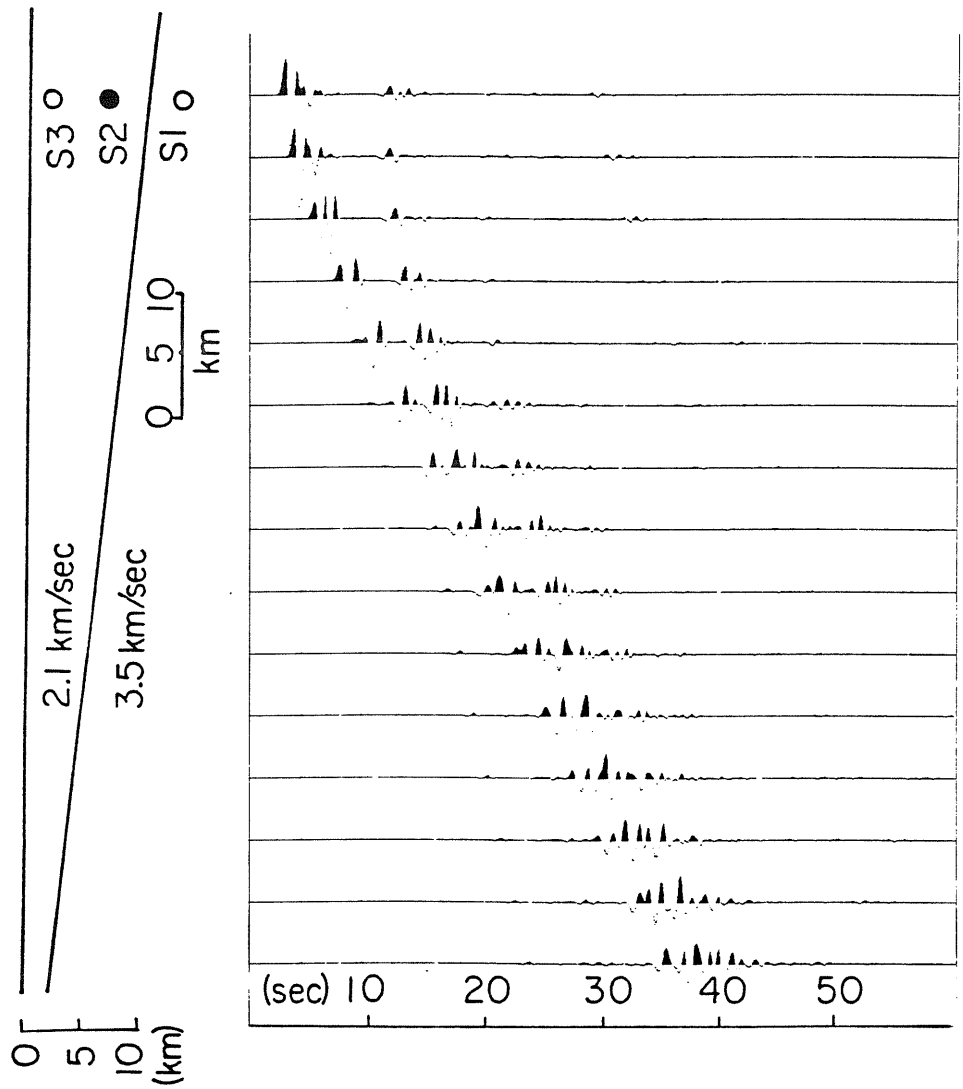

Figure II-6 Synthetic seismograms from source S2 (depth= 7 km) for surface receivers.

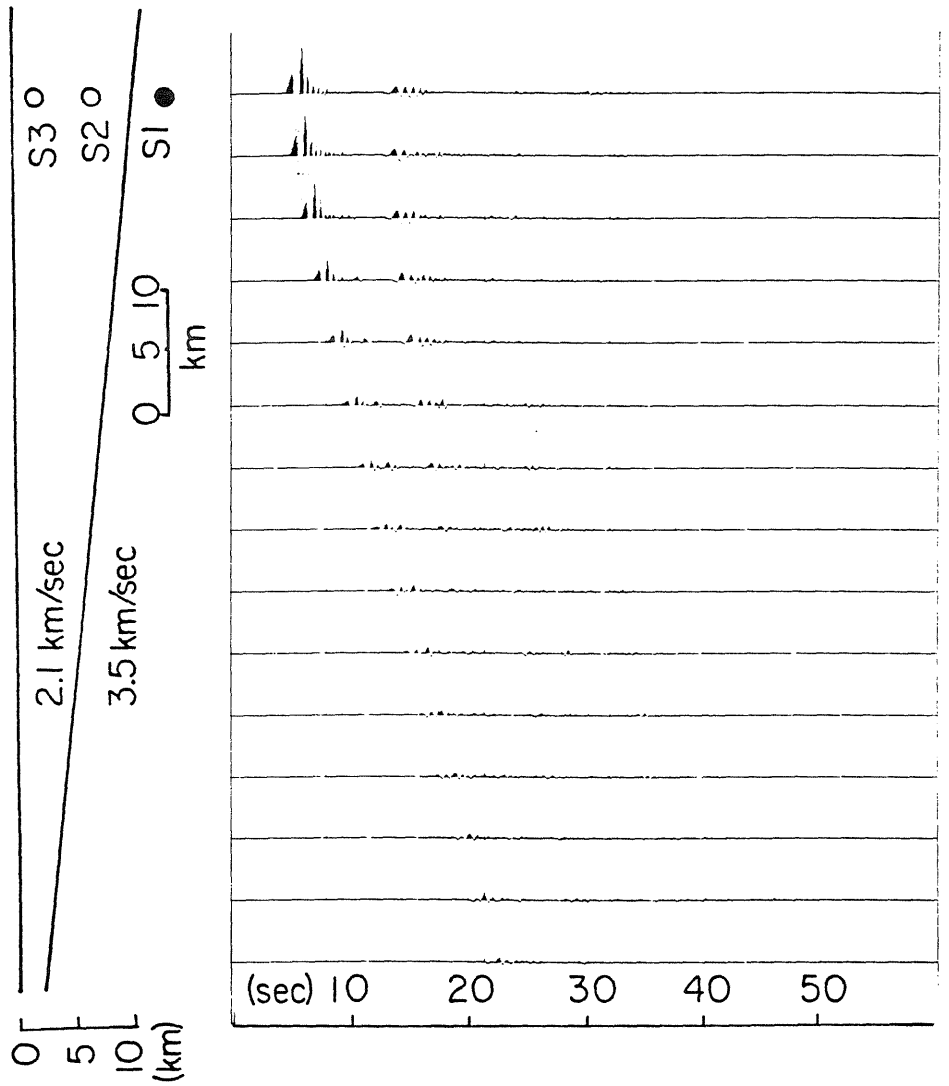

Figure II-7 Synthetic seismograms form source S1 (depth= 13 km) for surface receivers.

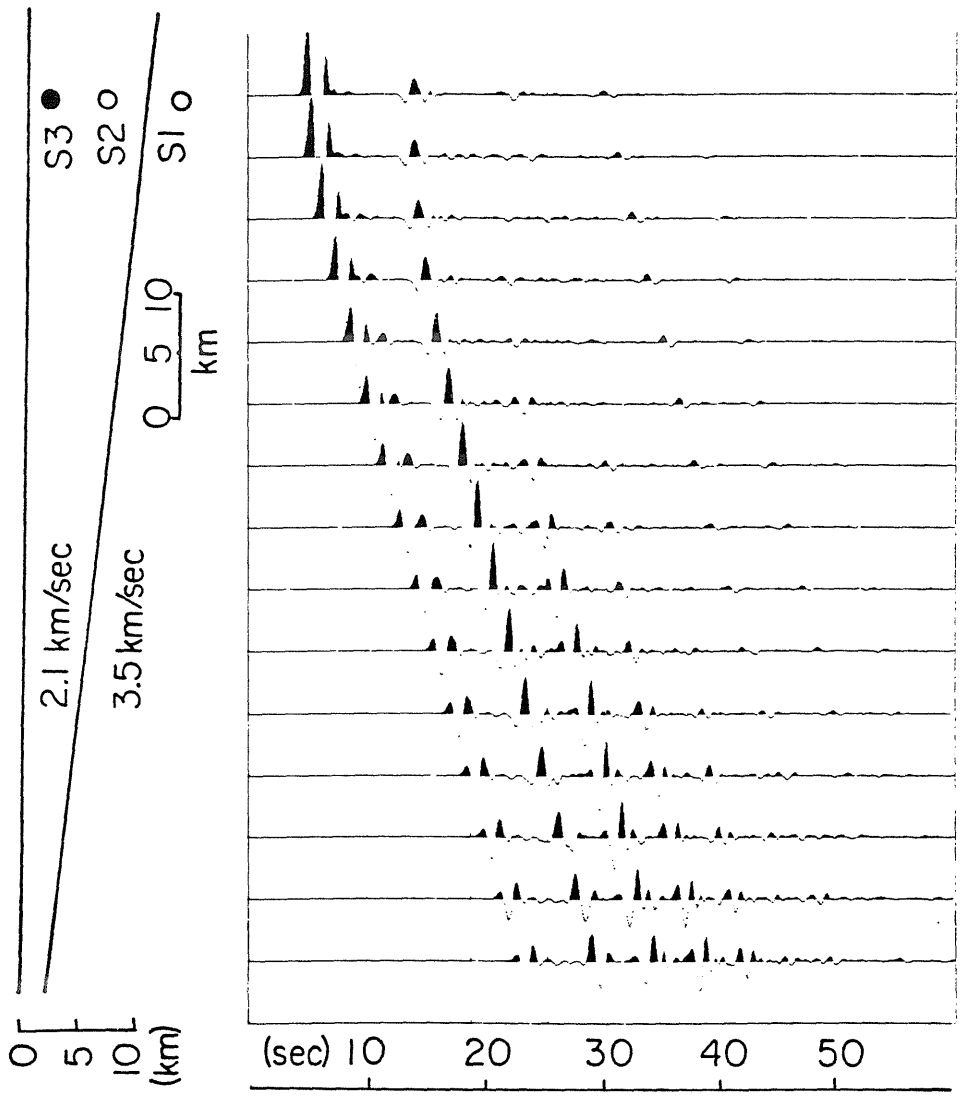

Figure II-8 Synthetic seismograms from source S3 (depth= 1 km) for the receivers at depth of 10 km.